Characterization of Mars Analog Soils with Microwave Radiation to Investigate Subsurface Water Extraction Utilizing Dielectric Heating

Osazonamen J. Igbinosun

A dissertation
submitted in partial fulfillment of the
requirements for the degree of

Doctor of Philosophy

University of Washington

2019

Reading Committee:

Adam Bruckner, Chair

Yasuo Kuga

Michelle Koutnik

Program Authorized to Offer Degree:
Aeronautics and Astronautics

University of Washington

Abstract

Characterization of Mars Analog Soils with Microwave
Radiation to Investigate Subsurface Water Extraction Utilizing Dielectric Heating

Osazonamen J. Igbinosun

Chair of the Supervisory Committee:
Adam Bruckner
Aeronautics and Astronautics

Dielectric heating of planetary simulant soils with microwave radiation has been demonstrated by others to be a potentially sustainable method of extracting subsurface water in planetary soils. Investigating subsurface water extraction stems from the need to acquire water resources to support human and robotic missions to Mars. However, dielectric heating is fundamentally a function of temperature and frequency-dependent dielectric loss mechanisms and the thermal properties of indigenous soils. These loss mechanisms lead to energy dissipation (i.e., heat) from the coupling of microwave radiation to soils. It is well established that dielectric losses in the microwave region are optimized in materials with high liquid water content at ambient conditions ($\sim$20°C). However, due to the low temperature and pressure of the near-surface of Mars (~ -63°C, 4.5 torr) stable liquid water does not exist; rather, subsurface ice is widespread across the planet. Considering these factors, an understanding of both the dielectric and thermal properties of simulant soils, which are strongly dependent on temperature and water content, will greatly benefit dielectric heating efforts on Mars. Therefore, this dissertation has analyzed dielectric loss mechanisms that contribute to the transfer of electromagnetic energy (2.6 – 18 GHz) to Mars simulant soils at environmental conditions comparable to those observed at the surface of Mars. In addition, dielectric heating of Mars simulants was performed using a low-power microwave transmis-

sion line system. Soil characterization studies demonstrated that dielectric loss mechanisms are significantly reduced at very low temperatures due to the absence of liquid water. However, unfrozen water films (indirectly observed in icy soils) produced higher losses than cold soils without ice. Moreover, heating icy, salty soils produced the highest heating rate among soil samples. Heating in lossy soils would be limited by the depth to which microwaves penetrate the subsurface (i.e., the penetration depth) combined with the thermal properties (e.g., thermal conductivity) of the soil. Given the insulative nature of soils observed on Mars; at low power, the subsurface could be heated just enough to liberate water vapor for extraction, without chemically altering the soil. Lastly, dielectric heating with microwave radiation could also have implications for the detection and sustainability of extant or extinct life in the subsurface of Mars.

TABLE OF CONTENTS

LIST OF FIGURES

LIST OF TABLES

ACKNOWLEDGMENTS

My deepest appreciation for his support and mentorship over the past 10 years goes to my doctoral advisor, Professor Emeritus Adam Bruckner. Over the years, his encouragement and guidance led to many invaluable research experiences that I will take with me for the rest of my career.

For their financial support, I wish to acknowledge the following: The National Science Foundation (NSF), the UW Astrobiology program (UWAB), the Graduate Opportunities and Minority Achievement Program (GO-MAP), and the William E. Boeing Department of Aeronautics and Astronautics (A&A).

Since my work was interdisciplinary I had a unique opportunity to interface with several departments across the University of Washington campus. From my qualifying exam committee to my doctoral supervisory committee, I would like to thank the following University of Washington faculty members from the A&A, Earth and Space Sciences, Electrical and Computer Engineering, Astronomy, and Chemical Engineering departments for their participation, feedback, and support throughout my doctoral studies: Prof. Carl Knowlen, Prof. Dana Andrews, Prof. Keith Holsapple, Prof. Bechet Acikmese, Prof. Stephen Wood, Prof. Michelle Koutnik, Prof. Yasuo Kuga, Prof. Victoria Meadows, and Prof. James Carothers.

I would also like to express my deepest gratitude to Shanti Garman for being an inspiring collaborator and a wonderful friend. In addition, I would like to thank Maya Gordon, Brett Biggs, Bailey Bonaci, and Oliver Ruo for their contributions and assistance in the Mars lab. Also, special thanks to Jake Quenzer, Marissa LaMadrid-Hermansfelt, Charlie Kelly, Curtis Promislow, and Sarah Li for their insight, support, and fellowship.

Furthermore, I must extend my appreciation to Dzung Tran, Eliot George, John Rogers,

Jaime Coyne, Tobin Weber, Kathy Troost, Martin Barmatz, and Oscar Vilches who were each so generous with their time, resources, and expertise.

I am grateful to my parents, Ekiuwa Obasuyi and Aimuamwosa Igbinosun, who taught me to be determined, passionate, and fearless. Those lessons have served me well throughout my life and will always be the root of my success. I am also blessed to have the encouragement and support of my older sister and eternal cheerleader, Osomwonken, who has always believed I could achieve extraordinary feats even when I had doubts.

Lastly, I wish to acknowledge members of the United States Navy who submitted letters of recommendation to the University of Washington over a decade ago that started the journey that has culminated in this dissertation. Thank you to Captain Wallace Moore, Captain Michael Herron, and Commander Stephen Jones for your inspiration, guidance, and belief in me.

Chapter 1

INTRODUCTION

Space exploration missions can be loosely divided into missions that are observational (orbiting a body remotely) and interactive (*in-situ*). Examples of observational missions include Hubble, James Webb, and Mars Odyssey. Interactive missions consist of rovers (Spirit/Opportunity and Curiosity), landers (Viking and Phoenix), and human missions (Apollo Lunar Landers). In general, interactive missions give rise to a variety of engineering challenges, particularly for human missions. ISRU (*in-situ* resource utilization) strategies endeavor to overcome some of these challenges and increase mission capabilities by acquiring and utilizing indigenous resources on planetary bodies. Upcoming phases of interactive space exploration include sample return and (continued) human missions. Both would benefit from ISRU, whose strategies seek to develop methods to supply either propellant or consumable resources, such as oxygen and water, extracted from the atmosphere or subsurface of the planetary body being explored. Water, in particular, is a desirable resource for both robotic (propellant for sample return) and human missions (consumables).

Human space exploration, which will extend to the planet Mars in the near future, would greatly benefit from ISRU strategies. With global average temperatures around $-63°$C and only trace amounts of oxygen in its tenuous atmosphere, Mars is considered an extreme environment [1]. Also, Mars does not have stable bodies of liquid water at its surface; rather, it has other water reservoirs, e.g., surface ices (H_2O and CO_2) in the polar regions, water vapor in the atmosphere, and the recent discovery of evidence to support a subglacial lake beneath the southern polar cap [2]. Another water reservoir of Mars is near-surface ice in the mid-latitude and equatorial regions [3–5]. This ice is expected to exist within a meter of the surface. Furthermore, the subsurface of Mars contains adsorbed water vapor, which

is considered to be in constant exchange with the near-surface atmosphere on a diurnal basis [6]. Conventional (Earth-based) means of acquiring water resources, such as direct access to bodies of liquid water, drilling to subsurface aquifers, and precipitation harvesting, are either unavailable or introduce significant complexity (e.g., drilling in extremely cold environments). Thus, other means of extracting water resources on Mars must be sought.

A potential solution is the extraction of water resources with microwave radiation, which could be combined with atmospheric water vapor extraction [7]. Dielectric loss mechanisms are fundamental processes that occur when matter is subjected to microwave radiation and is the basis for conventional microwave heating in microwave ovens. Subsurface heating of soils could serve as a primary extraction method; whereby, sublimation of subsurface ice, driven by energy transfer generated from dielectric heating with microwave radiation, migrates to a cold trap at the surface. This approach would eliminate the need for energy intensive drilling and excavation methods. Demonstrations of energy coupling to icy soils have been successfully performed and indicate that dielectric heating is a potentially viable extraction technique [8–10]. However, little has been documented about how dielectric loss mechanisms perform at low temperatures—particularly temperatures expected at the surface of Mars. Furthermore, soil components, i.e., adsorbed water, ice, salts, etc., trigger different loss mechanisms. These frequency and temperature-dependent mechanisms characterize the interaction between microwave radiation and soil components and must be understood in order to pursue dielectric heating techniques. Thus, the work described in this dissertation has investigated how understanding inherent dielectric loss mechanisms within Mars simulant soils is critical to the concept of employing dielectric heating in extreme environments. Additionally, dielectric heating as a post-extraction, thermal processing technique has also been proposed [11].

Subsurface water extraction via dielectric heating, although a potential benefit to human and robotic exploration of Mars, may have an impact on indigenous life that may exist in the subsurface of Mars. Due to the mystery surrounding the existence of extant or extinct life on Mars, specifically in the subsurface, consideration should be given to the

effects of microwave radiation on potential biological material within the soil matrix. Thus, investigations of dielectric heating are relevant to Astrobiology (i.e., the study of life in the universe) because it addresses two of the major topics listed in the Astrobiology Strategy– *Identifying, exploring and characterizing environments for habitability and biosignatures* and *Constructing habitable worlds* [12]. Moreover, identifying techniques for extracting water resources can aid manned and robotic missions seeking to investigate these topics. Lastly, in general, ISRU strategies are very much grounded in the concept of developing technologies to support the 'future of life' (formerly listed as Goal 6 of the NASA Astrobiology Roadmap [13]) which highlights advancements to support human space exploration.

1.1 Subsurface Environment of Mars

Orbital observations of the near-surface of Mars with a variety of spectroscopic instruments (neutron, near-infrared) have identified water in the near-surface of Mars, including detection of $\sim$2.0 – 10 wt.% (weight percent) of water-equivalent hydrogen [14, 15]. Water-equivalent hydrogen signatures at the near-surface of Mars (Fig. 1.1) are presumed to be due to adsorbed water or hydrated minerals [3, 16, 17], however the precise nature of the signature in this figure is not well understood [17]. Fine-grained soil observed by the Curiosity Rover's ChemCam and APXS instruments identified hydration abundances consistent with measurements by Viking 1 and 2 [17]. These findings demonstrate that water resources outside of the polar regions can be found in the near-surface. Dielectric heating of these soils will be dependent on the phase and/or configuration of water molecules bound to soil surfaces.

Without as robust of a hydrosphere as Earth's and limited by low temperature and pressure, global annual distribution of water on Mars presents as seasonal variations of water vapor suspended in the atmosphere. These variations can be as high as 100 precipitable micrometers (pr.μm) in the summer season but drop to less than 5 pr.μm during winter [18]. This atmospheric water vapor has been observed to adsorb to soil grains in the near-surface [6]. Moreover, in terms of atmospheric water adsorption, allophane-rich Mars analog soils (i.e., JSC Mars-1) exhibit enhanced adsorption due to nanophase iron oxides (e.g., ferrihy-

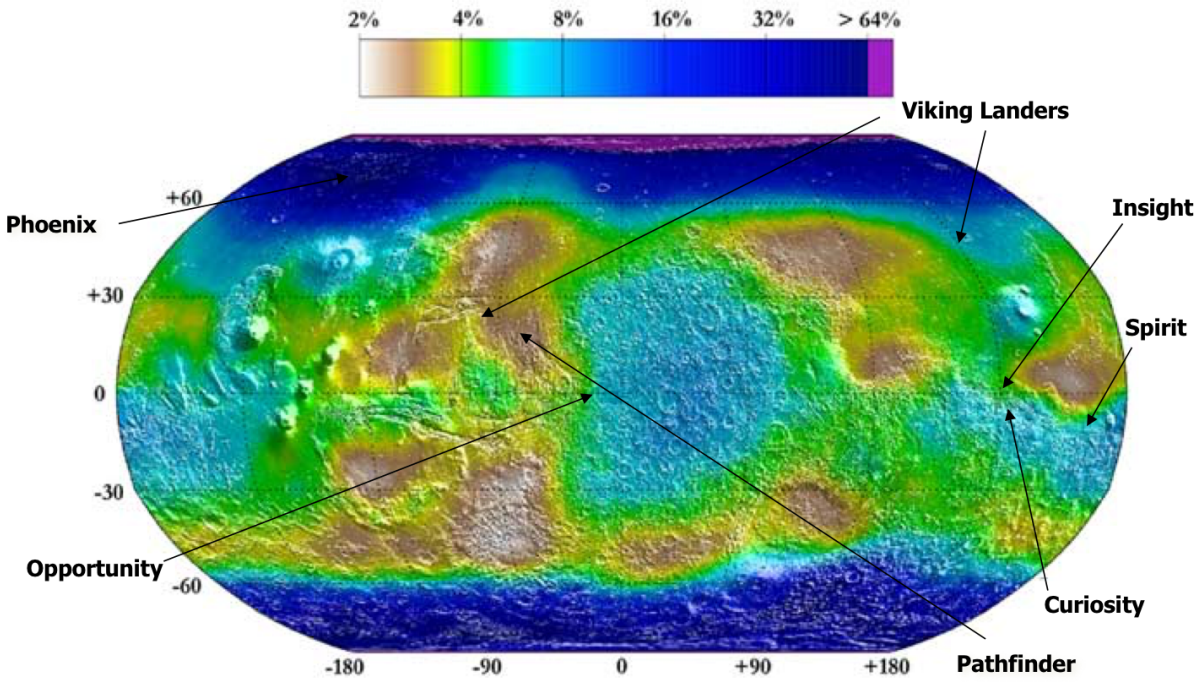

Figure 1.1: Water equivalent hydrogen abundances (by mass) as observed by the Neutron Spectrometer instrument aboard the Mars Odyssey spacecraft [3]. Landing sites for various Mars surface missions included for reference.

drite, magnetite) [19]. However, this analog soil does not appear to be representative of soils present in Gale Crater (located near the equator) and may not be as widespread across the surface of Mars as expected, which could present overestimates of water adsorption if used in regolith-atmosphere interaction models [17]. To reconcile these characteristics of the atmosphere and subsurface water, an approach to characterizing the interaction between microwave radiation and soils is to simulate the Mars environment, specifically the environmental conditions of the subsurface and its components with a variety of simulants (including JSC Mars-1) . The work in this dissertation accomplishes these simulations by conducting studies of Mars analog soils in a Mars environmental simulation facility [7].

1.2 Dielectric Heating of Soils

Researchers at the Marshall Space Flight Center (NASA) have conducted several proof-of-concept studies to determine the feasibility of using microwaves for subsurface extraction of water. They were able to successfully demonstrate the extraction and capture of water vapor (∼95 wt.%) from cryogenically cooled lunar simulant soil under vacuum conditions using microwave radiation at 2.45 GHz at 1.0 kW [8]. They surmised that the nature of the dielectric properties (i.e., complex permittivity) of planetary soils is critical for understanding this type of application. Additionally, these researchers measured the complex permittivity and permeability of several lunar analog soils at two microwave frequency bands (2.45 – 3.95 and 8.2 – 12.4 GHz) [8, 9]. Lastly, Ethridge and Kaukler, 2012 sought to model the diffusion of heat generated by microwaves. These experiments were mostly preliminary; although further investigation was proposed, work from this group (and microwave water extraction research, in general) effectively ceased after 2012.

The application of dielectric heating for subsurface water extraction by Ethridge and Kaukler, 2009 is compelling and provides a potentially effective solution to the problem of utilizing indigenous water resources on planetary bodies. However, complex permittivity measurements of planetary soils (mostly lunar simulants) provided by Ethridge and Kaukler, 2012 were assumed to be constant in heating models and did not account for variations in permittivity due to soil components. Furthermore, dielectric properties of soil components are the result of the excitation of dielectric loss mechanisms at a particular frequency and temperature and contribute to heating effects. Yet, neither details of loss mechanisms, including the dependence on frequency and temperature, nor their role in dielectric heating were discussed. Although Ethridge and Kaukler, 2009 successfully diagnosed the efficacy of water extraction as a function of applied power, the nature of dielectric losses in soils is highly nuanced and requires an understanding of the interaction between microwave radiation and soil components. Lastly, the analysis of complex permittivity requires a comprehensive assessment of measurement methods; however, these were not discussed in detail by either

Ethridge and Kaukler, 2009 or Ethridge and Kaukler, 2011.

On average, the surface temperature of Mars is ∼100°C lower than average surface temperatures on Earth. Thus, temperature-dependent microwave coupling to soils will greatly impact dielectric heating efforts. To understand this fundamental phenomenon of dielectric loss mechanisms and their role in dielectric heating, the nature of this coupling is investigated throughout this dissertation using a variety of Mars simulant soils. The frequency range of 2.6 – 18 GHz was chosen based on available microwave transmission line equipment. To address the viability of performing transmission line measurements of particulate media at low temperature, a feasibility study was performed. This study was followed by a characterization study of simulant soils to analyze environmental factors (e.g., pressure, temperature, composition, grain size, etc.) and their impact on loss mechanisms.

1.3 Organization

This dissertation presents a series of experiments and analysis to determine the feasibility and practicality of dielectrically heating Mars analog soils with microwave radiation. The dissertation is divided into eight chapters and one appendix. Chapter 2 provides an overview of dielectric loss mechanisms, microwave measurement theory, and measurement techniques used to quantify dielectric losses. Chapter 3 provides details of all the experimental components and facilities. Chapter 4 introduces the feasibility study that was used as the basis for all soil measurements. Chapter 5 presents an introduction to the soil characterization study that surveys all simulants at several environmental conditions. Results and discussion of this study are also presented in this chapter. Chapter 6 details dielectric heating experiments performed on select soil simulants followed by analysis and discussion of results. Chapter 7 discusses the impact of microwave radiation on subsurface microbial environments, including interactions with extremophiles. Lastly, Chapter 8 concludes the dissertation. The appendix provides supplementary technical design data and analysis.

Chapter 2

MICROWAVE MEASUREMENT THEORY AND METHODS

A central phenomenon used in this research is the concept of dielectric heating. Dielectric heating refers to a process whereby an electrically insulating material, or dielectric, is irradiated with microwave radiation and heating arises from losses, i.e., energy dissipation, in the material. The microwave region of the electromagnetic spectrum is generally defined as ranging from 300 MHz – 300 GHz and lies between infrared and radio frequencies. The most common use of dielectric heating is found in microwave ovens, which are used to penetrate the subsurface of foods for heating as opposed to conventional methods that rely on surface heating (e.g., standard ovens, counter-top stoves). Microwave ovens utilize microwave radiation at 2.45 GHz to convert electromagnetic energy to thermal energy via interactions with water molecules. This is the underlying concept of microwave ovens, which are optimized to heat materials containing water. Similarly, the concept of dielectric heating can be applied to soils to determine the efficacy of subsurface heating. However, in icy soils, microwave radiation would not couple efficiently with water ice because ice couples poorly to radiation at microwave frequencies; rather, maximum coupling occurs at very low radio frequencies (1.0 – 10 kHz) [20]. Presumably, at freezing conditions, heating would rely on dielectric losses occurring within soil particles to transfer heat to ice within the soil matrix. However, water adsorbed (or bound) to the surface of soil grains could also contribute to dielectric losses. Thus, this chapter presents an overview of dielectric loss mechanisms and measurement techniques used during experimental studies.

2.1 Dielectric Loss Mechanisms

The electric response of a material to an alternating electromagnetic field, as a function of angular frequency, is given by the complex permittivity, $\varepsilon(\omega)$,

$$\varepsilon = \varepsilon'(\omega) - \varepsilon''(\omega)j \tag{2.1}$$

where the real part, ε', is a measure of energy storage in a material, $j = \sqrt{-1}$, and the imaginary part, ε'', is a measure of energy dissipation (e.g., heat). Equation 2.1 can also be presented as

$$\varepsilon_r = \varepsilon'_r(\omega) - \varepsilon''_r(\omega)j; \varepsilon_r = \frac{\varepsilon(\omega)}{\varepsilon_0} \tag{2.2}$$

where ε_0 is the vacuum permittivity and ε_r is the relative permittivity. Throughout this dissertation, $\varepsilon(\omega)$ refers to the relative complex permittivity; similarly, $\varepsilon'_r(\omega)$ and $\varepsilon''_r(\omega)$ refer to the dielectric constant and dielectric loss (or loss factor), respectively (also denoted as ε' and ε''). Additionally, throughout this dissertation, the term "permittivity" refers to relative permittivity. The relative permittivity is unit-less. It should be noted that the complex permeability, i.e., the magnetic response of a material to an alternating electromagnetic field, can analogously be defined with a real and imaginary part, where the imaginary part is a measure of dissipative losses. Although dissipative losses due to an applied magnetic field can induce significant heating in magnetic materials [21], particularly magnetic materials observed in the soils of Mars [22], none of the materials analyzed in this dissertation had appreciable magnetic content.

The complex permittivity is frequency-dependent and can vary based on several dielectric loss mechanisms (Table 2.1). These mechanisms result in charge displacements that vary as an applied electric field alternates with time. For example, during dipolar polarization at 1.0 GHz, dipoles will attempt to align with the electric field as it alternates 10^9 times per second, resulting in heat generated by frictional forces resisting the motion of the dipoles [21]. Loss mechanisms can occur in discrete frequency bands (as shown in Figure 2.1) or be more prevalent in certain media, such as water or hydrated materials. Moreover, the complex

Table 2.1: Microwave Region Dielectric Loss Mechanisms [21]

Dipolar (orientation polarization)	Re-orientation of dipoles due to changing E-field
Current conductivity	Re-distribution of charge particles under the influence of E-field
Maxwell-Wagner	Interfacial charge accumulation (heterogeneous media)
Electronic	Displacement of electrons around nuclei
Atomic	Displacement of nuclei due to unequal charge distribution

permittivity is very sensitive to water, whether the phase is liquid (e.g., pure or saline), ice, adsorbed, or present in hydrated minerals [23]. Figure 2.1 shows the imaginary part (loss factor) as a function of frequency for a heterogeneous moist material. The grey-shaded area includes all loss mechanisms present in the microwave region; whereas, the red-shaded area limits loss mechanisms to the microwave range analyzed in this dissertation. Loss mechanisms dominating the microwave range (10^8 – 10^{11} Hz) and contributing to heating effects are due to free and bound water (W1, B). "Free" refers to liquid water and "bound" refers to chemically or physically bound water molecules (i.e., adsorbed water) [23]. It should be noted that although each mechanism has a unique bandwidth, the magnitude of frequency-dependent losses attributed to each mechanism will, in general, vary for different materials. Moreover, the electrical properties of bound water are not the same for different heterogeneous systems and are composition-dependent [24]. Loss mechanisms due to atomic and electronic polarization occur in the infrared and visible regions of the electromagnetic spectrum (10^{12} – 10^{15} Hz) and do not contribute significantly to losses in the microwave region. The combined response to these mechanisms is given by the effective loss factor, ε_{eff} [21],

$$\varepsilon''_{eff}(\omega) = \varepsilon''_d(\omega) + \varepsilon''_e(\omega) + \varepsilon''_a(\omega) + \varepsilon''_{MW}(\omega) + \frac{\sigma}{\omega\varepsilon_0} \tag{2.3}$$

where the dipolar, electronic, atomic, and Maxwell-Wagner loss mechanisms are represented by the subscripts d, e, α, and MW, respectively. The last term in Equation 2.3 represents

conductivity effects, where σ is the electrical conductivity. Depending on the frequency range, the effective loss factor could be comprised of only the dominant loss factors. For example, in the microwave region analyzed by this dissertation, the dominant mechanisms are dipolar relaxations related to water (represented by W1 and B) with lesser contributions from conductivity (C) and ice relaxation (I) (Fig. 2.1). Throughout this dissertation the effective loss factor is simply denoted as ε''.

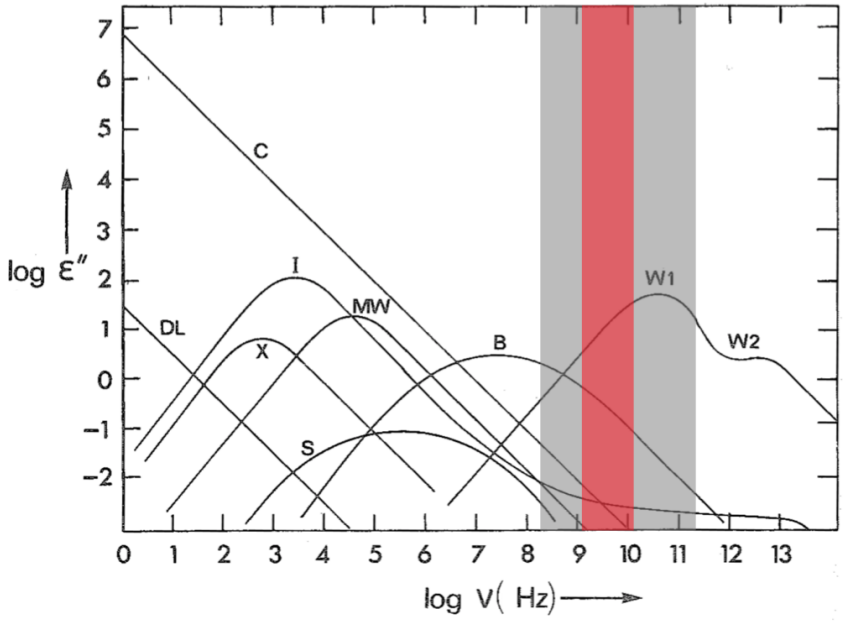

Figure 2.1: Dielectric Loss Mechanisms in a moist heterogeneous material. The grey-shaded region is the microwave region of the electromagnetic spectrum. The region in red represents the microwave frequencies studied in this dissertation. Dielectric loss mechanisms are labeled as follows: C (conductivity), DL (charged double layers), X (crystal water relaxation), I (ice relaxation), MW (Maxwell-Wagner effect), S (surface conductivity), B (bound water relaxation), W1 (principal relaxation of free water), W2 (second relaxation of free water) (modified from Hasted, 1973).

On the surface of Mars, there is expected to be a dry overburden above an icy soil layer in the mid-latitudes and equatorial regions [5, 6]. Therefore, in the absence of liquid water, losses due to bound water should dominate in soils irradiated with microwave radiation

(with significantly lower contributions from conductivity and ice relaxation). Moreover, the magnitude of the loss factor is dependent on the dominant loss mechanisms. It should be noted that loss mechanisms for ice and hydrated minerals (i.e., ice and crystal water relaxations, respectively) are highest at much lower frequencies ($\sim 10^2 - 10^5$ Hz).

2.2 Measurement Methods

Microwave transmission lines can take many forms; of these, coaxial and waveguide transmission lines are the most common for measuring electrical properties of solid, liquid or porous media. Coaxial transmission lines (coax) can be designed to measure reflection and transmission parameters (airlines) or reflection-only (dielectric probe). A coaxial transmission line consists of a metal inner conductor and a coaxial outer conductor, with a dielectric material between them to support the outer conductor (Fig. 2.2). Waveguide transmission lines (or waveguides) are hollow, rigid metal structures (aluminum or brass) and do not require a dielectric for structural support (Fig. 2.3). Waveguides can be designed with either rectangular or circular cross-sections.

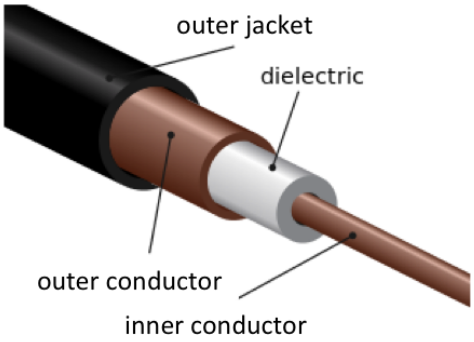

Figure 2.2: Coaxial transmission line

Figure 2.3: Waveguide transmission line

Transmission lines are selected for use based on several factors, e.g., frequency range, bandwidth, and attenuation. Waveguides exhibit low losses but have limited bandwidth (determined by the cutoff frequencies) and are prone to dispersion. The cutoff frequency

depends on the cross-sectional dimensions of the waveguide aperture and is the lowest frequency that will propagate within the waveguide for a given mode [Section 2.2.1]. Since each waveguide has a small frequency range, several waveguides were required to cover the 2.6 – 18 GHz range used for dielectric loss measurements. In contrast, coaxial transmission lines have a much broader frequency range and are non-dispersive but exhibit higher attenuation (0.7 dB/ft at 20 GHz [25]). Attenuation for both coaxial and waveguide transmission lines increase with increasing frequency, but the maximum attenuation for the highest frequency waveguide analyzed in this dissertation (P-band) is known to be nearly an order of magnitude lower than coaxial lines [25]. Indeed, both types of transmission lines offer advantages and disadvantages and were studied to determine which was better suited for the applications of this research. Measurements with transmission lines require an understanding of the transmission propagation modes and calibration requirements.

2.2.1 Propagation Modes

Microwaves can propagate in several modes within a transmission line. These modes are the transverse electromagnetic (TEM), transverse electric (TE), and transverse magnetic (TM) and are unique to the type and geometry of the transmission line. Coaxial lines, having two conductors, can support TEM, TE, and TM wave propagation; whereas, rectangular waveguides (single conductor) are limited to TE and TM only [25–27]. These modes can be expressed as solutions to Maxwell's equations [26], where E, H, and μ are the electric field, magnetic field, and magnetic permeability respectively,

$$\nabla \times E = -j\omega\mu H \tag{2.4}$$

$$\nabla \times H = j\omega\mu E \tag{2.5}$$

with boundary conditions that constrain the longitudinal components of the electric and magnetic fields, i.e., E_z and H_z, respectively as follows:

$$\begin{aligned} TE &: E_z = 0, H_z \neq 0 \\ TM &: E_z \neq 0, H_z = 0 \\ TEM &: E_z = 0, H_z = 0 \end{aligned} \tag{2.6}$$

Solutions to these equations for TE/TM modes yield m variations in the x-direction and n variations in the y-direction resulting in the following notation: TE_{mn} and TM_{mn}. The frequency range for each waveguide is determined by the cutoff frequency,

$$f_{c_{mn}} = \frac{1}{2\pi\sqrt{\varepsilon\mu}}\sqrt{\left(\frac{m\pi}{a}\right)^2 + \left(\frac{n\pi}{b}\right)^2}, \tag{2.7}$$

for neighboring modes where a and b are the waveguide aperture dimensions and $a > b$ (Fig. 2.4). This equation applies to both TE and TM modes. Waves cannot propagate within the aperture dimensions of the waveguide at frequencies lower than the cutoff frequency.

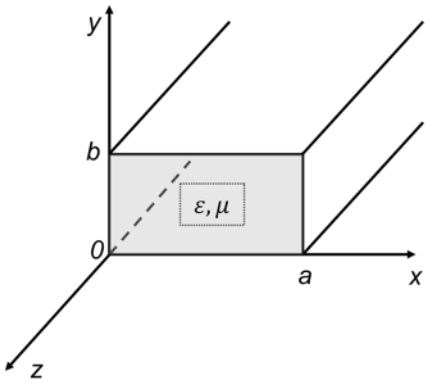

Figure 2.4: Rectangular waveguide geometry

The dominant mode (i.e., lowest cutoff-frequency mode) for rectangular waveguides is the TE_{10} (for $a > b$). The cutoff frequency of the TE_{10} mode determines the lower limit of

the frequency range for a waveguide with aperture dimensions a and b. The upper limit of the frequency range is determined by the cutoff frequency of the next mode (TE_{20}, for $a > b$) and serves to restrict higher order modes from propagating within the waveguide. This range is further constrained (by ∼30%) to minimize dispersion caused by differing group velocities that vary as a function of frequency [27]. Extending the frequency range to include higher order modes distorts the electromagnetic field configurations within transmission lines, introduces signal loss, and is usually avoided. Frequency ranges for the waveguides used in this dissertation are listed in Table 2.2. Waveguides are labeled with Electronic Industries Alliance (EIA) designations.

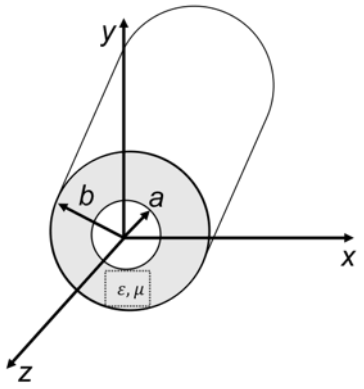

Figure 2.5: Coaxial line geometry

The frequency range for coaxial lines is similarly defined, but the dominant mode is TEM (where f_c=0). The next highest mode in a coax is TE_{11} and the cutoff frequency is determined by the dimensions of the coax (Fig. 2.5). An approximate solution for the cutoff frequency for the TE_{11} mode in a coaxial line is given by:

$$f_{c_{11}} = \frac{1}{\pi(a+b)\sqrt{\varepsilon\mu}} \tag{2.8}$$

where a and b are the radial dimensions of the coax cross-section as shown in Figure 2.5 [27, 28]. Thus, $f_{c_{11}}$ sets the upper limit of the operating frequency range. For the coaxial lines used in this research $f_{c_{11}}$∼18 – 34 GHz.

Table 2.2: Waveguide details

EIA Designation	Letter Designator	$TE_{1,0}$ Frequency range (GHz)	Cutoff frequency (GHz)	Cross-section dimensions (cm)	Calibration kit
WR284	S	2.6-3.95	2.078	7.22 x 3.41	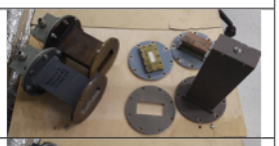
WR187	G	3.95-5.85	3.152	4.75 x 2.22	
WR137	C	5.85-8.2	4.3	3.49 x 1.58	
WR110	H	7-10	5.24	2.86 x 1.27	
WR90	X	8.2-12.4	6.55	2.28 x 1.01	
WR62	P	12.4-18	9.486	1.58 x 0.79	

Lastly, it should be noted that the waveguides used in this research were excited by coaxial transmission lines. In other words, coax-to-waveguide adaptors (N-type) were used to transmit microwave signals from the network analyzer to the waveguides. In order to excite the desired TE_{10} propagation mode in the waveguide, the adaptor consists of a center conductor extended as a probe into the waveguide (Fig. 2.6). The backplate of the adaptor acts as a short to aid in matching the impedance of the coaxial line to that of the waveguide. The fields propagating from the probe excite TE_{10} and higher order modes [27–29]. Due to the single conductor design of the waveguide and its aperture dimensions, TEM and higher order TE modes are cutoff and do not propagate.

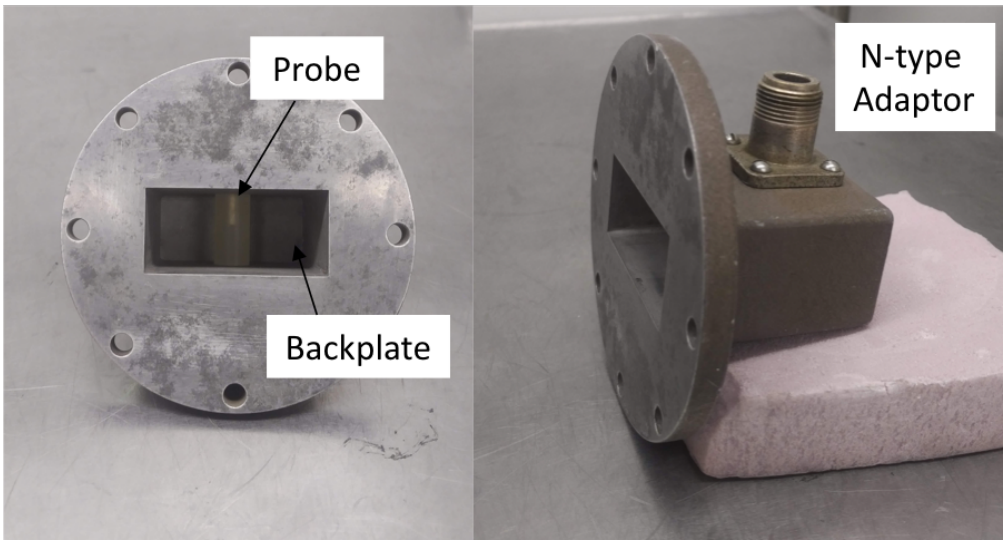

Figure 2.6: Coax-to-waveguide adaptor

2.2.2 Calibration Requirements

Measurement calibration is a procedure that removes the systematic errors (repeatable measurement variations) that cause uncertainty in measurements. During calibration, the vector network analyzer measures well-defined standards and mathematically compares the results against ideal versions of these standards (calibration algorithms). The techniques described here assume the material under test (MUT) is homogeneous. Measurements taken during calibration characterize a measurement reference plane and are made with all components in place, including cables and connections, except the MUT. Calibrations remove any erroneous signals caused by connections and errant reflections. This results in the transmitted and reflected signals being solely due to the properties of the MUT. Although there are several calibration types (with accompanying calibration algorithms) to choose from when using transmission lines, coax measurements were processed with a one-port calibration (SOL algorithm) and waveguides were processed with a two-port calibration (SSLT algorithm) [30].

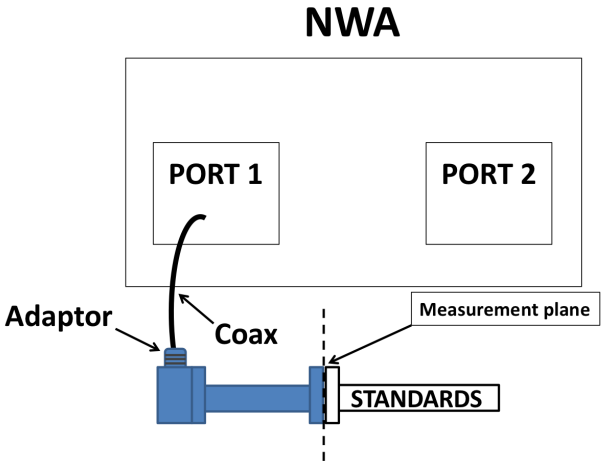

Figure 2.7: Configuration for a one-port calibration with a vector network analyzer (NWA) at Port 1. Measurements with standards are repeated at Port 2 for a two-port calibration.

A one-port calibration is used for reflection-only measurements (coaxial line). For example, in Figure 2.7, the system is calibrated at port 1 for reflection-only measurements (which could also be performed at port 2). The calibration algorithm, SOL, refers to the calibration standards, Short-Open-Load [30]. The short/open standards are used to define reflection behavior of the signal; whereas, the load standard sets directivity parameters. Directivity refers to the direction of the signal. Each standard is measured at the port where measurements will take place (e.g., port 1 as shown in Figure 2.7). Once all standards have been measured and the calibration is processed, calibration standards are no longer needed and the material can be measured.

For waveguides a two-port calibration (reflection and transmission measurements) and a Short-Short-Load-Thru (SSLT) algorithm was used. Similar to the one-port calibration, the two shorts ($\frac{1}{4}\lambda$ offset) define reflection behavior and the load standard sets directivity parameters. In addition, a thru standard is included to characterize transmission behavior. For calibration, each standard is attached to the waveguide and measured at *both* port 1 and port 2; i.e., once standards are measured at port 1, the process is repeated at port 2 (Fig. 2.7). After the short/load standards are measured, the waveguides are attached and a thru

standard is measured (Fig. 2.8). Once all standards have been measured, the calibration is processed. Similar to one-port calibrations, calibration standards are no longer needed after this process has completed. Due to the limited bandwidth of waveguides, six calibration kits were required for the 2.6 – 18 GHz frequency range (Table 2.2).

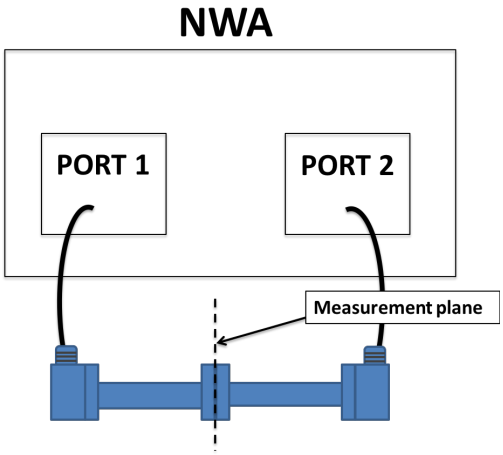

Figure 2.8: Configuration of the thru standard for a two-port calibration.

2.3 Data Acquisition

The microwave frequencies used for the research presented in this dissertation were generated by network analyzers. In general, the frequency range of a network analyzer is limited by its internal components. Network analyzers are instruments designed to test and measure electrical networks by acquiring scattering parameters. Scattering parameters (or S-parameters) are ratios of the output to input of a signal and can be defined for a network with an arbitrary number of ports. However, the work described in this dissertation is limited to one-port and two-port networks only. Input nodes are labeled a and output nodes are labeled b (Fig. 2.9). The subscript notation for S-parameters refers to the output port (first subscript) and input port (second subscript). The input/output ports discussed here are identical to port 1 and port 2 from the previous section. Each S-parameter assumes that there is only one input

source. S-Parameters are complex-valued and include amplitude and phase characteristics in the frequency domain and are a superposition of all reflected and transmitted components of the MUT. The four cases for a two-port network are displayed in Figure 2.9 and are as follows:

- $S_{11} = \frac{b_1}{a_1}$, assumes $a_2 = 0$: Reflection coefficient (forward)
- $S_{21} = \frac{b_2}{a_1}$, assumes $a_2 = 0$: Transmission coefficient (forward)
- $S_{12} = \frac{b_1}{a_2}$, assumes $a_1 = 0$: Transmission coefficient (reverse)
- $S_{22} = \frac{b_2}{a_2}$, assumes $a_1 = 0$: Reflection coefficient (reverse)

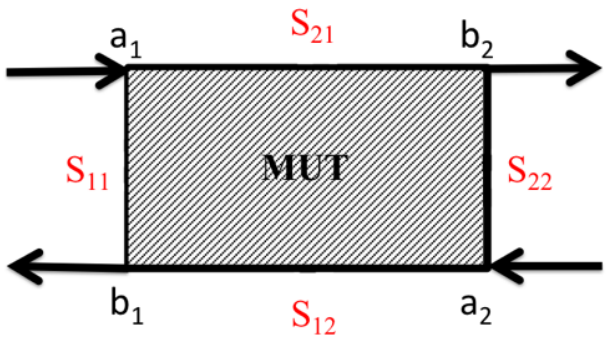

Figure 2.9: Scattering parameters for a two-port network.

A one-port measurement would only acquire S_{11} or S_{22} measurements (i.e., reflection-only). A two-port measurement acquires four parameters, of which two of those parameters are the reverse of the forward parameters, i.e., $S_{11} \approx S_{22}$ and $S_{12} \approx S_{21}$. When processing scattering parameters for a non-magnetic material ($\mu_r = 1$) to determine electrical properties, solutions can be found using either S_{11} or S_{21}. Moreover, if losses are low, the relative uncertainty in the dielectric loss, ε'', is significantly lower for S_{21} when the transmitted signal is greater than -40 dBm. Conversely, if losses are high, uncertainties in S_{21} can increase significantly [31]. Since the choice of scattering parameter is driven by the lossy or dissipative nature of the material being studied, analysis of simulant soils will be needed to identify which

parameter is appropriate. For example, for very dry soils where ε' is expected to be $\sim 10^{-1}$, S_{21} parameters would be used.

2.4 Acquiring Complex Permittivity

In order to extract permittivity data from S-parameters, these data must be processed through an inversion algorithm (this is not the calibration algorithm). Inversion algorithms can be divided into two groups—iterative and non-iterative—and require knowledge of the sample position within the waveguide (non-iterative) and an initial guess of the value of the complex permittivity (iterative). There are several algorithms that can be used for this purpose, but each has its limitations [31–33]. Each of these algorithms assumes the MUT is homogeneous, which is a particularly difficult assumption when considering porous media, which, in general, are considered heterogeneous because non-uniform pores are present. This generalization is especially appropriate for soils, which are mixtures of pores, organic matter, mineral grains of varying size/hydration state, and moisture content. However, homogeneity (spatial invariance) can be closely approximated by eliminating organics, ensuring samples are well mixed, and minimizing the particle size distribution and sample size.

S-parameters require processing to solve for the complex permittivity and permeability. Weir, 1974 developed a procedure to solve for these parameters using the following equations:

$$\mu_r = \frac{1+\Gamma}{\Lambda(1-\Gamma)\sqrt{\frac{1}{\lambda_0^2}-\frac{1}{\lambda_c^2}}} \tag{2.9}$$

$$\frac{1}{\Lambda^2} = -\left[\frac{1}{2\pi d} ln\left(\frac{1}{T}\right)\right]^2 \tag{2.10}$$

$$\varepsilon_r = \frac{\left(\frac{1}{\Lambda^2}-\frac{1}{\lambda_c^2}\right)\lambda_0^2}{\mu_r} \tag{2.11}$$

where d is the thickness of the sample, λ_c is the cutoff wavelength (corresponds to the cutoff frequency), λ_0 is the free space wavelength, and Γ, T are the reflection and transmission coefficients, respectively [33]. All soil simulants used in this research were considered non-

magnetic ($\mu_r = 1$), therefore permeability calculations were not performed. However, an instability exists which causes discontinuities for samples whose thickness approaches $\frac{\lambda}{2}$ and results in phase uncertainty of reflection S-parameters [32].

To avoid instabilities, iterative inversion techniques can be used. One such iterative process, a genetic algorithm (GA), can be employed to process S-parameters to solve for the complex permittivity and has been used by others [34]. GAs use an optimization/search technique based on a natural process that mimics biological evolution [35]. GAs are computationally intensive ($O(n^3)$), requiring long processing times. In order to approach a solution, the algorithm randomly selects individuals from a numerical population to use as parents to produce the next generation. Parents are chosen based on a fitness function that carries parameters for the solution. This process is repeated until a solution is found that best matches the fitness function. The fitness function is based on the minimization of the difference between the measured scattering parameters and the modeled scattering parameters, i.e.,

$$Min\left[S_{21measured} - S_{21modeled}\right] \tag{2.12}$$

The modeled scattering parameters are computed using a cascaded network approach.

2.4.1 Cascaded Networks

Single two-port networks can be defined using transmission line theory in which the complex permittivity of an unknown material (with wave impedance Z_1) can be determined by conveniently defining a 2x2 transmission (or ABCD) matrix (Fig. 2.10). These ABCD parameters can also be used to define scattering parameters S_{21},

$$S_{21} = \frac{2}{A + \frac{B}{Z_0} + CZ_0 + D} \tag{2.13}$$

where Z_0 is the wave impedance of air and the ABCD parameters for a transmission line are defined as follows:

$$A = cos\beta\ell \tag{2.14}$$

$$B = jZ_n sin\beta\ell \tag{2.15}$$

$$C = \frac{jsin\beta\ell}{Z_n} \tag{2.16}$$

$$D = cos\beta\ell \tag{2.17}$$

Transmission line theory defines the wave impedance for TE waves as,

$$Z_n = Z_{TE,n} = \frac{\eta_n k_n}{\beta_n} \tag{2.18}$$

where ℓ is the characteristic length, β is the propagation constant, η is the intrinsic impedance, and k is the wavenumber. The subscript n denotes the medium over which the wave impedance characterizes. Moreover, S-parameters can be used to characterize microwave networks with an arbitrary number of ports, i.e., networks consisting of a cascaded connection of two or more two-port networks. Figure 2.11 displays an example of a cascaded network containing an unknown material supported by backing material on either side. This network can be defined similarly with ABCD parameters. Once matrices have been defined for each material, they can be combined via matrix multiplication to form a single matrix. This configuration was used to processes scattering parameters for all soils measured because backing materials were used to contain soil samples within the sample cells. Thus, modeled scattering parameters (Eq. 2.12) were computed using ABCD parameters (Eq. 2.13) .

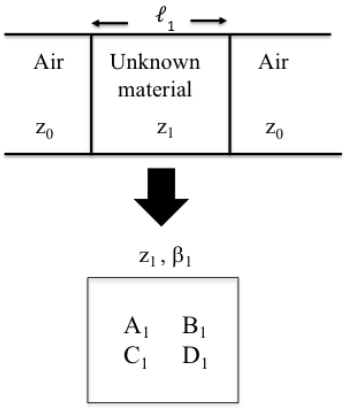

Figure 2.10: ABCD matrix defined for an unknown material in a transmission line bounded by air.

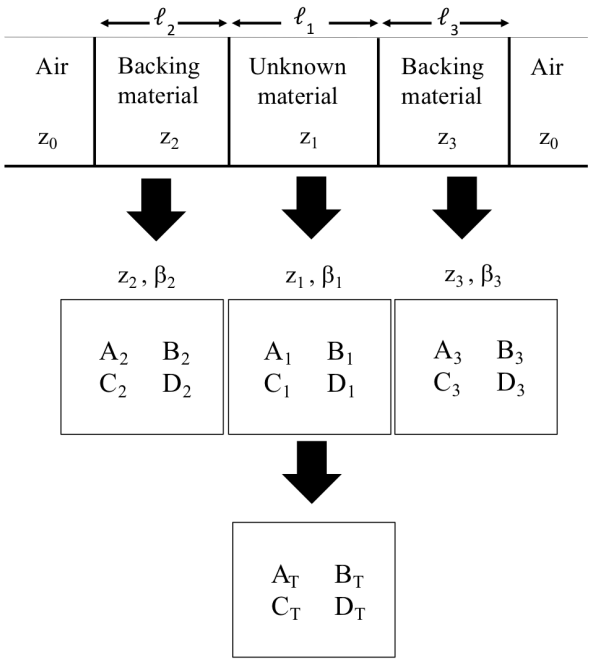

Figure 2.11: ABCD matrix defined for an unknown material in a transmission line bounded by backing material and air. The $ABCD_T$ matrix is the result of matrix multiplication of $ABCD_1$, $ABCD_2$, and $ABCD_3$. For all samples processed in this dissertation $ABCD_2$= $ABCD_3$.

2.5 Network Analyzer Parameters

Several built-in tools were used to condition the signal transmitted to the transmission lines and included utilizing a reflection subtraction tool (gating), sweep averaging, and adjustments to the instrument input power and intermediate frequency bandwidth (IFBW). These steps were taken due to the nature of the measurements acquired in this research. In general, measurements (taken at room temperature on solid media) could be processed with default parameters (i.e., Power: $-17\,\mathrm{dBm}$, IFBW: $35\,\mathrm{kHz}$); however, for low temperature, granular materials, default settings resulted in noisy, widely varying results.

In terms of gating, reflections are expected to occur at any interface that deviates appreciably from ideal. For example, a coating of dust inside the waveguide will produce signal reflections. However, gating is designed to pinpoint (in the time domain) the strongest reflection (i.e., the sample) such that smaller, indiscriminate reflections can be eliminated. Minimizing noise by adjusting the "noise floor" can be achieved by averaging and reducing the IFBW and power settings [36]. Sweep averaging calculates an exponentially weighted average of the 201 data points from each sweep. The disadvantage of these setting adjustments is that the sweep processing time increases significantly. Lowering these settings reduces noise and error; therefore, given the low temperature of measurements performed on soil samples, the power was increased and the IFBW was lowered considerably.

Chapter 3

OVERVIEW OF FACILITIES AND COMPONENTS

As described in Chapter 1, subsurface water extraction techniques would significantly benefit space exploration and further manned exploration of bodies in our solar system. In order to explore the impact of environmental conditions on dielectric loss and heating of simulant soils, it was necessary to simulate the near-surface environment of Mars. This required the use of the Mars Environmental Simulation Facility (MESF) located at the University of Washington. This facility has the capability to simulate conditions consistent with the near-surface of Mars and has been used to analyze atmospheric water extraction [7].

3.1 Mars Environmental Simulation Facility

The MESF (Fig. 3.1) is a continuous flow system in which CO_2 (from a pressurized cylinder) is drawn through a conditioning section (humidity control) to a vacuum pressure vessel by a vacuum pump through electropolished stainless steel tubing. The conditioning section consists of a circulating bath, saturator, and dryer. A NESLAB RTE-4 circulating bath filled with antifreeze solution is used to maintain $-14°$ C within the saturator (a device used to generate humid CO_2 in the simulation facility [1]). A chilled-mirror hygrometer is located downstream of the conditioning section and pressure vessel. Humidity conditions set in the conditioning section are validated with this instrument. All waveguide measurements were performed in a vacuum pressure vessel that was mounted in a SO-LOW C85-5 freezer (located between the conditioning section and the hygrometer). The waveguide assembly (including

[1]Due to the nature of the research in this dissertation, humidity control was not utilized, therefore the circulating bath and saturator were not used.

sample cells) was either installed inside the pressure vessel or directly in the freezer for all measurements.

3.1.1 Dryer

The dryer is comprised of a cylinder with coiled tubing mounted in a rectangular container constructed of metal sheeting. Metal beads inside the cylinder served to increase the surface area for water vapor condensation. Thermal insulation covers the exterior of the container (Fig. 3.2). Prior to this research, the cylinder was immersed in an alcohol/dry ice slurry with the purpose of condensing impurities (primarily water vapor) from the flowing gas (CO_2) prior to exiting the dryer; thereby, providing a very dry gas for subsequent mixing with the humidified gas exiting the saturator. Initial measurements of the flow humidity inside the pressure vessel reached very low frost point temperatures ($-90°C$) when the freezer was cooled to $-80°C$. When the dryer was immersed in liquid nitrogen, the frost point did not change appreciably ($< 5°C$). Furthermore, the frost point was unaffected by the metal "condensation" beads. This confirmed that the gas supplied by the CO_2 cylinder (Praxair CD 4.8RS, 99.998 % purity, 3 ppm H_2O) was sufficiently dry for the experiments described in this dissertation. Therefore, the alcohol/dry ice slurry was not used, and the metal beads were removed.

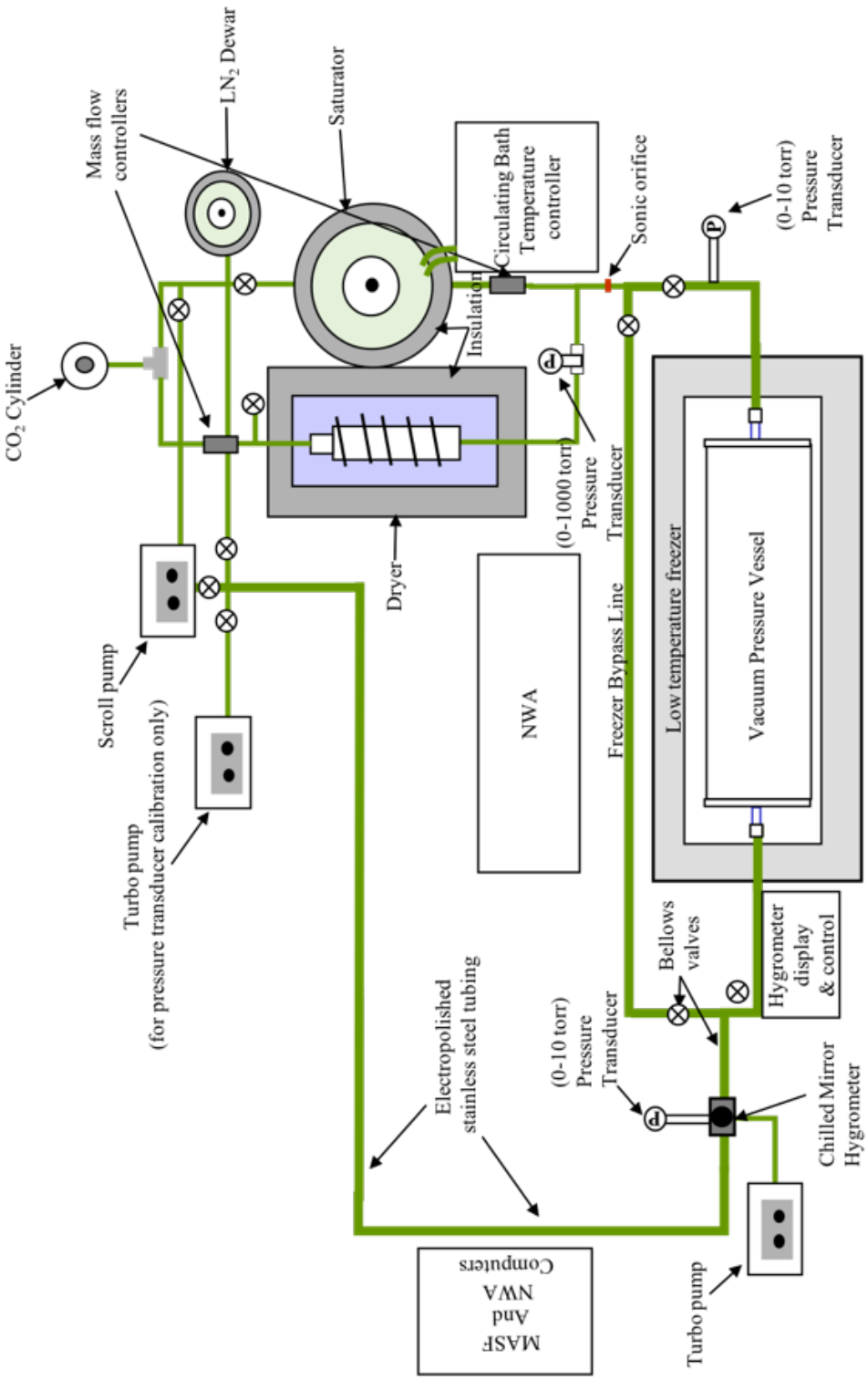

Figure 3.1: Detailed diagram showing a bird's-eye view of the facility in its operational configuration (modified from Schneider, 2013).

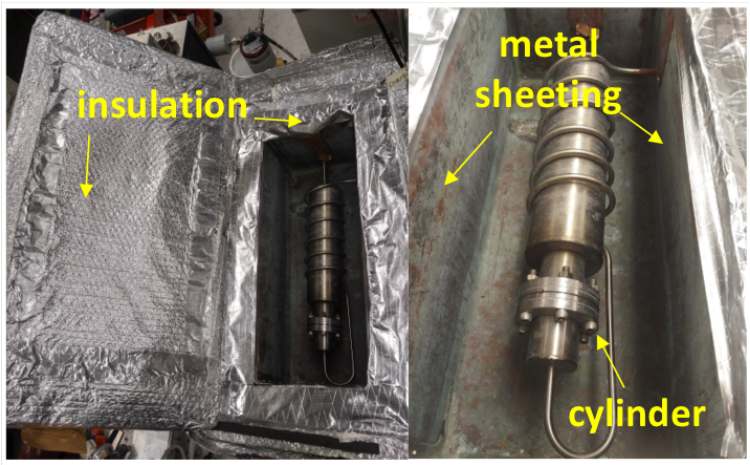

Figure 3.2: Dryer apparatus covered with thermal insulation (left), close-up view of cylinder and coiled tubing (right).

3.1.2 Hygrometer

A Buck Research Model CR-2 chilled mirror hygrometer was used to determine the humidity of the flow in the pressure vessel. The instrument consists of a gold-plated copper mirror, temperature sensor, heating coil, closed cycle helium Stirling pump cryocooler and evacuated isolation chamber, optical module, and control circuitry. The optical system is calibrated to detect condensed volatiles and maintain a condensate film thickness on the copper mirror. To maintain the prescribed film thickness, the mirror is cooled or heated via the cryocooler and heating coils, respectively. The mirror temperature is shown on the display module. When the condensate film thickness is being maintained (i.e., in controlling mode), the displayed mirror temperature is interpreted as a frost or dew point of the flow. In order to achieve very low frost point temperatures, the instrument manufacturer recommended maintaining the isolation chamber at $< 10\,\mathrm{mTorr}$. To achieve this pressure, the isolation chamber was continuously evacuated via a vacuum turbopump.

3.1.3 Vacuum Pumps

An Agilent Technologies SH-110 dry scroll Vacuum Pump was used to evacuate the MESF and was the primary pump used for all measurements. An IDP-3 dry scroll vacuum pump was used separately to evacuate the isolation chamber of the CR-2. Additionally, a Pfeiffer Vacuum TMU 071p turbopump and Residual Gas Analyzer (RGA) were used for pressure transducer calibration, MESF leak testing, and was also used to continuously evacuate the CR-2 isolation chamber when the IDP-3 was not in use. Helium leak testing with the Pfeiffer turbopump was accomplished using Stanford Research Systems (SRS) RGA software. Both scroll pumps maintained facility pressure at $\leq 5\,\mathrm{mTorr}$.

3.1.4 Electrical Components

Simulated atmospheric flow rates were controlled via two MKS Instruments mass flow controllers. The higher range controller (2000 sccm, N2 equivalent) is located upstream of the

dryer. The lower range controller (200 sccm, N2 equivalent), located in the conditioning section of the facility, was not used in this research.

Pressure within the facility was monitored via three MKS Baratron® Type 622A absolute pressure transducers (10 torr (2) and 1000 torr (1) Full Scale Range). The transducers were calibrated using both the scroll pumps and the turbo pump to establish base pressure. Zero adjustment pressure requirements for transducer calibration were $< 5 \times 10^{-4}$ torr and $< 5 \times 10^{-2}$ torr for 10 torr and 1000 torr transducers, respectively. Minimum pressure achieved at the turbopump during base pressure calibration was $\leq 1.6 \times 10^{-5}$ torr.

3.2 Network Analyzers and Facility Software

Agilent Technologies E8364C-PNA (operating range: 10 MHz – 50 GHz) and 8720ES (operating range: 50 MHz – 20 GHz) Microwave Network Analyzers (NWA) were used for all measurements. The 8720ES was used exclusively for dielectric probe measurements and was not integrated into the MESF. The E8364C-PNA was mounted next to the freezer (Fig. 3.1). Port connections on the analyzer (3.5 mm) were connected to microwave cables that were installed through the freezer lid (Fig. 3.3)

Both network analyzer instruments operated with proprietary software from Agilent. This software (85071: Materials Measurement Software) was used to process or store all data collected from the NWA instruments. In addition to the NWA software, the facility's mass flow controllers, thermocouples, and pressure transducers were controlled and/or monitored using LabVIEW programs developed when the facility was initially operated [7].

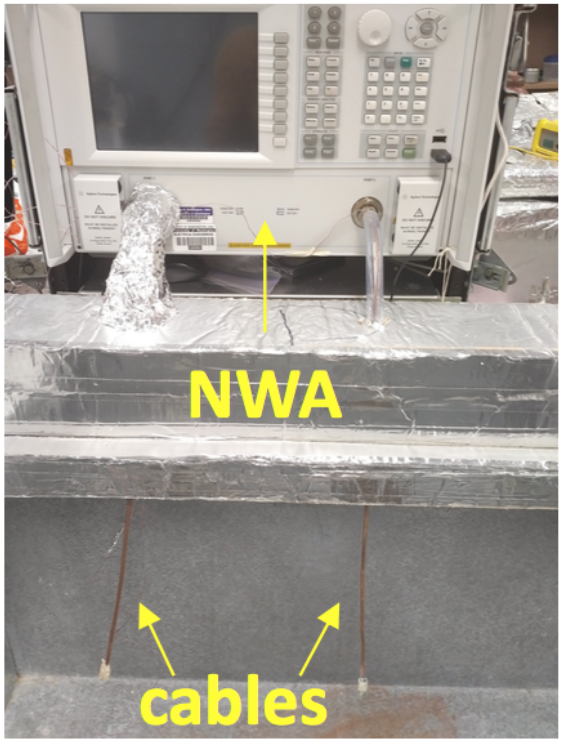

Figure 3.3: Microwave cables connected to the E8364C-PNA network analyzer instrument and installed through customized freezer lid.

3.3 Constructed Components

Several components used in this research were custom designed, machined, and assembled to integrate with the existing facility. These included a vacuum pressure vessel, sample cells, and freezer lid. Each of these components are new contributions to the MESF facility based on the research contained in this dissertation and were uniquely designed to integrate with the existing facility.

An 8-inch thick customized lid constructed from Rmax Thermasheath-3 polyisocyanurate rigid foam was designed to replace the original facility freezer lid. The customized lid allowed access to the freezer interior via a plug-type insert (Fig. 3.4) and included drilled channels for microwave cable installation.

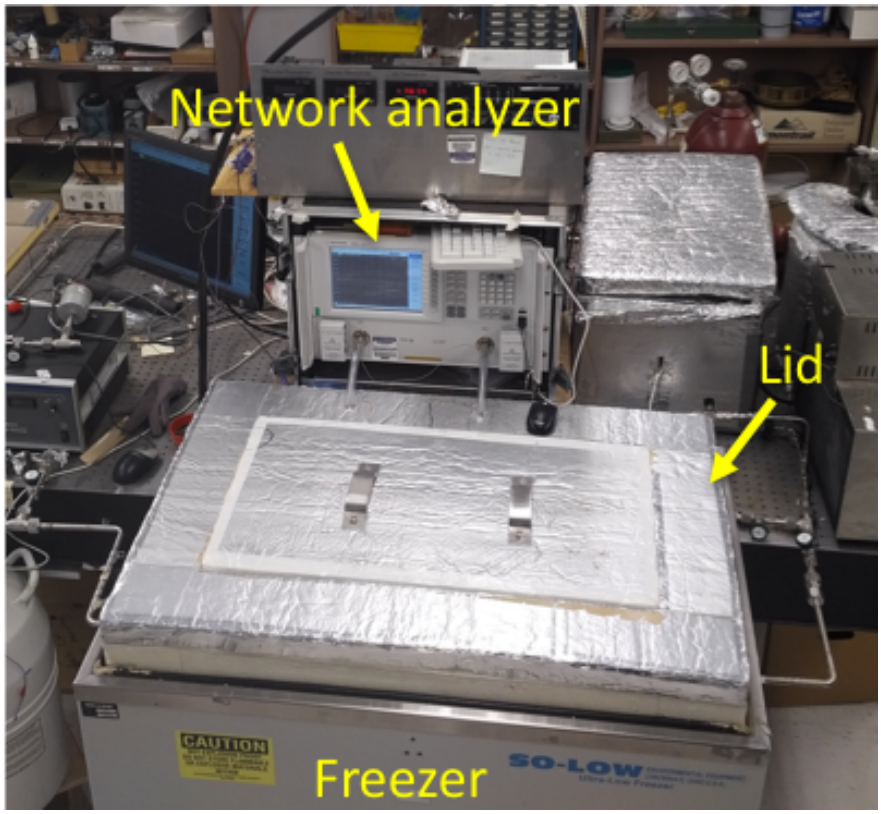

Figure 3.4: Customized freezer lid. Provided access to the freezer interior via plug-type insert (pictured with handles). Image displays exterior view of lid, plug extends an additional four inches into the freezer, totaling eight inches in overall thickness.

3.3.1 Vacuum Pressure Vessel

A pressure vessel, mounted inside the freezer and connected to the MESF's flow-through system via electropolished stainless steel tubing, contained the waveguide assembly. The vessel was constructed from a 10.0-in-ID aluminum tube with $\frac{3}{8}$-in wall thickness that was machined to a length of 22.5 in. An aluminum 13.25-in ($\frac{3}{4}$-in-thick) square flange was welded to the tube and $\frac{3}{8}$-in-thick aluminum circular end plates were bolted to the flanges with $\frac{3}{8}$-in, 18-8 stainless steel hex head screws. The flanges were machined to include a groove to fit a silicone O-ring (10.89-in-ID, $\frac{5}{16}$-in thickness, Durometer 70). Through-wall straight connectors with 0.5-in tube fitting terminations were mounted to the end plates with fluorosilicone

O-rings ($\frac{5}{8}$-in-ID, $\frac{1}{8}$-in thickness, Durometer 70A). Aside from the pressure vessel end plates and interior components, the tubing throughout the facility was connected via vacuum coupling radiation (VCR) fittings. Fittings attached to the end plate (through-wall connectors) and within the pressure vessel interior were Swagelok compression fittings. The assembled pressure vessel is shown in Figure 3.5.

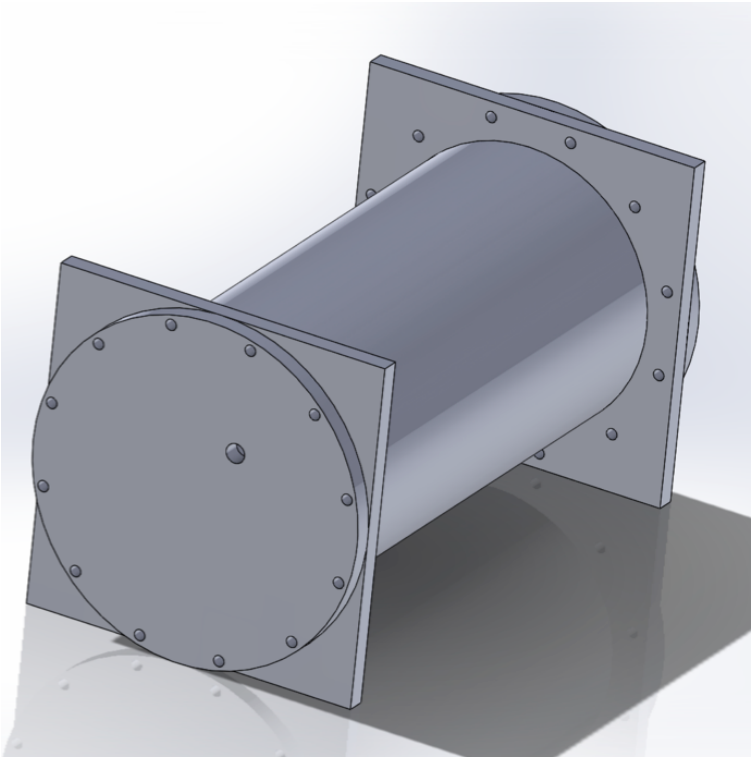

Figure 3.5: SOLIDWORKS image of the fully assembled vacuum pressure vessel. Image displays aluminum tube and circular end plates mounted to rectangular flanges. End plate through-wall connectors and hex head bolts are not shown.

Additionally, two Kurt J. Lesker single-ended, two-pair, Type E thermocouple feedthroughs were mounted to the pressure vessel body and sealed with PTFE O-rings ($1\frac{1}{8}$-in-ID, $\frac{1}{8}$-in thickness). The metals used in these Type E thermocouples are chromega® (nickel-chromium) and constantan (copper-nickel), with an operating range from $-270°$C to $1000°$C. Additionally, two Huber & Suhner thermal vacuum, hermetically-sealed SMA jack adaptors

were mounted to the pressure vessel body and sealed with silicone O-rings. It should be noted that O-rings were used only for room temperature measurements. For low-temperature measurements, all O-rings seals were replaced with indium wire (diameter $\geq$0.070 in) because silicone, fluorosilicone, and Teflon were not suitable to maintain vacuum pressure.

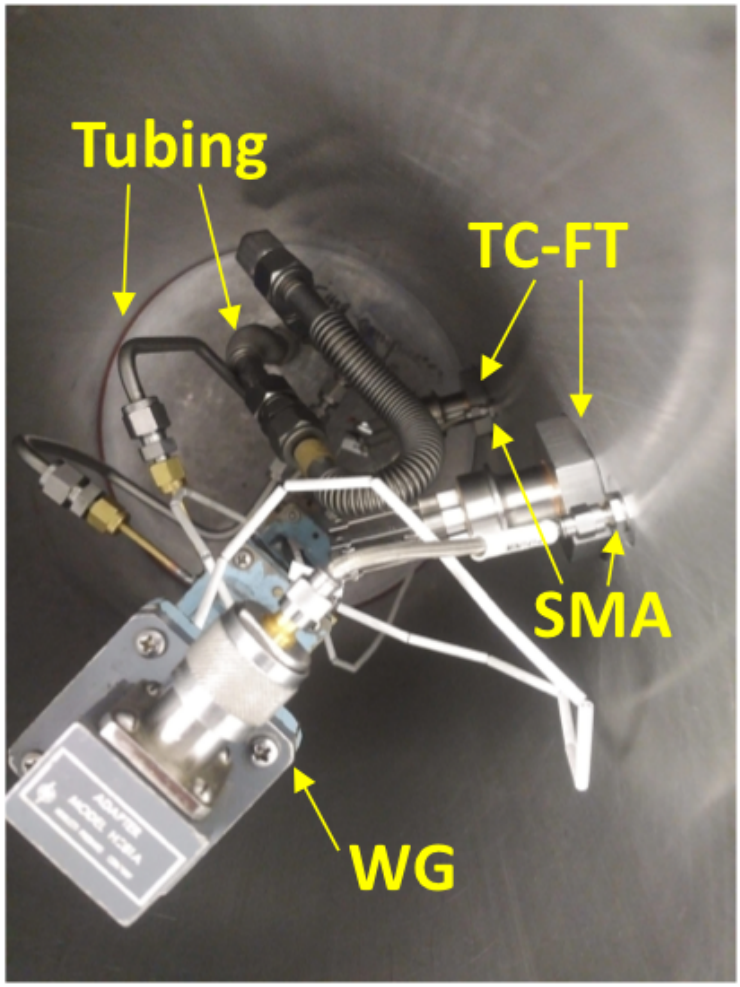

Figure 3.6: Waveguide assembly mounted inside vacuum pressure vessel. Components visible in this image include thermocouple feedthroughs (TC-FT), H-band waveguide and coax-to-waveguide adaptor (WG), SMA wall adaptors (SMA), and flow tubing.

Indium wire (acquired from Indium Wire Extrusion) was used to make gaskets for low-temperature sealing (as noted above, O-rings were not effective due to brittleness at low

temperatures [silicone, fluorosilicone] or were not reusable [Teflon]). Once compressed, indium gaskets, formed from the compression of indium wire between the flange and end plates of the pressure vessel, demonstrated reusability (i.e., achieved vacuum base pressure) by as many as 10 re-uses per gasket. In other words, after initial compression, the pressure vessel end plates were removed and re-bolted at least 10 times before needing to apply uncompressed indium wire to the pressure vessel flange.

The interior of the pressure vessel housed the waveguide assembly, which included waveguides, a sample cell, connecting stainless steel tubing (including flexible tubing), and microwave cables (Fig. 3.6). Tubing connected to the sample cell directed flow from the sample cell, through the tubing, to the end plate (connections made via Swagelok compression fittings) where the flow exited the pressure vessel and routed to the vacuum scroll pump (via the hygrometer) (Fig. 3.1). Microwave cables connected the SMA jack adaptors to the waveguides via coax-to-waveguide (N-type) adaptors (Fig. 3.6). An assortment of microwave cables was used in the waveguide assembly and the exterior of the pressure vessel (Table 3.1). Cables outside the pressure vessel connected the SMA jack adaptors to the network analyzer via SMA terminations.

Table 3.1: List of Microwave cables. All cables were rated for the 2.0 – 20 GHz range (TEM mode). Ultiflex cables were used for preliminary work and were not used in the pressure vessel.

Manufacturer	Model	Termination	Length [in.]	Temperature Range [°C]
Huber&Suhner	Cobraflex	SMA	20	−269 to +250
Huber&Suhner	Mini141	SMA	4, 6	-55 to 125*
Huber&Suhner	Sucoflex	SMA	20	-55 to 125*
N/A**	Copper	SMA	20	--
Tensolite	Semi-flex 601	SMA	9	-65 to 105*
Micro-Coax	Ultiflex UFA210B	N-type	74	-65 to 165*

*Low temperature limit set by manufacturer's testing equipment, it is not due to expected decreased performance at lower temperatures

**Un-terminated stock copper cables were fitted with SMA terminations and soldered as part of the work of this dissertation

3.3.2 Sample Cells

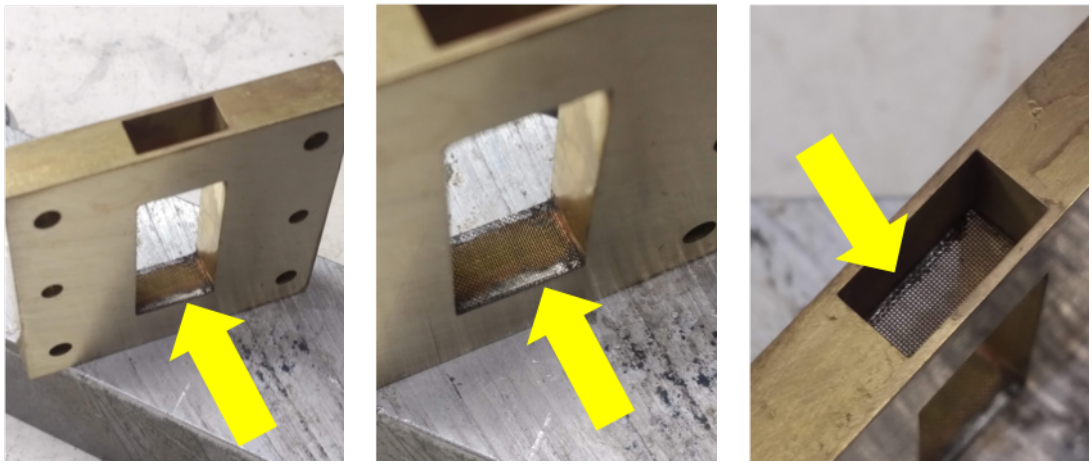

(A) (B) (C)

Figure 3.7: H-band sample cell screens. A) Full view of sample cell, B) close-up view of soldered screen from sample cell cavity interior and C) view from flow port side. These images do not include flow port tubing.

Sample cells, machined from brass, were made for each frequency band (Table 2.2). Construction included milling cavities for soil samples and gas flow, installing interior screens (also constructed from brass) for current continuity and soil containment (Fig. 3.7), and soldering tubing to the flow ports of the sample cells. The most critical dimension of the waveguide technique is the cross-section of the sample cell, which mates to the cross-section of each waveguide (or calibration standard). Proper aperture alignment ensures a seamless interface for electric current to transition from each waveguide to either the sample cell or the calibration standard (Figure 3.8). To achieve this alignment, the dimensions of each sample cell cavity were derived from the mating waveguides to which they would be mounted. The thickness of each sample cell was designed according to optimum thickness parameters as detailed in the Appendix. The collection of sample cells used in this dissertation are shown in Figure 3.9. For high frequency measurements (P, X, and H-bands) slip (i.e., locating) pins were installed to achieve the desired alignment of the rectangular waveguide flanges

to the sample cells. Slip pins were not required for the lower frequency bands (C, G, and S-bands) because the number of mounting screws ensured adequate lineup of the aperture to the circular waveguide flanges.

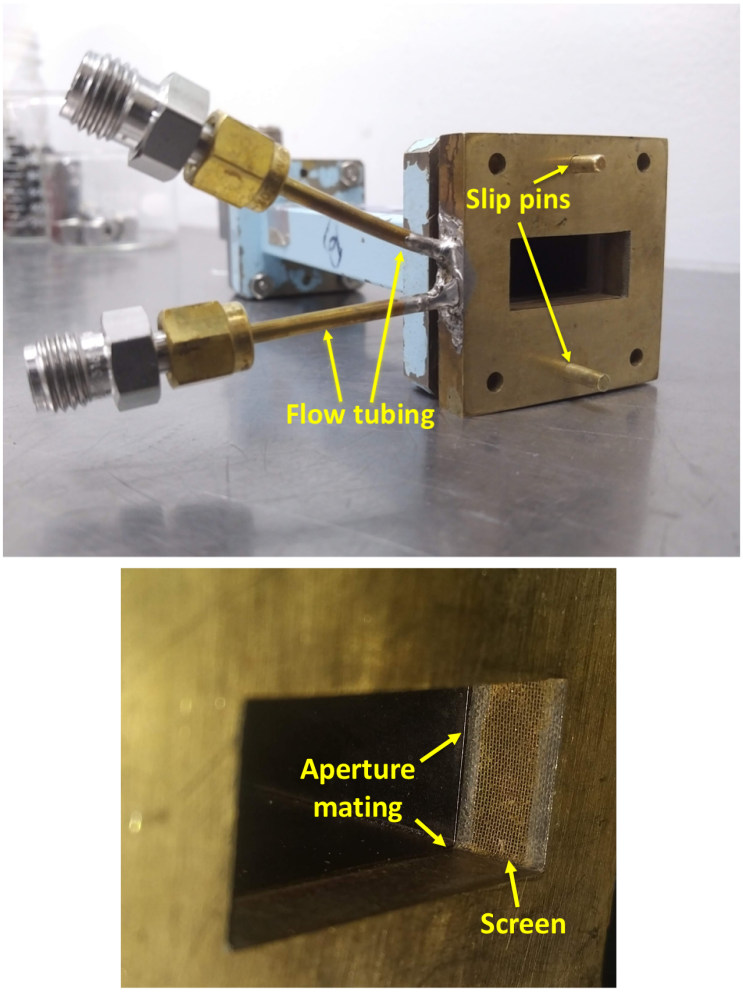

Figure 3.8: H-band sample cell and waveguide displaying slip pins and flow tubing (upper figure) and aperture mating (lower figure).

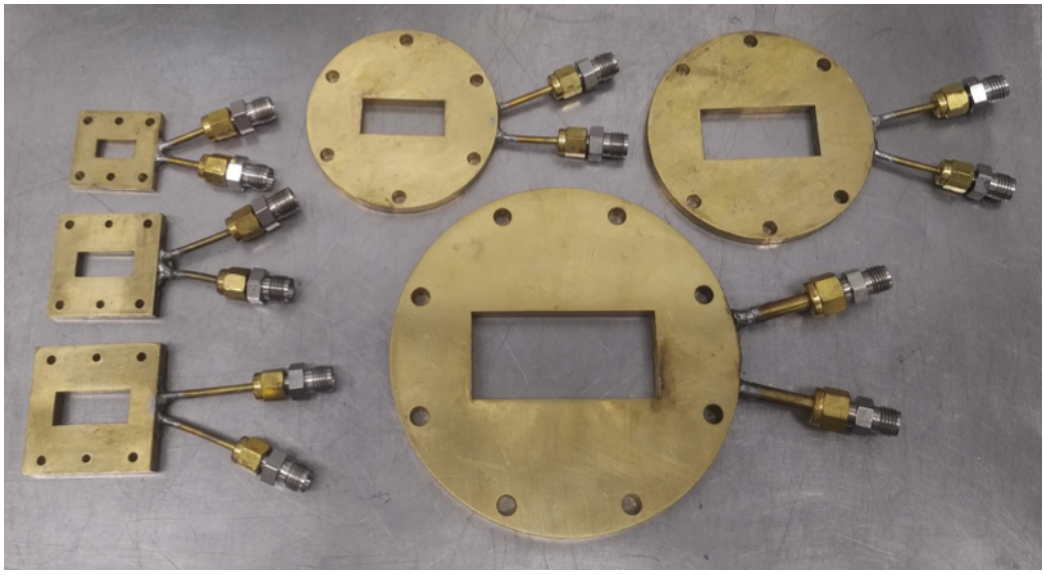

Figure 3.9: Constructed sample cells for the waveguides used in this research. The smallest sample cell (top-left) corresponds to the highest frequency (P-Band). Similarly, the largest sample cell (bottom-right) corresponds to the lowest frequency (S-Band). See Table 2.2 for more information on waveguide bands.

3.4 Materials

Mars simulant soils were the primary material measured with the NWA instruments. However, other materials measured and analyzed in this dissertation included Teflon, sodium perchlorate, and ice.

3.4.1 Mars Simulant Soils

The soil studies included in this dissertation were comprised of three Mars simulants: JSC Mars-1, JSC-RN (Rocknest), and MMS sand (Mojave Mars Simulant). These simulants are manufactured by the Johnson Space Center (JSC) and the Jet Propulsion Laboratory (JPL). The components of each simulant are listed in Table 3.2. Here, the major element composition is listed for each simulant along with a soil sample analyzed at the Chryse site (Viking 2 lander mission) [37]. As displayed in Figure 3.10, a major difference among these

simulants is their appearance—JSC Mars-1 and JSC-RN present as a reddish-brown soil; whereas, MMS presents as a blackish soil. Presumably, the reddish color of JSC Mars-1/RN can be attributed to higher concentrations of iron oxide (Fe_2O_3) when compared with MMS (Table 3.2) [37–39]. Additionally, the source material of these simulants is quite different. JSC Mars-1 is a palagonitic tephra (glassy, basaltic, meteorically altered volcanic ash) mined from the Pu'u Nene cinder cone, located on the island of Hawai'i. The source material for MMS is mined from basalt excavated from the Saddleback Mountains in the Mojave Desert and is crystalline in texture. JSC-RN is a mixture of MMS and other minerals (including pyrite, ferric sulfate, ferric oxide, and forsterite). Interestingly, the manufacturer of MMS was motivated to produce an alternative simulant due to the hygroscopicity of JSC Mars-1 [38] (Section 1.1). Yet, JSC-RN was specifically developed to mimic the water-bearing properties (1 – 3 wt.%) of aeolian sand detected by the Sample Analysis at Mars (SAM) instrument (Curiosity rover) of evolved water (from adsorption, hydrated salts [e.g., perchlorates], etc.) at the Rocknest sampling site (Gale Crater, Mars) [40]. All simulants are mostly comprised of metallic oxides but JSC Mars-1 and MMS contain neither perchlorate salts nor hydrated minerals. Due to the hygroscopic nature of the perchlorate salts that have been detected on the near-surface of Mars [41–45] and the water extraction focus of this research, it was useful to develop simulant mixtures containing these salts. Thus, to simulate perchlorate salt content consistent with observations from Mars, subsets of JSC Mars-1 and MMS simulants were doped with 1.5% sodium perchlorate ($NaClO_4$). Also, researchers at Johnson Space Center developed JSC-RN to support component and system testing for water extraction; thus, the JSC-RN simulant also contains $NaClO_4$ (1%) and hydrated oxides that contribute to low-temperature water release [46].

3.4.2 Sodium Perchlorate

Perchlorate mixtures of JSC Mars-1 and MMS were developed for this research by preparing samples that contained 1.5% anhydrous sodium perchlorate ($NaClO_4$—CAS:7601-89-0), acquired from Thermo Fisher Scientific Chemicals, Inc., and sieved to 180 – 246 μm for soil

Table 3.2: Major element abundances for Mars (JSC Mars-1, MMS, JSC-RN) simulants and Viking Lander 2 (Chryse site) sample expressed in weight percent (wt.%).

Major Element Composition	JSC Mars-1 [37]	Mojave Mars Simulant [39]	JSC-RN [39]	Chryse [37]
SiO_2	38.72 – 45.66	47.1 – 49.7	45.8	51
TiO_2	3.24 – 3.57	0.87 – 1.24	1.05	0.76
Al_2O_3	18.53 – 28.01	15.5 – 17.4	13.7	8.5
Fe_2O_3	10.10 – 17.04	10.87	14.72	n.r.
FeO	1.98 – 5.58	0.39 – 1.03†	2.69	n.r.
Fe_2O_3T	15.43 – 19.24	9.73 – 11.30	17.7	19.7
MgO	1.73 – 4.85	4.68 – 7.17	9.51	6.8
CaO	5.32 – 6.21	7.85 – 11.45	7.97	6.9
Na_2O	1.06 – 2.76	2.12 – 4.11	3.05	n.r.
K_2O	0.29 – 0.88	0.33 – 0.58	0.54	n.r.
MnO	0.24 – 0.45	0.14 – 0.19	0.18	n.r.
P_2O_5	0.71 – 1.38	0.09 – 0.25	0.16	n.r.
CrO_3	n.r.	0.04 – 0.06	n.a.	n.r.
Loss on Ignition (LOI)	9.66 – 29.81*	1.24 – 9.79**	n.a.	n.r.

† Fe_2O_3T calculated in this dissertation used the following: $FeO = |Fe_2O_3T - Fe_2O_3| / 1.1113$
LOI measured at 950℃* and 1000℃**, includes H_2O, SO_3, Cl, etc.
n.a. (not analyzed), n.d. (not detected), n.r. (not reported)

mixture measurements. These mixtures are referred to as JSCp and MMSp for JSC Mars-1 and MMS perchlorate mixtures, respectively. Direct measurements of sodium perchlorate were performed with large ($> 250\mu m$) and small ($< 180\mu m$) grain sizes.

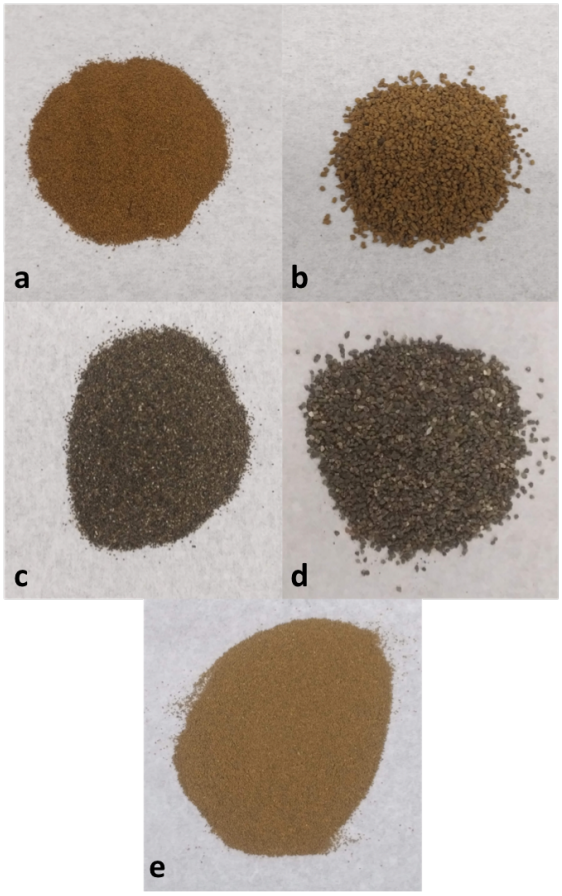

Figure 3.10: Mars simulants used in soil studies. a) JSC Mars-1: grain size 180 – 246 μm, b) JSC Mars-1: grain size 850 – 991 μm, c) MMS: grain size 180 – 246 μm, d) MMS: grain size 850 – 991 μm, e) JSC-RN: grain size 180 – 246 μm. MMS sand is comprised of particles ranging from $\sim$3 μm to 2 mm, ($\sim$50% $\leq 200\mu m$) [38]. In comparison, JSC Mars-1 has a similar particle size distribution: 5 μm to $\sim$1 mm, with $\sim$50% $\leq$ 250 μm. JSC Mars-1 and MMS mixtures containing perchlorate, visibly similar to their base simulants, are not shown. Samples used for energy coupling experiments (Chapter 6) were not sieved.

Chapter 4

FEASIBILITY STUDY AND RESULTS

Dielectric heating of the subsurface of Mars requires an understanding of the interaction between microwave radiation and heterogeneous subsurface components, i.e., silicate minerals, water content, salinity, etc.—all of which contribute to the lossiness of the soil. This lossiness can be interpreted as the effectiveness of energy dissipation during dielectric heating. The purpose of the feasibility study was to assess transmission line measurement techniques (coaxial and waveguide) for compatibility with measuring heterogeneous particulate materials (i.e., soil mixtures) at temperatures consistent with the subsurface of Mars (i.e., $\sim -80°C$). Results contained in this chapter will be used to formulate the methods for testing simulants described in Section 3.4.1.

Others have reported complex permittivity results for soils and planetary simulants at ambient [47], vacuum [48], and low temperature [9, 49] conditions using waveguides, coax transmission lines, and cavity resonators at microwave frequencies. However, little has been reported on measurements of soils using reflection techniques with coaxial transmission lines. In general, coaxial transmission lines can be configured for reflection-only (dielectric probe) and transmission (coaxial-airline) measurements. Transmission measurements with coaxial-airlines are more common but would be more challenging to integrate with the MESF than dielectric probes.

Ethridge and Kaukler, 2009 performed permittivity experiments on lunar and Mars analog simulants at ambient and low temperature conditions with waveguides, but exact details of these measurements were not discussed. Moreover, it is unclear how the low temperature measurements were calibrated. If calibration conditions are inconsistent with measurement conditions, errors in the scattering parameters are likely to occur. Additionally, waveguides

can provide more accurate results than coaxial lines, as discussed in Chapter 2, but soil permittivity across a broad frequency range with waveguides has not been published.

As described in Chapter 2, prior to performing measurements, waveguides are calibrated (commonly at room temperature) to determine the temporal location of the measurement plane, which is based on the time it takes for the signal leaving the NWA to reach the calibration standards. Spatially, the measurement plane exists at the waveguide/sample interface. However, if the temperature of the waveguide system is not uniform during measurement acquisition, thermal expansion effects (at very low temperatures) can shift the waveguide/sample interface significantly, resulting in mis-alignment of the measurement plane (Fig. 4.1). A relatively small temperature change, ΔT, between the sample and waveguide may not generate an appreciable alignment shift; however, to simulate the low temperature conditions of Mars (ΔT$\approx$ 100°C), significant shifting ($\sim$2 mm) is expected. To prevent mis-alignment during low temperature measurements, it was necessary to also calibrate the waveguide system at low temperature.

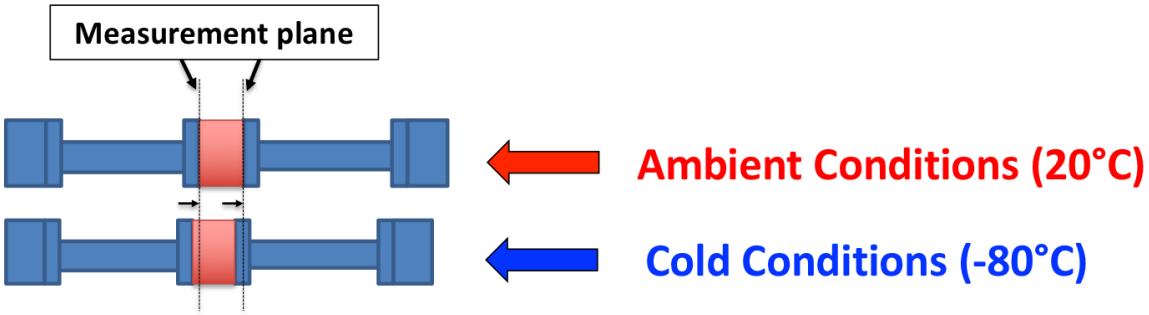

Figure 4.1: Mis-alignment between waveguide/sample interface and measurement plane at ambient conditions (upper figure) vs cold conditions (lower figure) with identical calibrations (i.e., performed at ambient conditions).

Thus, the experiments discussed in this chapter address coaxial reflection soil measurement feasibility with a series of experiments using a dielectric probe. These experiments are repeated using a waveguide transmission line for comparison. Also, to assess low temperature capabilities with a waveguide transmission line, experiments were performed using Teflon.

4.1 Dielectric Probe Measurements

Broad frequency bandwidth is a major advantage of using coaxial transmission line methods. However, coaxial techniques for transmission measurements (coaxial airlines) are difficult to integrate into a flow-through system, such as the MESF. Reflection measurements, on the other hand, with a dielectric probe can be easily integrated by placing the probe directly on or in soil samples. The dielectric probe can provide broadband permittivity results of solid, semi-solid, and liquid materials. Although the frequency bandwidth is much broader when compared to waveguides, acquiring the complex permittivity using the dielectric probe is limited to reflection scattering parameters (i.e., S_{11}, S_{22}).

4.1.1 Materials and Methods

A Keysight N1501A-HT dielectric probe was used for all dielectric probe measurements. The probe consisted of a stainless-steel inner conductor, Inconel outer conductor (with air as the insulating medium), and a borosilicate glass seal separating the conductors at the face of the probe (Fig. 4.2). The probe was connected to an Agilent 8720ES NWA (operating range: 50 MHz – 20 GHz) via coaxial cables (Huber+Suhner: Sucoflex 104) with SMA (SubMiniature version A) connectors. Measurements of Mars simulant soils using the N1501A-HT required samples to be constrained to the dimensions listed in Table 4.1. Assumptions employed by this method are that samples are isotropic, homogeneous, and non-magnetic [50]. In order to comply with these assumptions, simulant samples were sieved to 5.5 – 20 μm (JSC Mars-1 or JSC) and 180 – 246 μm (MMS). These grain sizes are also referred to as JSC Mars-1 silt and MMS sand. Prior to acquiring measurements, the probe was calibrated as discussed in Chapter 2. When acquiring measurements, samples were placed in close proximity to the face of the probe. The probe was rinsed with water and cleaned with isopropyl alcohol between measurements. All measurements were performed within minutes of each other. Sample preparation and measurement procedures were identical for both simulants.

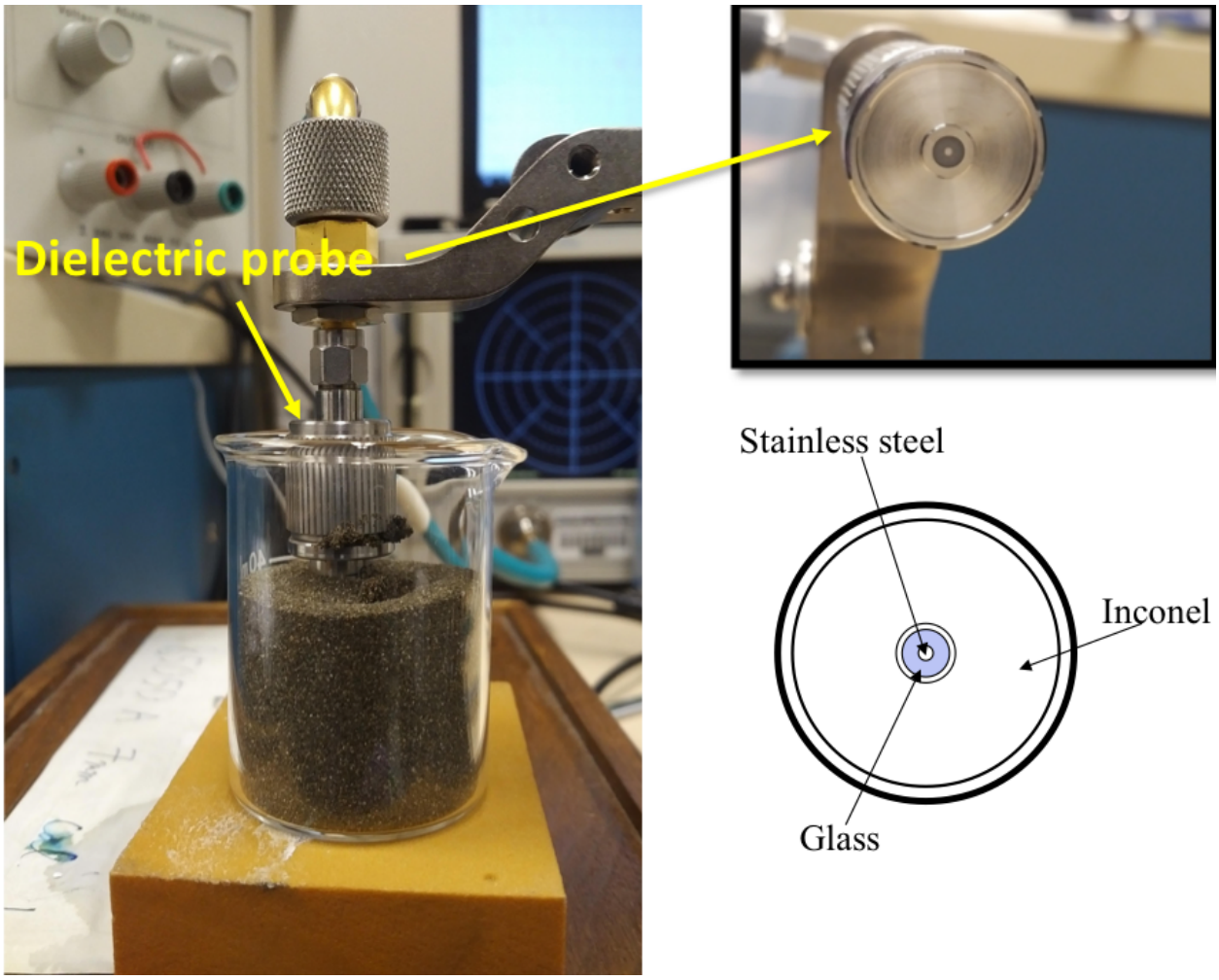

Figure 4.2: Left: Dielectric probe positioned above MMS sand (grain size 180 – 246 μm). Right: Plan views of face of dielectric probe (∼20 mm in diameter).

Table 4.1: N1501A-HT Sample Requirements [50]

Grain size	$< 300\,\mu$m
Sample diameter	$> 20\,\mu$m
Sample thickness	$> \frac{20}{\sqrt{\lvert\varepsilon(\omega)\rvert}} (\sim 12\,\text{mm})$

Simulant samples were measured at two conditions. The first condition simulated the natural settling of the sample (MMS only) around the dielectric probe. In other words, the sample was poured over the probe until the probe was completely immersed. The second condition involved compressing the sample against the face of the probe to insure good contact and avoid air gaps. All JSC Mars-1 measurements were taken at the latter condition.

Software designed for the N1501A-HT instrument (85071D: Materials Measurement Software) processed the scattering parameters in a proprietary manner to determine the complex permittivity of the samples [51].

4.1.2 Results and Discussion

The Phoenix Mars Lander mission to the northern latitudes of Mars measured the electrical permittivity of Mars soils with a thermal electrical conductivity probe (TECP) at 6.25 MHz [52]. Results from these measurements are displayed in Figure 4.3 and show the range of permittivity (real part) is 2.4 – 2.6. Higher permittivity (2.6 – 2.8) is theorized to be a result of overnight deposits of unfrozen (adsorbed) water [6]. However, results reported by others at room temperature seem to vary—3.2 – 3.5 (10.0 MHz – 1.0 GHz: coaxial air line) [53], 3.37 (2.45 GHz: waveguide) [9], and 2.0 – 3.0 (1.0 MHz – 1.0 GHz: coaxial air line) [49]. This discrepancy could be a result of the measurement method and/or techniques used to process scattering parameters. In addition, higher permittivity values could be the result of samples having higher water content.

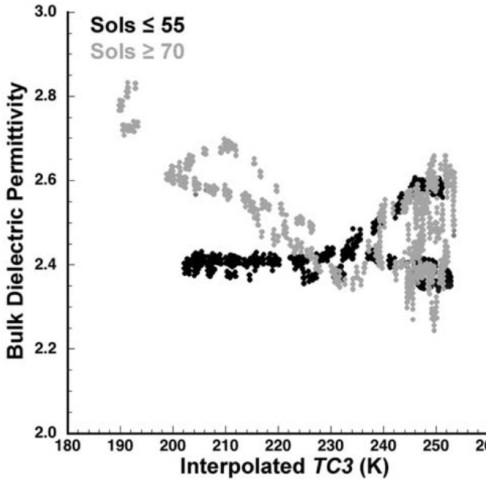

Figure 4.3: Phoenix Mars Lander permittivity (real part) results [52]

Complex permittivity results for JSC Mars-1 and MMS samples taken in the 500 MHz to 20 GHz range using a dielectric probe display similar trends for each simulant (Fig. 4.4). Although JSC results are in good agreement with TECP results (Fig. 4.3), the permittivity of JSC samples appears to decrease linearly from 500 MHz until approximately 10.0 GHz; whereas the permittivity of MMS samples is mostly invariant across the frequency range. Results also indicate higher losses for JSC by a factor of two. This result could be explained by the order of magnitude difference in grain size between the two simulants. Additionally, Figure 4.4 shows significantly reduced values (bold curves) for natural settling (NS) MMS results when compared with compressed results. Due to the design of the dielectric probe and its orientation when mounted (Fig. 4.2), it is reasonable to assume that as samples naturally settle around the probe, significant air gaps can form causing a reduction in the dielectric constant, ε'.

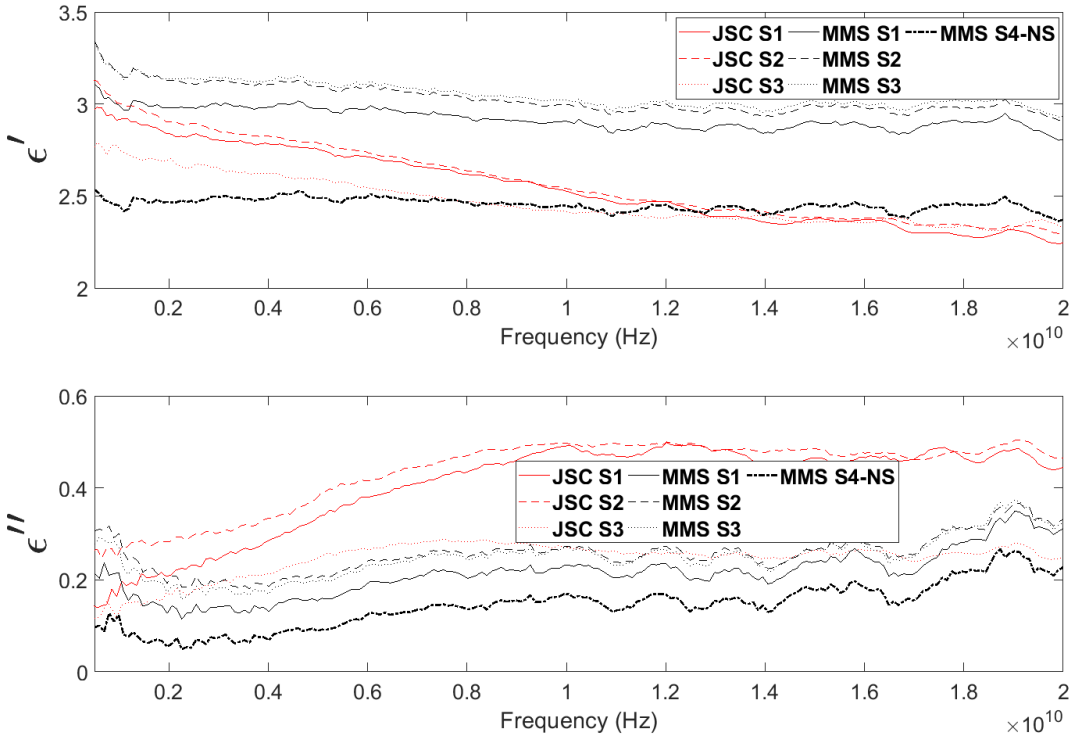

Figure 4.4: JSC Mars-1 silt (grain size 5.5 – 20 μm) and MMS sand (180 – 246 μm) complex permittivity results using a dielectric probe. Curves labeled NS represent samples that were measured under natural settling conditions.

To assess the repeatability of dielectric probe measurements, standard deviation calculations were performed using the population standard, σ, where N is the number of observations, μ is the mean, and x_i are the observed sample values (Eq. 4.1). Deviation results for MMS appear more uniform than JSC results (Fig. 4.5). However, these results bring to question the repeatability of reflection measurements among identical samples, particularly for JSC. Furthermore, it is doubtful that deviations are frequency dependent so the variability observed in JSC samples highlights another limitation to this measurement method.

$$\sigma = \sqrt{\frac{1}{N}\sum_{i=1}^{N}(x_i - \mu)^2} \tag{4.1}$$

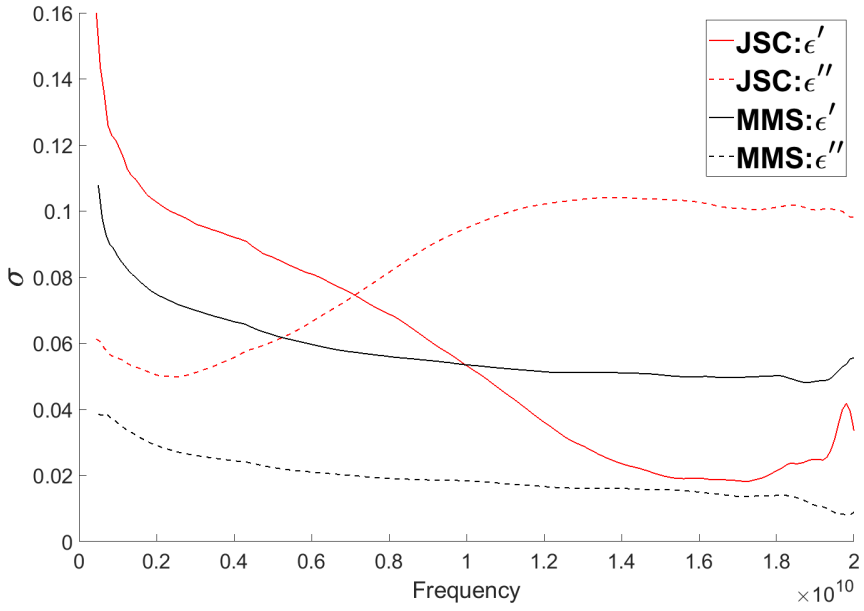

Figure 4.5: Standard Deviation of the complex permittivity of JSC Mars-1 silt and MMS sand. Permittivity results acquired using a dielectric probe.

Results using the dielectric probe offer insight into the limitations of reflection measurements to fully characterize dielectric loss in particulate materials. Given that "measurement repeatability for granular materials is dependent on density variation" [50], it is difficult to ascertain the accuracy of dielectric probe results due to unavoidable variations in samples. Density variation assessment with reflection techniques can vary with grain size, sample configuration (i.e., naturally settled vs. densely packed), or if there is variability in how or where the dielectric probe makes contact with the sample (i.e., reference position). If either of these occur, dielectric loss results can vary significantly between identical soil measurements. In addition, constraining each measurement to ensure conditions were constant also had drawbacks. Even when the dielectric probe was mounted (i.e., fixed reference position) and samples were poured (natural settling), air gaps between the sample and the surface of the probe were difficult to control and impacted measurement repeatability. To mitigate these air gaps, the probe was firmly pressed against the surface of the soil sample. How-

ever, in both cases results varied among repeated measurements. Moreover, should reflection techniques be used for environmental simulations, density variations would only be further compounded when particulate samples undergo cementation due to volatile deposition (e.g., ice forming in the voids between soil grains).

4.1.3 Comparison with Waveguide Method

JSC and MMS samples were also measured with waveguides to acquire reflection and transmission data. In order to compare these measurements with dielectric probe results, soil samples were sieved to the same grain size, to wit: 5.5 – 20 μm and 180 – 246 μm for JSC and MMS samples, respectively. Samples were installed in sample cells with Laird Eccostock polyethylene foam windows for containment (Fig 4.6). Afterward, the sample cells were mounted to the waveguides and connected to the E8364C-PNA (operating range: 10.0 MHz – 50.0 GHz) via coaxial cables. All samples were measured at the X-band frequency range, i.e., 8.2 – 12.4 GHz. After each measurement, the sample cell was detached from the waveguide and the foam windows and soil sample were removed. Prior to installation of subsequent samples, the sample cell was vacuumed to remove any remaining soil grains and the foam windows were cleaned with isopropyl alcohol. X-band waveguides were calibrated prior to all measurements using calibration standards as described in Chapter 2. Scattering parameters were processed with the PNA instrumentation software (85071: Materials Measurement Software) using a 'Transmission Epsilon Fast Model' [51].

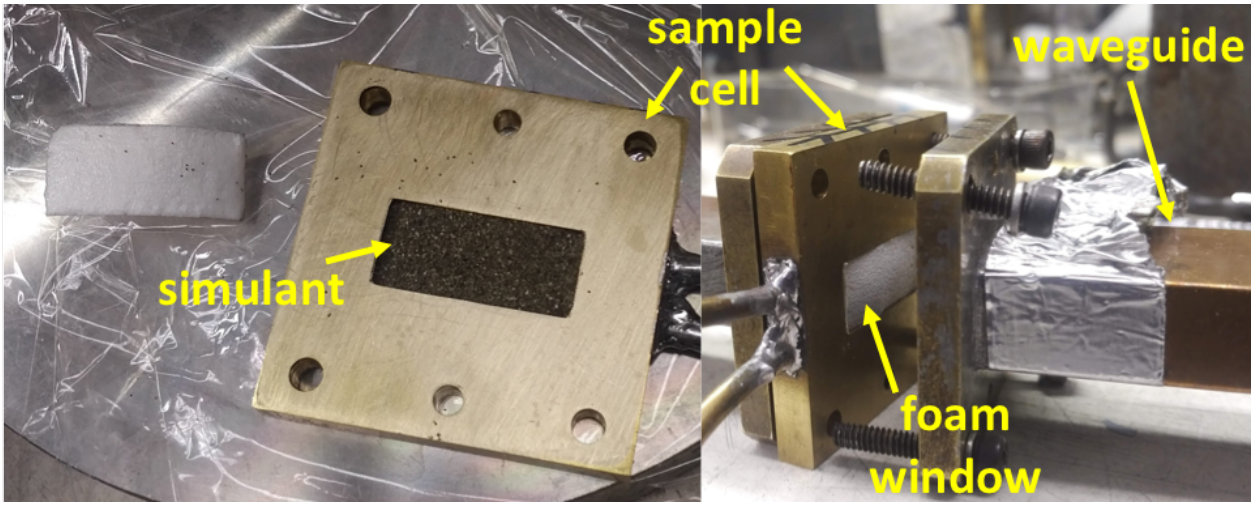

Figure 4.6: Left Image: Soil sample (MMS) installed in X-band sample cell with foam windows (left). Right image: Sample cell (containing soil sample) mounted to X-band waveguide.

Dielectric losses using waveguide techniques show reduced deviations between identical measurements for JSC and MMS samples (Fig. 4.7). Curves from Figure 4.5 are reprinted from 8.2 – 12.4 GHz for comparison with X-band waveguide results. Low variability in these results strongly suggests that transmission waveguide measurements are more reliable in terms of repeatability than coaxial reflection measurements. As discussed in Section 4.1.2, a major disadvantage of using the dielectric probe is controlling the "density" of samples. This issue is circumvented when using waveguides for transmission measurements since the sample volume is constrained and the bulk density is generally conserved for each measurement. Waveguide reflection measurements of JSC and MMS were similar to dielectric probe measurements.

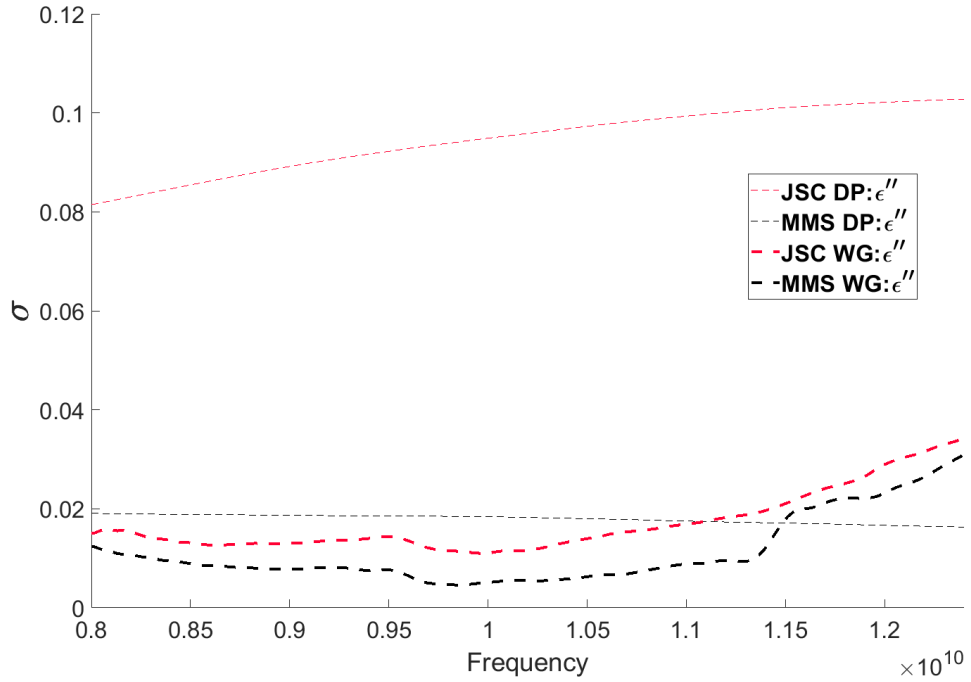

Figure 4.7: Dielectric loss deviations for JSC Mars-1 silt and MMS sand using waveguide (WG) and dielectric probe (DP) measurement techniques.

4.2 Low Temperature Experiments with Teflon

A study with Teflon (polytetrafluoroethylene) samples was performed to determine the effectiveness of waveguide measurements at low temperature. Teflon is an excellent measurement standard due to its known and invariant electrical properties within the 2.0 – 20 GHz range at ambient conditions [54–56]. Although others have reported these properties at cryogenic temperatures (28 – 84 K) [57, 58], they were measured at discrete frequencies. There do not appear to be any published measurements of low temperature Teflon over a broad frequency range to demonstrate its invariance. Thus, to investigate the invariance of Teflon at low temperature across the microwave range of this study, Teflon was measured at room temperature (∼20°C) and low temperature (∼ − 80°C) using six waveguide bands (Table 2.2) to cover the 2.6 – 18 GHz frequency range.

4.2.1 Materials and Methods

Six Teflon samples were machined to fit inside a sample holder for each band as shown in Figure 4.8. It was important that each sample be flush with the surface of the sample holder and free of any gaps. The surface of the Teflon samples was cleaned with isopropyl alcohol prior to installation. Sample holders were mounted to the waveguides as described for soil samples in section 4.1.3. For low temperature measurements, the waveguide system was installed in the SO-LOW freezer. Thermocouples were placed on the sample holders to monitor temperature.

As described in Chapter 2, several software tools were used to condition the signal propagating within the waveguide to reduce noise. The intermediate frequency bandwidth (IFBW) and instrument power were reduced to 10 Hz and -5 dBm (3.16×10^{-3} Watts), respectively. These adjustments reduced the noise floor to -117 dBm (2.0 – 10 GHz) and -120 dBm (10 – 20 GHz) [59]. For low temperature measurements of Teflon, cryogenically-rated coaxial cables (Huber+Suhner: Cobraflex) were used to interface waveguides to the PNA. Similar to soil results (Section 4.1.3), scattering parameters were processed with the PNA instrumentation software (85071: Materials Measurement Software) using a 'Transmission Epsilon Fast Model'.

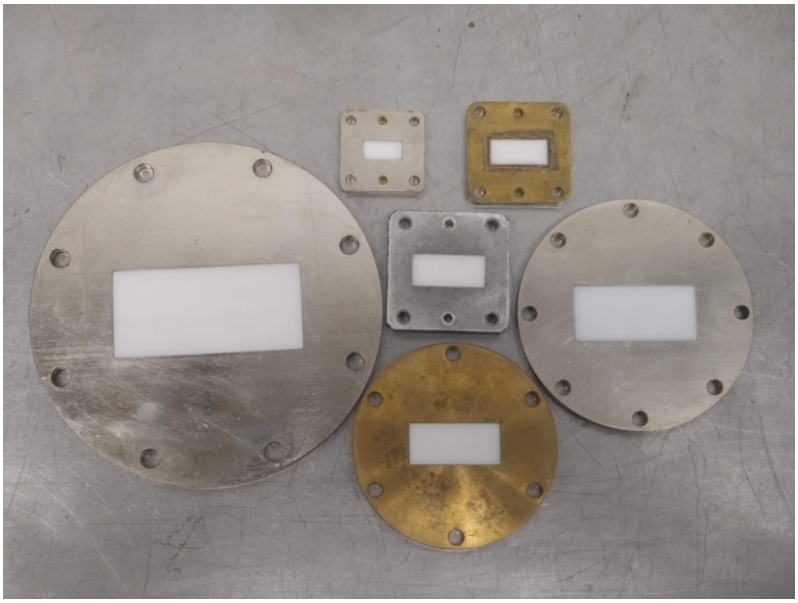

Figure 4.8: Sample holders for the waveguides used in this research. The largest sample holder (left) corresponds to the lowest frequency (S-Band). Similarly, the smallest sample holder (middle-left) corresponds to the highest frequency (P-Band). See Table 2.2 for more information on waveguide bands.

4.2.2 Results and Discussion

Results from this study are shown in Figure 4.9. The top figure shows dielectric constant measurements of Teflon across the six measurement bands at room temperature (solid curves) and ~ -80°C (dashed curves). The lower figure displays dielectric losses. Both figures display gated measurements of Teflon using transmission (S_{21}) scattering parameters. Within each band at room temperature there are slight variations in ε', these variations are also evident at low temperature. Additionally, room temperature measurements appear similar to low temperature measurements and are consistent with the results of others [54, 55, 57, 58]. Losses, ε'', on the other hand, are quite low ($\varepsilon' \leq 0.1$) and display greater variability within each band, diverging significantly in the lower frequency bands (S, G). The dielectric losses of Teflon are reported to be low at ambient conditions ($\sim 10^{-4}$) [54, 55, 57] and significantly lower at cryogenic temperatures ($\sim 10^{-6}$) [58]. However, measurement accuracy of low loss

materials is greatly impacted by the measurement technique. Resonant cavity techniques are reported to have increased accuracy with low loss materials when compared with waveguides [57].

Although the PNA instrument resolution is $\sim 10^{-3}$ and S_{21} magnitude uncertainty is ~ 0.1 dB, the accuracy in the PNA measurement software is $1 - 2\,\%$ [51]. This results in the error for loss measurements being dominated by S_{21} uncertainty. Measured results displaying $\varepsilon'' < 0$ are the result of model inversion calculation error and are indicative of material losses outside the resolution (10^{-3}) of the PNA processing method (this only applies to ε''). Therefore, dielectric loss measurements of Teflon are not considered accurate due to precision limitations of the waveguide measurement technique. Overall, ε' results are in good agreement and verify the invariance of the real part of the complex permittivity of Teflon at low temperatures. Furthermore, these results confirm the feasibility of performing low temperature measurements using waveguides, albeit with limitations when measuring the dielectric loss of low loss materials.

To demonstrate the need for calibrations performed under cold conditions, Teflon was measured with X-band waveguides using a low temperature calibration and a room temperature calibration. Results of these measurements are plotted in Figure 4.10. Low temperature measurements (blue and red curves) are plotted with room temperature measurements (black curve). Consequences of measurement plane mis-alignment can be seen as the red curve diverges from the other curves for both the real and imaginary part of the complex permittivity. Scattering parameters for these data were processed with the PNA instrumentation software (85071: Materials Measurement Software) using a 'Reflection/Transmission Nicolson-Ross Model'.

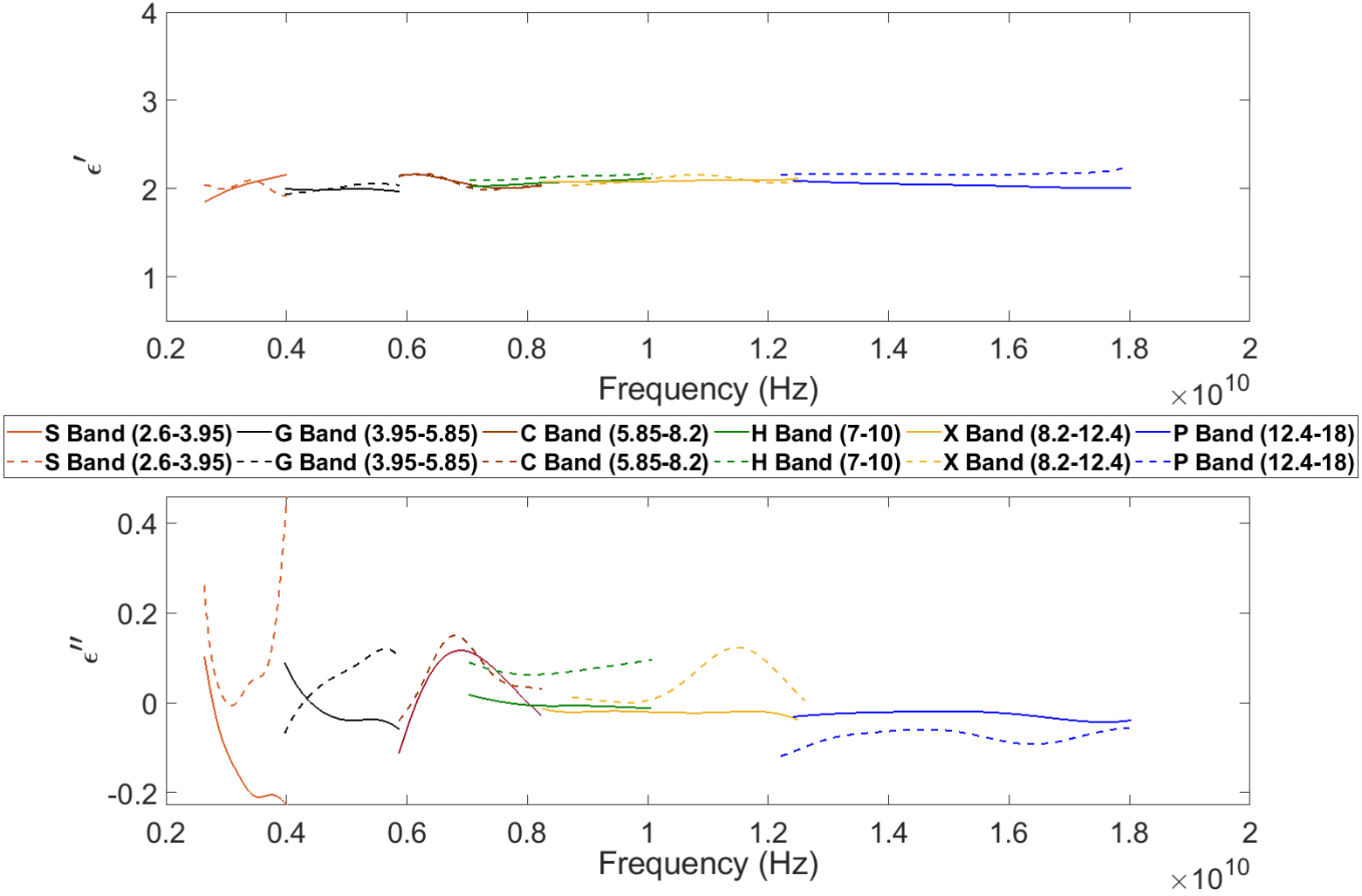

Figure 4.9: Complex permittivity results of Teflon at ambient (solid curves) and low temperature (dashed curves) for all microwave bands used in this research (2.6 – 18 GHz).

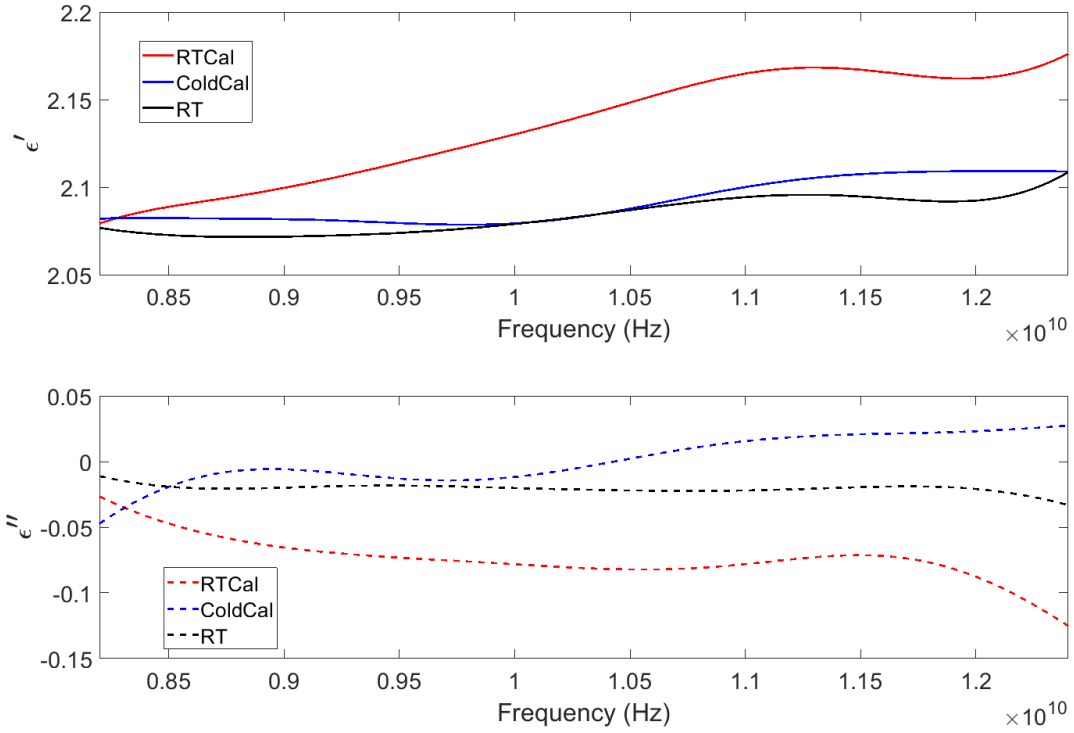

Figure 4.10: Calibration comparison of Teflon at low temperature (X-band). Red and blue curves display complex permittivity of low temperature measurements with room temperature (RTCal) and low temperature calibrations (ColdCal), respectively. Black curves display room temperature (RT) data.

4.3 Processing Scattering Parameters with Genetic Algorithm

Each network analyzer used in this study processed scattering parameters with proprietary models developed by Agilent. These models are not published nor explicitly defined in the software documentation. As discussed in Chapter 2, a genetic algorithm can be generated to process scattering parameters using cascaded networks. In order to have direct control over the processing of scattering parameters a genetic algorithm (GA) was created to include a cascaded network as discussed in Section 2.4. Figure 4.11 displays the proprietary transmission model of the 8364C-PNA ('Transmission Epsilon Fast Model') and the S_{21} GA for low

temperature measurements of Teflon in X-band. As shown, the GA curves match closely to the curves from the PNA with maximum variations of ∼5% at the higher frequency end of the operating range. These variations are the result of the different inversion techniques used to process the scattering parameters.

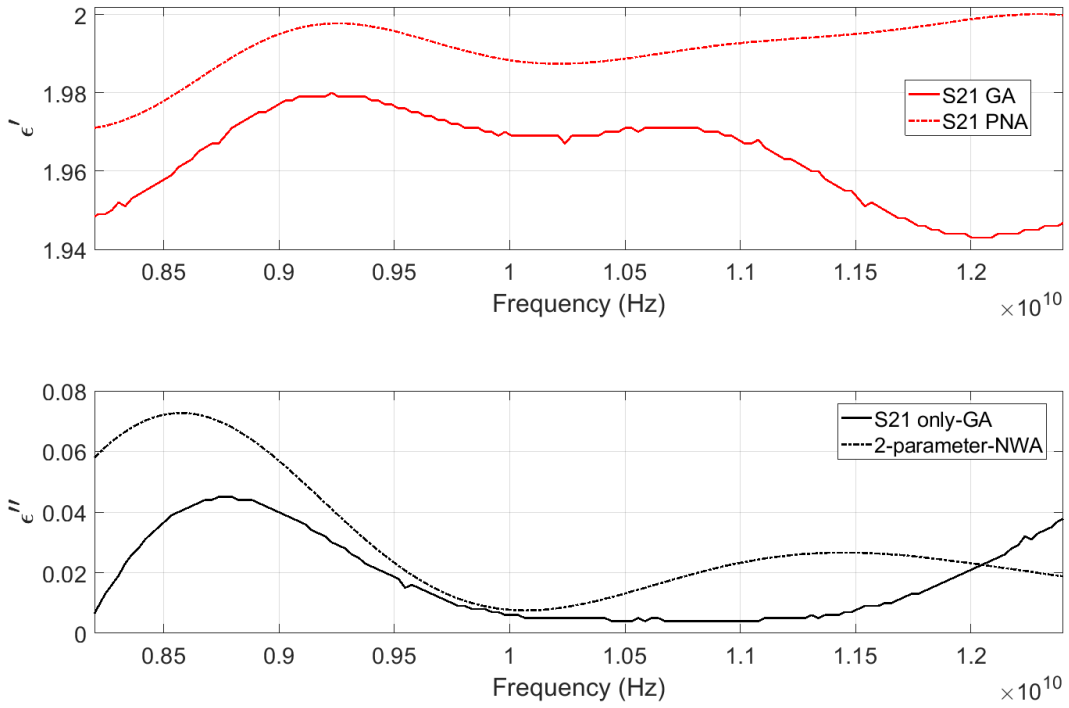

Figure 4.11: GA comparison with PNA model for low temperature Teflon. Results display maximum deviations of ∼5%.

4.4 Summary of Findings

Exploring water extraction using dielectric heating requires characterization of the soil medium with microwave radiation to assess dielectric losses. This study sought to analyze methods of measuring dielectric losses with commonly used techniques (coaxial line and waveguide) in soils at temperatures similar to the near-surface of Mars. In determining a suitable method,

consideration was given to measurement repeatability, effects of low temperature, and integration with the MESF. The following conclusions have been made based on this study:

1) Although dielectric probe results cover a much larger range, being limited to reflection scattering parameters restricts the repeatability of results because this sampling technique is very sensitive to density variations occurring at the probe/sample interface. Since these variations are difficult to control, the dielectric probe is considered unsuitable for acquiring repeatable analysis of the complex permittivity. Moreover, measurements with waveguides exhibit lower deviations among repeated measurements than those observed with coaxial refection techniques. Coaxial transmission methods were not investigated in this study because this method would have been very difficult to integrate with the simulation facility. Thus, soil studies included in this dissertation will be performed with waveguides.

2) It has been demonstrated that mis-alignment of the measurement calibration plane will distort permittivity results. Thus, in order to minimize misalignment distortion, low temperature measurements require low temperature calibrations.

3) Analysis of soil samples is best achieved using S_{21} (transmission) parameters because they exhibit fewer deviations than S_{11} (reflection) parameters. Processing scattering parameters with a genetic algorithm provides reasonable permittivity results and is consistent with results generated by the proprietary software of the PNA. Therefore, a genetic algorithm will be used to process S_{21} scattering parameter results for future soil studies.

4) The accuracy of dielectric loss measurements of Teflon with the waveguide method is limited for low loss materials. Fortunately, losses in simulant soils are observed to be an order of magnitude ($\varepsilon'' \sim 10^{-1}$) higher than in Teflon. The limitations of the waveguide method in regard to measuring losses will be further discussed in Chapter 5.

Chapter 5
SOIL CHARACTERIZATION STUDY

In order to determine the efficacy of dielectric heating, an understanding of the interaction between the subsurface environment and microwave radiation is needed. The subsurface environment or soil matrix, specifically the subsurface environment that would be dielectrically heated, is comprised of soil grains and void space components. When simulating the subsurface of Mars, these components can include perchlorate salts and mixtures of the vapor, solid, and transitional phases of water (H_2O). These components individually contribute to dielectric losses.

Dielectric losses for soils at temperatures consistent with the subsurface of Mars are mostly unknown. The loss mechanisms present at these conditions can directly impact heating capabilities *in-situ* and are critical for dielectric heating applications. Therefore, a soil characterization study was performed to analyze environmental factors, e.g., pressure, temperature, soil composition (particularly water content), to determine how these factors influence dielectric losses. Studies were performed with Mars simulant soils in the Mars Environmental Simulation Facility (MESF) described in Chapter 3. Furthermore, this chapter contains a comprehensive discussion of the loss mechanisms introduced in Chapter 2 and their relevance to the experimental work performed on simulant soils.

5.1 Loss Mechanisms

As discussed in Chapter 1, water resources on Mars are limited to surface and subsurface ice and atmospheric water vapor. *In-situ* losses in the subsurface of Mars can be assessed by simulating the low temperature, low pressure, CO_2-rich atmosphere of the near-surface of Mars. Additionally, when considering possible loss mechanisms in the subsurface that

would contribute to dielectric heating in the frequency range of this research (2.6 – 18 GHz), dipolar relaxations of bound (adsorbed) water are expected to dominate at ambient conditions (Figure 2.1). In contrast, losses due to conductivity and ice relaxation are expected to be several orders of magnitude lower. However, it should be noted that loss mechanisms are temperature-dependent and shift to lower frequencies with decreasing temperature [20]. Thus, there could be a considerable reduction in losses for soil materials at −80°C. To predict the overall dielectric response of icy soils, each soil component (i.e., perchlorate salts, water ice, soil grains) and its potential loss contributions are discussed.

Under the influence of an alternating electric field, water molecules (dipoles) attempt to orient themselves as the electromagnetic field changes rapidly. The rate at which this occurs is dependent on temperature and can be described by the relaxation time, τ

$$\frac{1}{\tau} = Ce^{-\frac{A}{RT}} \tag{5.1}$$

where A is the activation energy, R is the universal gas constant, T is the absolute temperature, and C is a constant [60]. Furthermore, the influence of τ on dielectric loss for materials containing polar molecules can be seen in the Debye equation:

$$\varepsilon'' = \frac{(\varepsilon_0 - \varepsilon_\infty)\omega\tau}{1 + (\omega\tau)^2} \tag{5.2}$$

where ε_0 is the static permittivity (i.e., at $\omega = 0$), ε_∞ is the high frequency (optical) limit of the permittivity, and ε'' is maximized when $\omega\tau = 1$ [60, 61]. Examination of these relations shows the temperature dependence of dielectric losses, i.e., as temperature decreases, maximum losses shift to lower frequencies [20, 60].

Water ice, as submitted by others, has dielectric loss values as low as $\varepsilon''\approx 10^{-4}$ (−80°C, 5 GHz) but peaking at $\varepsilon'' \approx 40$ in the kilohertz region at 0°C [20, 62, 63] where conductivity and ice relaxation loss mechanisms dominate. Although salts and other impurities can increase losses by a factor of 10 (0°C, 5 GHz), losses due to ice relaxation are still very low ($\varepsilon''\sim 10^{-3}$) [62]. However, similar to water ice, saline ice exhibits maximum losses at low frequencies [64]. Figure 5.1 displays models and experimental data for the complex index of

refraction of ice (a proxy for dielectric losses where $\varepsilon'' = 2n'n''$ and the complex refractive index, $n = n' - n''j$ [63]) where losses are shown to monotonically increase with increasing wavelength (decreasing frequency) in the microwave region (300 MHz – 300 GHz), with maximum losses occurring at lower frequencies. It is clear that dielectric losses peak at very long wavelengths but approach a local minimum just outside the microwave range (∼430 GHz). Although data displayed in Figure 5.1 are limited to −20°C, presumably maxima at lower temperatures would continue to shift to lower frequencies. It should be noted that losses derived from Figure 5.1 represent the effective, or total, loss from all active loss mechanisms (Eq. 2.3). Thus, the magnitude of the dominant mechanism would mask contributions from other mechanisms.

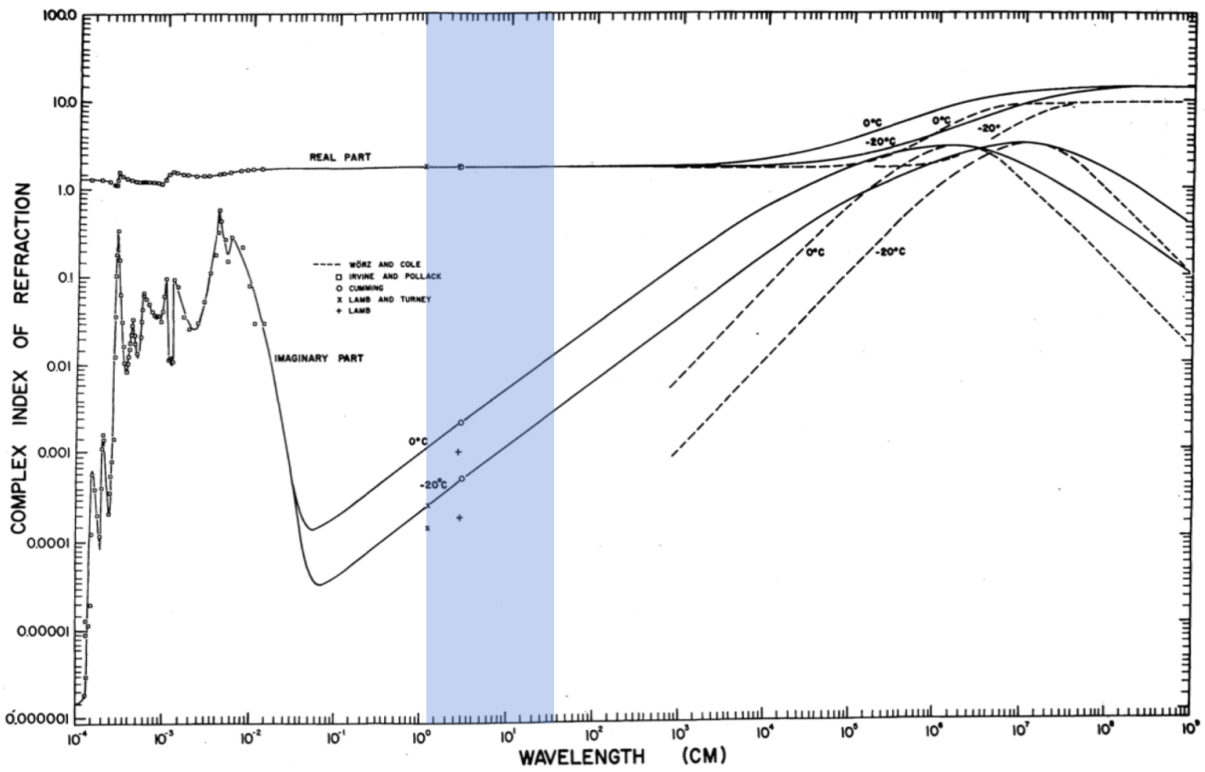

Figure 5.1: Analytical model of the complex index of refraction of ice [20]. Curves for 0°C and −20°C are displayed as dashed (Wörz-Cole model) and solid (analytical model). The shaded region represents the microwave wavelength range of this dissertation.

Saline solutions in the pore space of soils have been demonstrated to enhance dielectric losses due to ionic conductivity in the 1 – 50 MHz range [65]. This loss mechanism is frequency-dependent, decreasing with increasing frequency. Campbell, 1990 also remarks on an observed decrease in losses with decreasing temperature. In addition, very low losses were observed in precipitated salt inclusions (i.e., low water content). The reasoning provided for this observation is that the loss mechanism relies on the connectivity of dissolved salts throughout the sampling medium. Once the mobility of the salts becomes restricted, the effectiveness of the loss mechanism drops rapidly. Moreover, dielectric losses in moist soils mixed with sodium chloride (NaCl), magnesium sulfate ($MgSO_4$), and calcium sulfate ($CaSO_4$) have been observed to yield higher losses than soils with equal salt concentrations but lower water content [66]. Moreover, increasing the concentration of these salts produced a variety of effects on losses, particularly for hydrate-forming salts, e.g., $MgSO_4$ and $CaSO_4$ (Fig 5.2). Lastly, polycrystalline aluminum perchlorate has also been shown to exhibit decreasing losses with decreasing temperature [67]. Thus, although documented observations of dielectric loss in saline soil environments were mostly performed with chlorides and sulfates, the observed dielectric loss behavior in sulfates could also occur in perchlorates, which are also hydrate-forming salts and likely exist as hydrates in the subsurface of Mars [68].

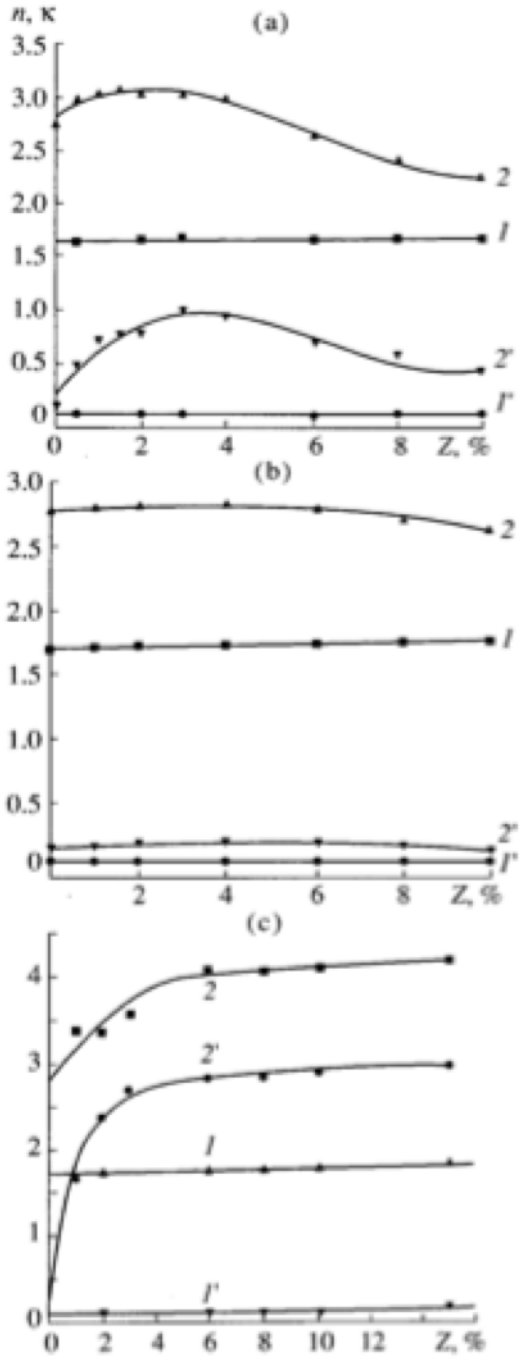

Figure 5.2: Complex index of refraction of moist sand as a function of weight percent (Z) of (a) $MgSO_4$, (b) $CaSO_4$, and (c) NaCl salts at ambient conditions. Curves labeled 1 and $1'$ (ε' and ε'', respectively) are for low water content soils ($0.005\,cm^3$ water/cm^3 soil) and curves labeled 2 and $2'$ (ε' and ε'', respectively) are for higher water content soils (0.15 – $0.17\,cm^3$ water/cm^3 soil). Dielectric losses in hydrate forming salts ($MgSO_4$ and $CaSO_4$) appear more sensitive to increasing salt content than non-hydrate forming salts (i.e., NaCl) [66].

At ambient conditions (∼20°C), soils are heterogeneous mixtures of minerals (including hydrated minerals), air, and various phases of water (liquid, adsorbed). As described in earlier sections, different phases of water present a variety of loss mechanisms throughout the radio and microwave frequency range [23]. Losses attributed to dry soils are very low and not expected to be attributed to any mechanisms associated with water [60, 65]; however, certain minerals have higher losses in the 1.0 – 22 GHz range at ambient, humid (50 – 65 % relative humidity) conditions [69]. Furthermore, losses associated with wet soils are significantly higher, increasing as a function of increasing water content [60, 63]. On the other hand, at low temperatures (≤ 0°C), soils are heterogenous mixtures of minerals, air, ice, and unfrozen water. Thermodynamic and statistical arguments have been presented to explain the existence of unfrozen water or 'thin films' of liquid-like water on the surface of ice [70, 71]. The thickness of these thin films is temperature-dependent, can extend up to tens of angstroms [70, 71], and has been observed down to −79°C [72]. Although there is considerable experimental evidence to support thin films of liquid water on the surface of ice, the precise nature of these films is still a topic of great interest [73]. Furthermore, this unfrozen water has been observed to enhance dielectric losses at ∼10 GHz in sodium-montmorillonite clays at temperatures as low as −47°C due to water relaxations of adsorbed water between the montmorillonite mineral layers [72]. This effect may be unique to expandable phyllosilicate minerals (e.g., montmorillonites), but water adsorption on mineral grains is common for a variety of mineral surfaces [74]. Mironov et al., 2010 further developed this concept of unfrozen water by assigning a multilayer interface between soil grain surfaces and ice for the development of a dielectric model that would predict dielectric losses in soils under a variety of conditions. This multilayer approach identifies three adsorbed water types: bound water, transient bound water (transient water), and moistened ice water (ice water) (Figure 5.3). Bound water is closest to the soil grain surface, ice water closest to the ice surface, and transient bound water exists in-between and exhibits mobility features sensitive to charge conductivity [72, 75, 76]. At −15°C (10 GHz), losses associated with these waters, as observed in Artic soils, are highest for transient water, followed by bound water and ice water, as shown

in Figure 5.4. Interestingly, transient water losses at $-15°C$ are higher than bound water losses at ambient conditions (i.e, 25°C). Additionally, Mironov et al., 2010 ascertained that although transient water behaves similarly to liquid water, they should not be considered the same. Moreover, others report that, in general, spectral features of adsorbed water, albeit similar to one another, are not entirely comparable to liquid water or ice [74].

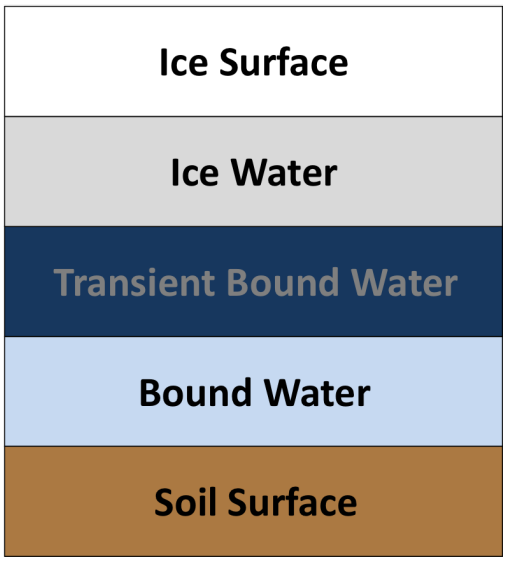

Figure 5.3: Adsorbed water layered between a soil surface and an ice surface in frozen soil as described in Mironov et al., 2010.

The combined works of Mironov et al., 2010 and Hoekstra and Doyle, 1971 present a more nuanced perspective on water adsorption at cold conditions. It is evident that unfrozen water observed in soils can be characterized by adsorbing surfaces. A layered adsorption structure coupled with enhanced losses at cold conditions strongly suggest that the dominant loss mechanism in icy soils is very different from cold, dry soils. The mobility of transient bound water in icy soils could activate both the free water relaxation and ionic conductivity loss mechanisms (for soils containing ionic molecules) in addition to bound water relaxations. The combined effect of these loss mechanisms would explain enhanced losses occurring in icy soils. However, at 10 GHz (ambient conditions) only the free water and bound water

mechanisms are active. Thus, it is unclear how bound water and ice loss mechanisms respond to bound water on cold, dry soils. It is also unclear how bound water loss mechanisms vary with adsorbed water content at cold conditions. There is little discussion in the literature regarding the influence of bound water on the effective dielectric loss in soils as a function of water content or humidity. Although Mars is expected to have 4.0 – 8.0 % water equivalent hydrogen in the subsurface (equatorial regions) (Figure 1.1), losses reported for icy soils were at higher water content [72, 75]. These higher losses, if used to predict dielectric heating, could overestimate heating effects expected at the near-surface of Mars.

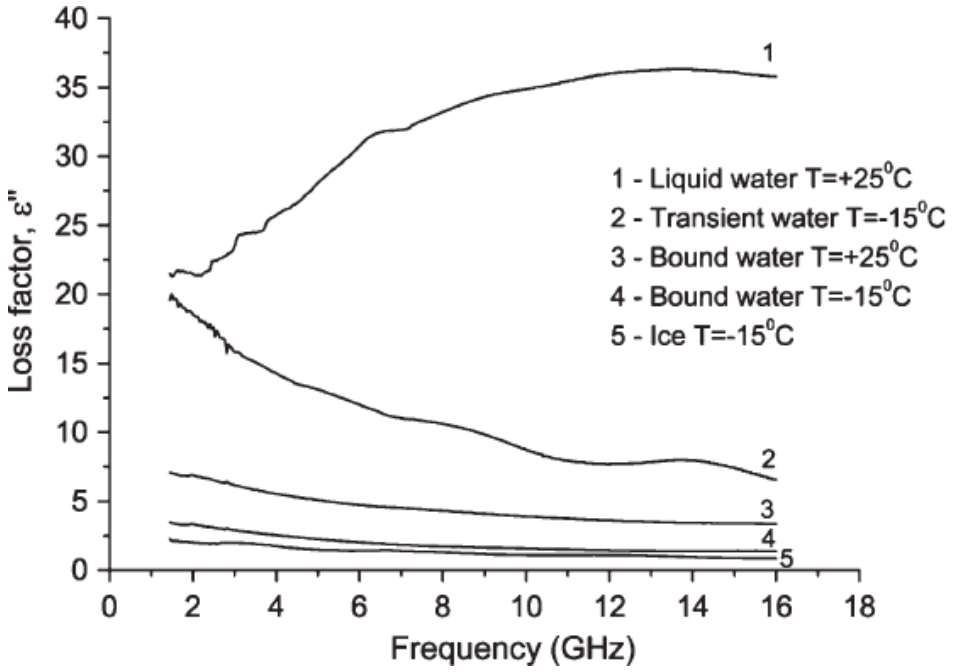

Figure 5.4: Dielectric losses in adsorbed water layers at ambient (25°C) and cold conditions (−15°C) [75].

5.2 Study Materials and Components

The work described in this dissertation sought to analyze dielectric heating at cold, low pressure environments so it was necessary to install the waveguide assembly in a vacuum

pressure vessel as described in Chapter 3. The Mars Environmental Simulation Facility (MESF) was used for all soil studies.

Analysis of the complex permittivity of a simulated Mars subsurface was performed in the 2.6 – 18 GHz frequency range. Each waveguide required a customized sample cell as shown in Figure 3.9. These sample cells were used for all soil studies. Prior to assembly, sample cells were vacuumed (to remove dust from screens, flow tubing, etc.) and cleaned with isopropyl alcohol. The foam windows were also cleaned of any debris. When preparing soil samples, a foam window was installed on one side of the sample cell, then the sample cell cavity was filled with soil and covered with the other foam window. Sample cells were then mounted to the mating waveguides with slip-fit alignment pins (when required) and bolted in place. The waveguides were then connected (via N type coax-to-waveguide adaptors) to the coaxial cables in the pressure vessel as described in Chapter 3.

In order to establish uniform flow conditions within the sample cell, the pressure vessel was evacuated via the sample cell. One side of the sample cell was connected to the aluminum flexible tubing, which led to the facility vacuum pump, while the other side of the sample cell was open to the interior of the pressure vessel (Figure 3.6). Flexible tubing was chosen due to its adaptability to the varying sizes of waveguides that were mounted inside the pressure vessel.

5.3 Measurement Methods

Measurements of Mars simulant soils were performed at room temperature (ambient) and low temperature (~ -80°C) while varying pressure conditions and background gases. Once samples were loaded into the pressure vessel, measurements were taken at ∼20°C and standard pressure (∼760 torr) (step A), afterwards samples were evacuated. The sequence of measurements listed in Table 5.1 display the pressure/temperature/background gas condition for subsequent measurements. After initial evacuation (step B), the pressure vessel was backfilled with CO_2 (step C), then re-evacuated prior to step D. Step D was accomplished by slowly backfilling the pressure vessel with ambient air prior to cooling. Afterwards, the

pressure vessel was evacuated again to achieve a low temperature, vacuum condition (step E). Steps A-D were performed across all waveguide bands; however, low temperature vacuum measurements (step E) were only performed with X-band waveguides (8.2 – 12.4 GHz). The 'condition' column listed in Table 5.1 refers to the impact of evacuation and temperature on the water content of the soil samples and is discussed further in Sections 5.4.2 and 5.4.3. All simulants at both grain size categories (Figure 3.10) were measured throughout the sequence across the 2.6 – 18 GHz range with the exception of the lower frequency bands (i.e., G, S) due to equipment failure. All measurements were performed under static flow conditions (i.e., no-flow conditions) except for vacuum measurements. During vacuum conditions (refer to Table 5.1), the pressure vessel was continuously evacuated. In addition to soil measurements, dielectric losses were obtained for each background gas listed in Table 5.1 with the exception of step E.

Table 5.1: Characterization study measurement sequence

	Temperature (°C)	Background gas	Pressure (Torr)	Condition
A	20 ±	Air	760 ±	ambient
B	20 ±	Vacuum	.050 ±	ambient-drying
C	20 ±	CO_2	760 ±	--
D	-80 ±	Air	760 ±	cold
E*	-80 ±	Vacuum	.050 ±	cold-drying
*Only performed on Xband				

Further dielectric loss analyses were performed with icy soils by mixing simulants (JSC-RN and MMS) with deionized water at 8.0 and 22.0 wt.%, where,

$$wt.\% = \frac{m_{H_2O}}{m_{H_2O} + m_{simulant}}. \tag{5.3}$$

Simulant mixtures were installed in X-band sample holders and were contained with foam windows (when needed). After soils were installed, water was pipetted directly onto the soil sample. Simulant, mass, and water volume data for each mixture are listed in Table 5.2.

Table 5.2: Soil mixtures for cold permittivity experiments

Simulant	Mass [g]	Volume, H_2O [µL]
MMS	1.16	101
		327
MMS•$NaClO_4$ (1.2 wt.%)	1.51	131
	1.35	381
JSC-RN	1.77	153
		500

Afterward, the sample holder was installed in the waveguide assembly. A similar procedure was performed to measure sodium perchlorate-water mixtures and ice (deionized water and deionized water-perchlorate mixtures). Mixtures were only measured at cold conditions; thus, for these measurements (including ice and sodium perchlorate measurements) the waveguide assembly was mounted directly in the freezer in lieu of the pressure vessel.

5.4 Results and Discussion

Results presented in this section contain dielectric loss results at ambient conditions (17.7 – 28.0 °C) and cold conditions (-77.6 to −90.8 °C) as a function of background gas, water content, temperature, grain size, and salinity.

5.4.1 Background Gas

Dielectric losses of the background gas across X-band are plotted in Figure 5.5. It was observed that losses of background gases were very low and do not appear to vary with composition or pressure; although, there does appear to be a temperature dependence, which can be seen for cold air (Fig. 5.5). However, since the amplitude change between ambient and cold measurements (~ 0.01) is within the measurement uncertainty it is doubtful that observations reflect loss variations due to the background gas.

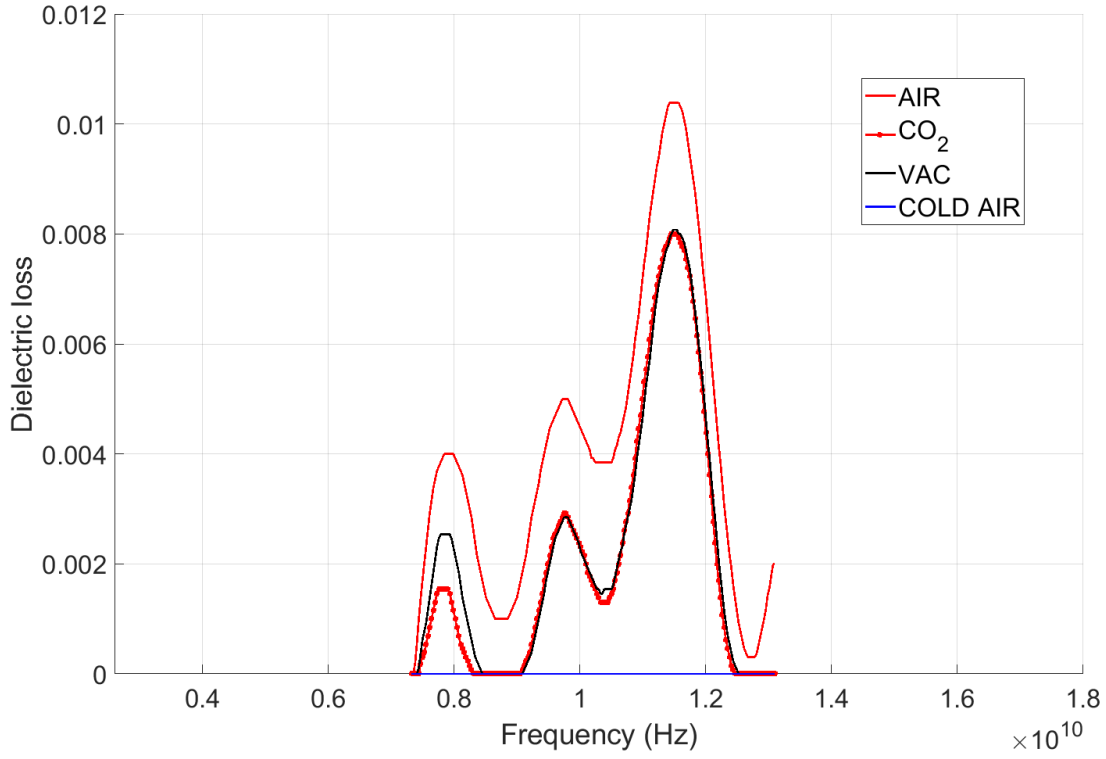

Figure 5.5: Dielectric loss of Air (ambient and −80°C), CO_2, and vacuum across the X-band frequency range.

Of the limited number of publications reporting on the permittivity of gases, few directly address dielectric losses. Of those, dielectric losses in ambient air at standard pressure have been observed to peak at 60 GHz [77]; however, losses at low temperature and low pressure do not appear to have been previously reported. Interestingly, losses of all background gases appear to increase with frequency within P-band (12.0 – 18 GHz) as shown in Figure 5.6. However, losses were not observed to vary in soils as a function of background gas.

5.4.2 Water Content: Dry Soils

In general, dielectric losses are greatly impacted by water content; however, losses vary with phase/configuration and frequency. Loss mechanisms expected to occur in dry soils at

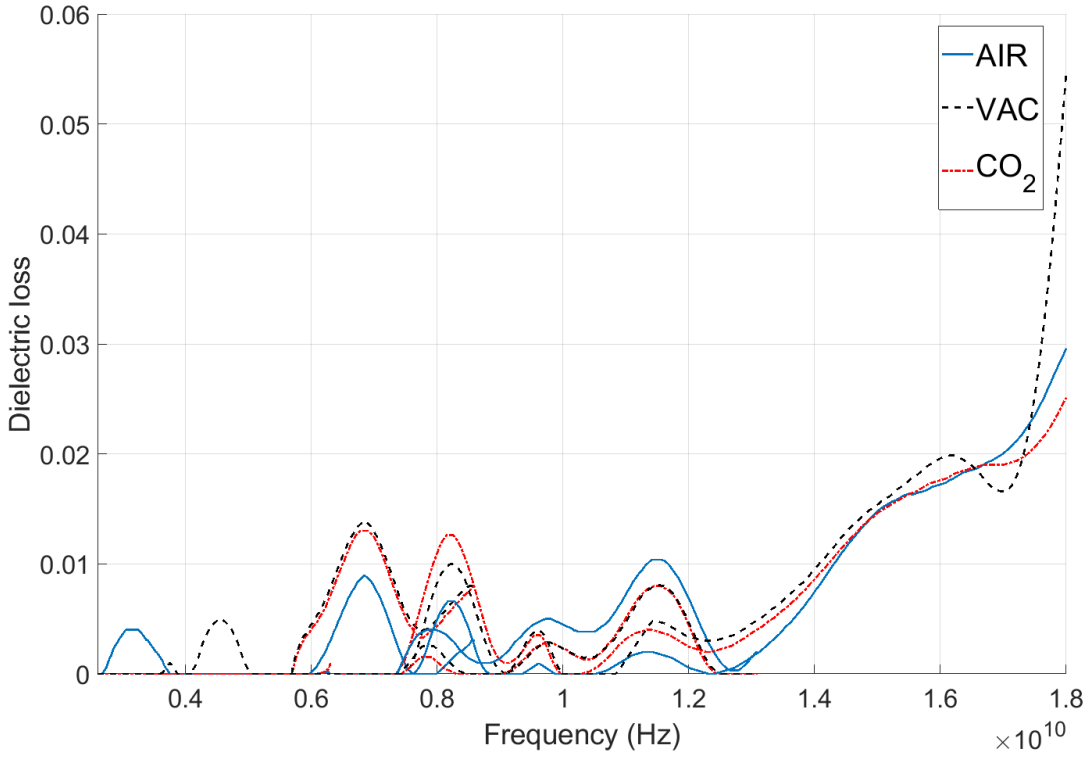

Figure 5.6: Dielectric loss of air, vacuum, and CO_2, at ambient conditions from 2.6 – 18 GHz.

ambient conditions (relative humidity $\leq 43\%$) are limited to bound water. Figure 5.7 displays losses at ambient conditions (red curves) for all waveguide bands, within all soil simulants. It should be noted that no simulants had any bulk liquid water but had varying moisture levels due to adsorbed water. Relative humidity can be used as a proxy for adsorbed water layer thickness—higher humidity indicates thicker adsorbed water layers [78]. The relative humidity within samples was observed to vary between 0.0003 – 43 % and 5.7% to saturation conditions for ambient and cold samples, respectively. Assuming losses in Figure 5.7 reflect a variable amount of adsorbed water, lower losses occurring at ambient-drying conditions (black curves) should reflect reduced water content. Although evident within all bands, this reduction effect is most noticeable for X-band ($0.82 - 1.24 \times 10^{10}$ Hz). Losses observed on JSC-RN (ambient-drying condition) were extremely low with a considerable amount of noise

and are most likely indicative of losses below the detection limit of the NWA instrument. Furthermore, cold-drying conditions also reflect losses below the detection limit and are most likely a consequence of the reduced temperature. Figure 5.8 displays cold and cold-drying conditions of all simulants within X-band. Cold-drying conditions were not performed on other bands. Aside from errant features, which are difficult to interpret and are likely instrumentation or inversion artifacts, losses are minimal.

Analysis of these results, considering the multi-layer adsorbed water profile (Fig. 5.3), suggests that losses in cold, dry soils (limited to bound water only, without ice) would experience a similar drying effect as ambient soils (Figure 5.7) when subjected to drying conditions. However, a reduction in losses at cold-drying conditions was not observed, nor was there an observable level of losses at cold conditions. Water vapor density at saturation conditions varies by three orders of magnitude between ambient ($10^{-3}\frac{kg}{m^3}$) and cold conditions ($10^{-6}\frac{kg}{m^3}$) [79]. Reducing the temperature of moderately humid samples could also have a drying effect, inducing water to migrate from the sample cell to the interior of the waveguide assembly. Whether temperature-induced drying is more pronounced than pressure-induced drying (evacuation) is unclear. Therefore, losses could have been reduced due to the lack of water content; however, adsorbed water, reduced to a monolayer could not be removed by drying alone, a significant energy input would be required to rid soils of all adsorbed water [80, 81]. Additionally, if bound, ice, and transient water respond to bound, ice, and free water loss mechanisms, respectively, it would follow that losses in dry, cold soils would be attributed primarily to the bound water loss mechanism in the microwave region. Moreover, these losses should be observable if the measurement technique is precise enough for low loss materials of this magnitude. It is clear that measuring losses at cold conditions in soils absent of bulk water (i.e., ice), is outside the detection limit of the waveguide method.

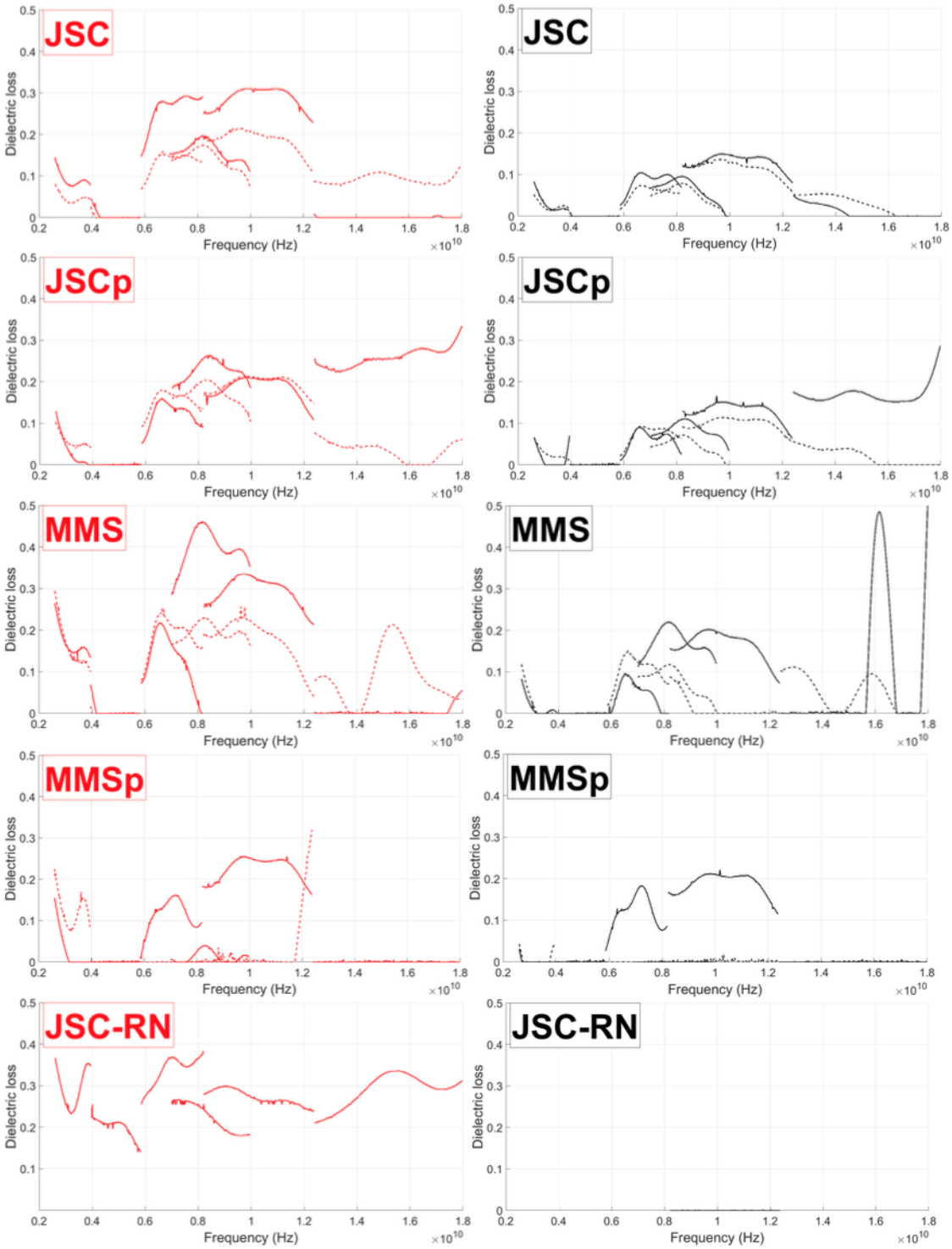

Figure 5.7: Dielectric loss of Mars simulants at ambient (left column) and ambient-drying conditions (right column) across the frequency range of this study, i.e., from left to right S, G, C, H, X, and P bands. Curves are displayed for small grains (solid) and large grains (dashed).

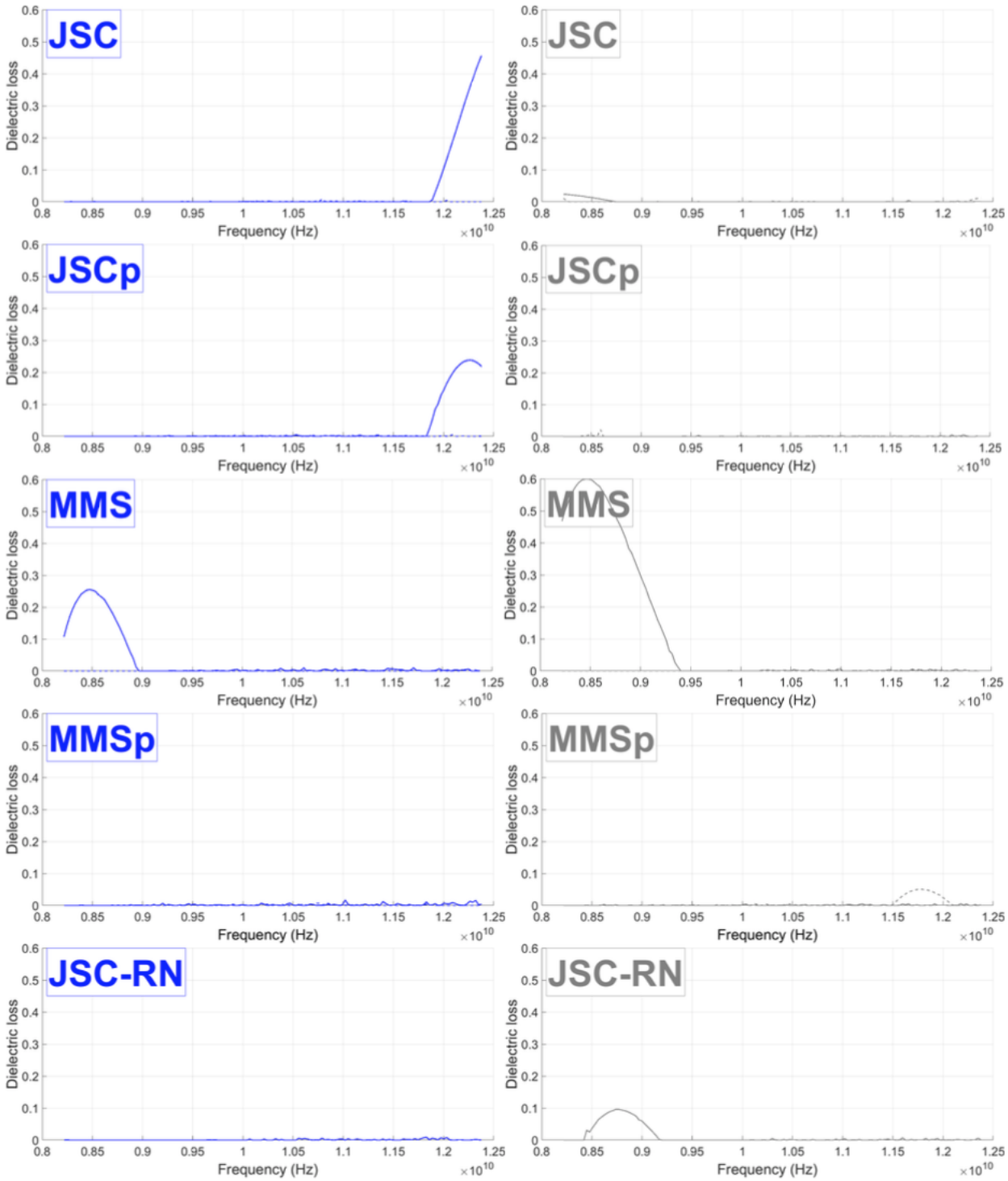

Figure 5.8: Dielectric loss of Mars simulants at cold (left column) and cold-drying conditions (right column) across X-band. Curves are displayed for small grains (solid) and large grains (dashed).

5.4.3 Temperature

Dielectric losses at low temperature of all simulants across all waveguide bands (except S-band) are displayed in Figure 5.9 (blue curves). The reduction in losses evident in these data is due to the configuration of water content and the associated mechanisms (ambient losses from Figure 5.7 are reprinted for comparison in Figure 5.9). At ambient temperature on dry soils, bound water is the dominant loss mechanism; however, at low temperature on dry soils, bound water is still the dominant loss mechanism (although present, losses due to ionic conductivity and ice relaxation are very low). Therefore, although the dominant loss mechanism is constant at ambient and cold conditions, the reduction in losses is likely due to a reduction in the thickness of adsorbed water layers. Losses plotted for C-band (0.6 – 0.8×10^{10} Hz) at cold conditions appear invariant across all simulants and is likely due to a calibration error for that band. Interestingly, losses within H-band for JSCp and JSC-RN are not reduced as much as other bands/simulants at cold conditions. It was observed that losses at cold and cold-drying conditions were outside the detection limit for most simulants in X-band (Figure 5.8).

It is evident that losses decrease as a function of decreasing water content and temperature, which has implications for dielectric heating. However, this behavior was not documented by others [8, 9]. The highest losses observed (at ambient conditions) indicate that losses associated with bound water dominate the effective loss factor. However, when comparing ambient-drying conditions to cold conditions, the pronounced reduction of losses indicates that temperature has a stronger influence on losses. What remains unclear is whether the temperature effect is due to temperature-dependent shifting of the bound water loss mechanism or inactivation of the bound water loss mechanism (due to drying) at low temperature. Thus, it is difficult to conclude if data presented here infer temperature-dependent shifting of loss mechanisms.

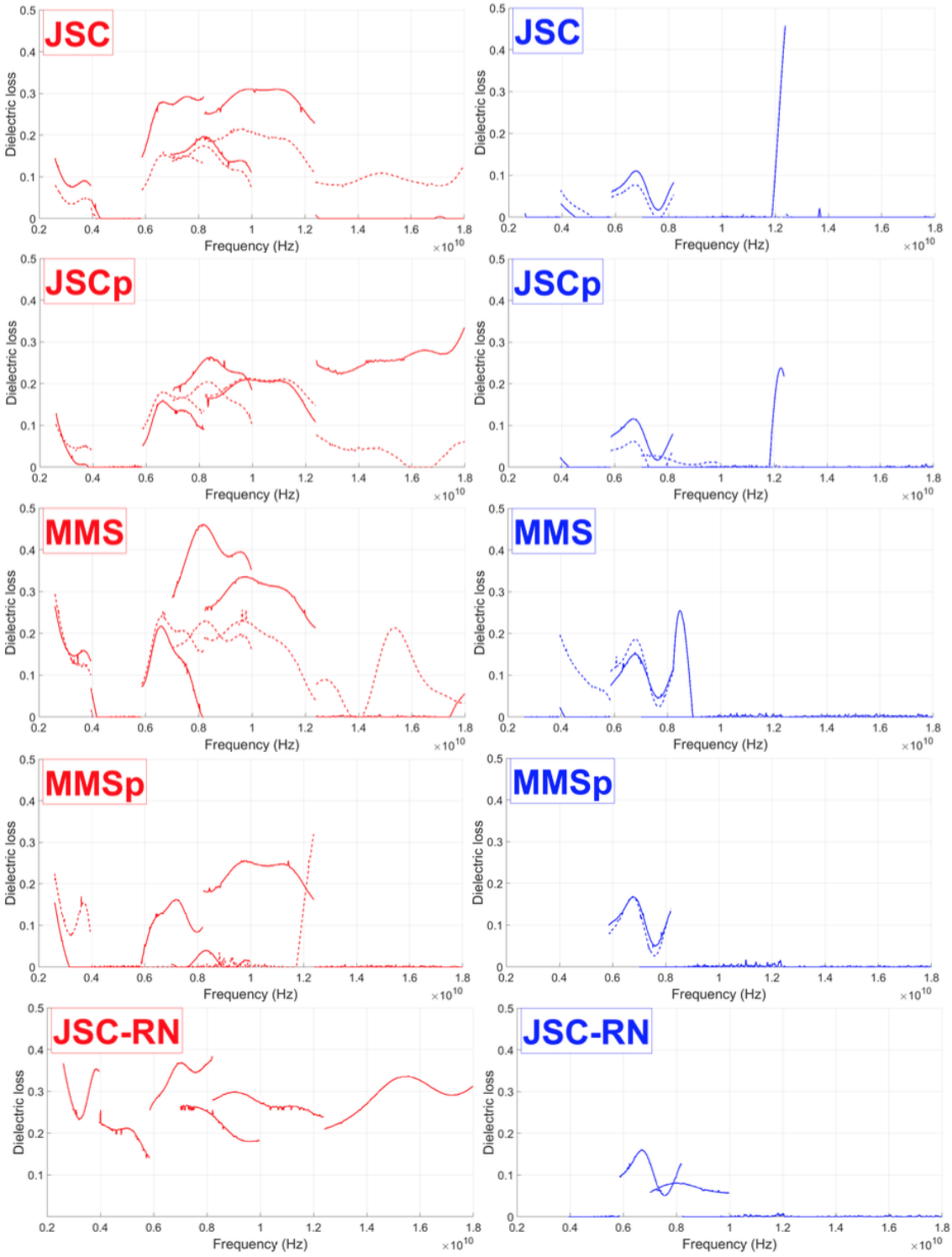

Figure 5.9: Dielectric loss of Mars simulants at ambient (left column) and cold conditions (right column) across the frequency range of this study, i.e., (from left to right) S, G, C, H, X, P. Curves displayed for small grains (solid) and large grains (dashed). Figure 5.7 (left column, ambient conditions) reprinted for comparison.

5.4.4 Grain Size

Adsorption of water to soil grains is enhanced significantly (in terms of surface area for adsorption) by smaller particles. Due to the homogeneity assumptions of the waveguide measurement method, simulants were sieved to two grain size categories—small grains (180 – 246 μm) and large grains (600 – 710 μm, 710 – 850 μm, and 850 – 991 μm). The large grain size category varied for each simulant and was based on the amount of soil needed to perform measurements. Assuming spherical particles and accounting for void spaces, 200μm-diameter soil grains would yield 20% higher surface area than 900μm-diameter particles. Therefore, increased surface area available for water adsorption should have an observable effect on dielectric losses.

Although smaller grain sizes appear to yield slightly higher losses, these variations are only consistent within H-band and X-band on some simulants (i.e., JSC, JSCp, MMS) (Fig 5.7, left column). Another possibility for the observed variations could be unrelated to grain size entirely and simply be an indicator of measurement uncertainty.

5.4.5 Salinity

Dielectric loss measurements (Fig. 5.10) of anhydrous sodium perchlorate within X-band show low losses ($\varepsilon'' < 0.3$) for dry, cold, and icy samples. However, at ambient conditions, dielectric losses of sodium perchlorate-water mixtures increase significantly. Again, it is evident that cold conditions greatly decrease losses due to the configuration of water content. Furthermore, losses in JSCp, MMSp, and JSC-RN (all perchlorate mixtures of JSC and MMS), mixed at 1.5% (JSCp/MMSp) and 1% (JSC-RN) perchlorate, have losses similar to their base material (Fig 5.7, left column), albeit, somewhat reduced in some bands. This implies that mixing dry sodium perchlorate with simulants does not impact losses, which appears consistent with loss measurements of pure sodium perchlorate. Thus, for the samples measured, anhydrous perchlorate salts, in dry soil simulants, do not appear to effect dielectric losses significantly.

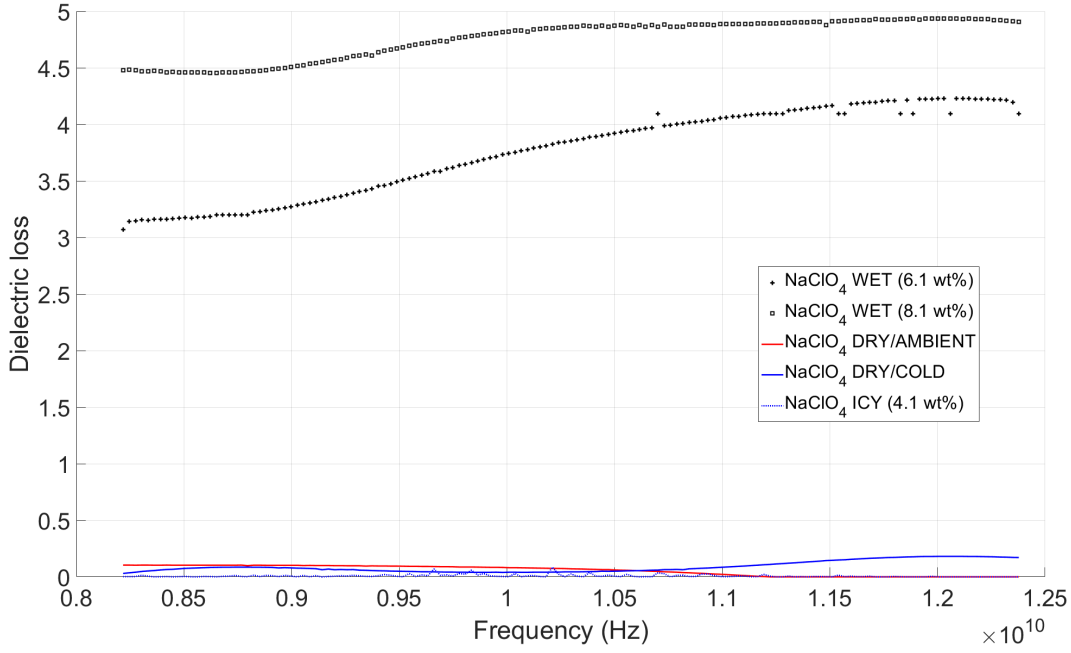

Figure 5.10: Dielectric loss of anhydrous $NaClO_4$ at dry, cold, wet and icy conditions across the X-band frequency range. Icy $NaClO_4$ was prepared at 4.1 wt.% liquid water then cooled. Cold and icy samples were measured at -84.5°C and -81°C, respectively. Wet and dry samples were measured at ambient conditions (19.0 – 26.0 °C).

5.4.6 Water Content: Icy Soils

As discussed in earlier sections, dielectric losses in the microwave region are sensitive to water content. Uniquely for dry soils, losses are likely derived from bound water loss mechanisms at ambient conditions; however, these losses are drastically reduced at cold conditions. Losses derived from ice are minimal in the microwave region but peak at radio frequencies (1 – 10 kHz). Additionally, perchlorate salts in dry soils were not observed to enhance losses. Thus, soils with or without perchlorate are not expected to exhibit increased losses when ices are included in soil mixtures. However, as previously discussed, Hoekstra and Doyle, 1971 observed high losses (i.e., > 0.5) at ∼10.0 GHz on icy sodium-montmorillonite soils at -47°C and 35 wt.% H_2O due to unfrozen water adsorption between mineral grains. It was

of interest to determine if a similar result would be obtained on Mars simulant soils in which phyllosilicates have either not been observed, or occur at < 1 wt.% [38, 82]. Interestingly, both icy JSC-RN and icy MMS·$NaClO_4$ soils at 8.0 and 22.0 wt.% H_2O exhibit similar losses to the results observed by Hoekstra and Doyle, 1971 (Figure 5.11). However, observations of the base material of these simulants (i.e., MMS) do not reflect comparable losses when measured at the same water content. This observation suggests that dielectrically, the soil grain-perchlorate interface in the presence of ice is distinctly different from icy perchlorate, which did not appreciably enhance losses. A potential explanation for this behavior could be that water adsorbing to salt surfaces is dielectrically dissimilar to water adsorbing to soil surfaces *and* equally dissimilar to the transient unfrozen layer that develops between these surfaces [72, 75]. Moreover, salinity enhances losses in wet soils when compared to non-saline wet soils, but this effect decreases with increasing frequency and is most pronounced at low frequency (< 4.0 GHz) [83]. Furthermore, this effect is likely similar within transient liquid-like layers in icy soils.

Deionized water ice and sodium perchlorate ice (1.2 wt.% $NaClO_4$) are included in Figure 5.11 to demonstrate dielectric loss contributions from ice. It should be noted that the magnitude of dielectric loss in Figure 5.11 for ice samples represents an upper limit for losses expected in icy soil samples. This is due to the fact that losses are a function of volume and all samples displayed in Figure 5.11 were of similar volume (i.e., $\sim$1.1 cm^3), with ice occupying a maximum of $\sim$ 36% and 25% of the sample volume for JSC-RN and MMS respectively. It is apparent that enhanced losses in icy soils are not due to dielectric losses in the soil (regardless of perchlorate content) or ice. These observations support the existence of transient liquid layers in icy soils and strongly suggest that enhanced losses are directly related to the liquid-like nature of these layers.

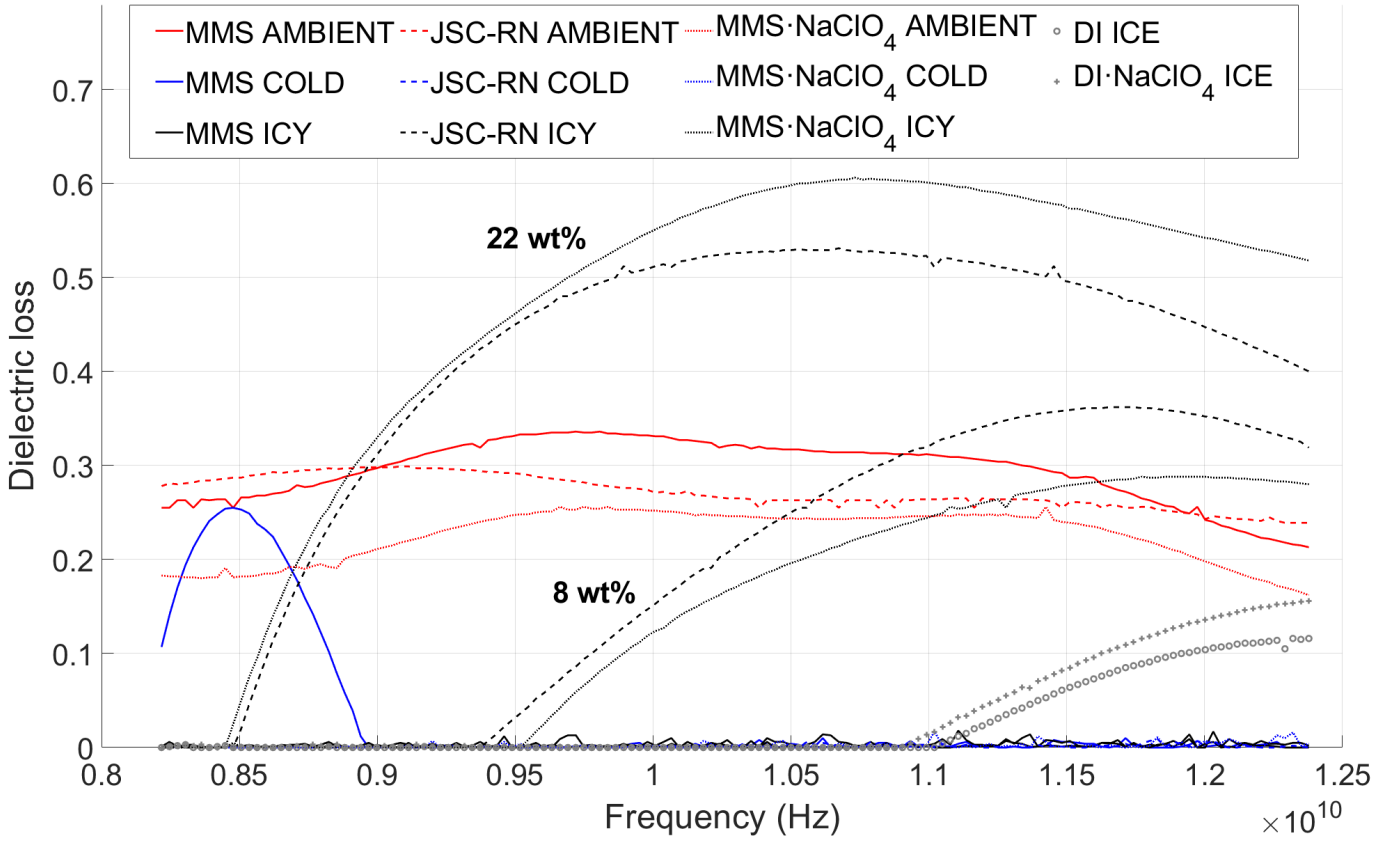

Figure 5.11: Dielectric loss of icy mixtures at 8.0 and 22.0 wt.% compared with JSC-RN, MMS, and MMS·$NaClO_4$ at ambient and cold conditions. Grey curves (lower right) display dielectric losses in pure deionized water ice (DI ice) and sodium perchlorate DI ice (1.2% $NaClO_4$).

Chapter 6
ENERGY COUPLING TO SOILS

Previous chapters have addressed the identification of loss mechanisms in soil components; however, complex permittivity alone does not provide enough information to analyze thermal distributions that arise from microwave energy coupling to soils. Energy exchange occurring between microwave radiation and soils is a complex interaction governed by the heat equation,

$$\rho C_p \frac{\partial T}{\partial t} + \nabla \cdot (-k \nabla T) = Q \tag{6.1}$$

where ρ (density), C_p (specific heat capacity), and k (thermal conductivity) represent thermal properties of the soil and are generally temperature dependent. The term Q is the heat source term and represents energy input (in Joules) as a result of microwave energy coupling. Modeling of soil temperature profiles is beyond the scope of this dissertation. However, such models could be validated with heating experiments similar to those contained in this chapter.

In addition, the variation of loss signatures observed in soil simulants in Chapter 5 gives rise to questions of how thermal effects vary with changing losses. Losses occurring outside the detection limit of the NWA do not necessarily imply that heating does not occur at low-loss conditions. Furthermore, it is unclear how enhanced losses, due to transient adsorbed water at cold conditions, translate to heating. Thus, to supplement permittivity results, a series of low power heating experiments were performed at cold and ambient conditions to experimentally determine temperature profiles in simulant soils.

6.1 Materials and Methods

In order to observe dielectric heating of icy soils, measurements of this coupling effect were performed using a resonator, amplifier, waveguide (X-band), and soil sample holder (Figure 6.1). The tunable resonator (EMF Systems, Inc., P/N: 52747-626048) was operated at

10 GHz and had an output power of 10 dBm (10 mW). A MACOM power amplifier (LWA 6012-2/10859) was downstream of the resonator and increased the power output to approximately 2.6 W. An isolator was installed as a safety feature to prevent reflected radiation from propagating back to the amplifier. A Faraday cage, constructed of cardboard and covered with aluminum, isolated radiation exiting the waveguide from the interior of the freezer. Power transmitting through the waveguide was monitored with a Hewlett Packard 437B power meter via the coupled port. Since the power meter had a 100 mW limit, attenuators were placed in line to reduce power exiting the coupled port. The X-band frequency range was chosen to supplement X-band permittivity results on icy soils (Chapter 5). Aside from the power meter, attenuators, resonator, and amplifier, all components were installed in the facility freezer and subjected to cold conditions (−80°C).

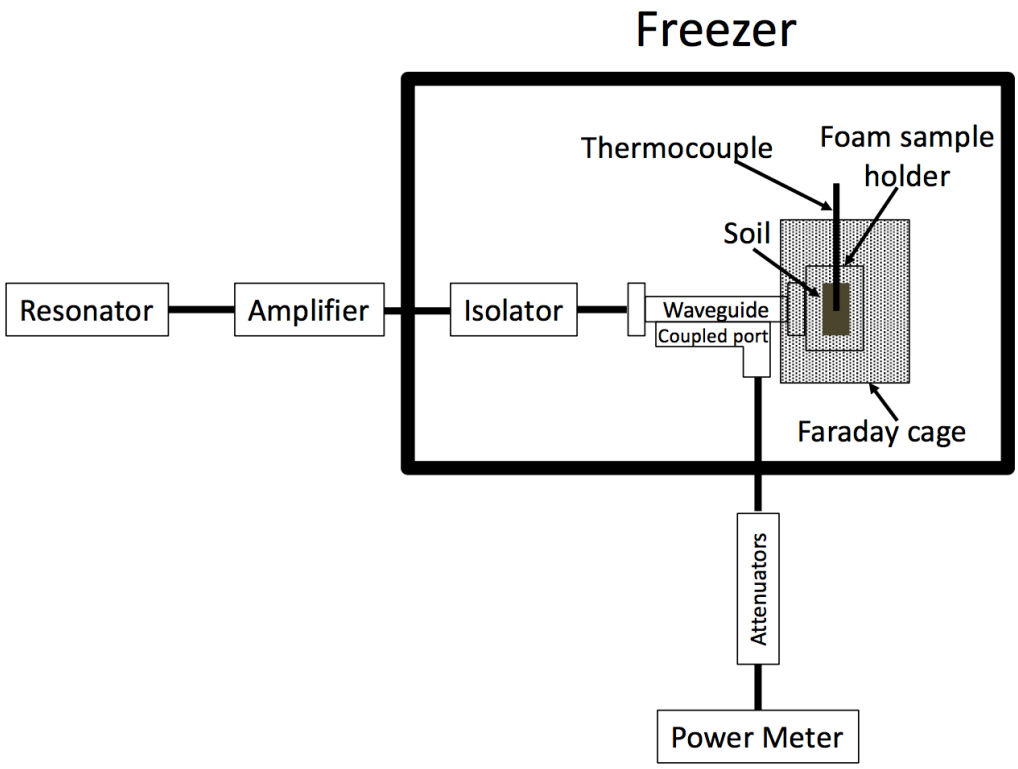

Figure 6.1: Experimental setup for dielectric heating of Mars simulant soils.

The sample holder was constructed of a foam frame (Rmax Thermasheath-3 polyisocyanurate rigid foam) (Fig. 6.2) with foam end pieces (Laird Eccostock, 0.64 cm thick) and enclosed a 11.0 cm^3 soil sample (Fig. 6.3). To measure temperature, a Type E thermocouple probe was installed through the rigid foam and embedded ∼3.0 cm into the soil sample. The thermocouple was positioned such that it was orthogonal to the electric field of the radiation exiting the waveguide. This was done to minimize energy coupling and heating of the probe. Foam end pieces were rated as low loss ($\varepsilon' < .001$) and were not expected to couple to the radiation transmitted through the sample holder. The sample was irradiated via waveguide at ambient (13.2 to 22.6°C) and cold conditions (−79.3 to −82.3°C). The waveguide was in physical contact with the foam sample holder during heating.

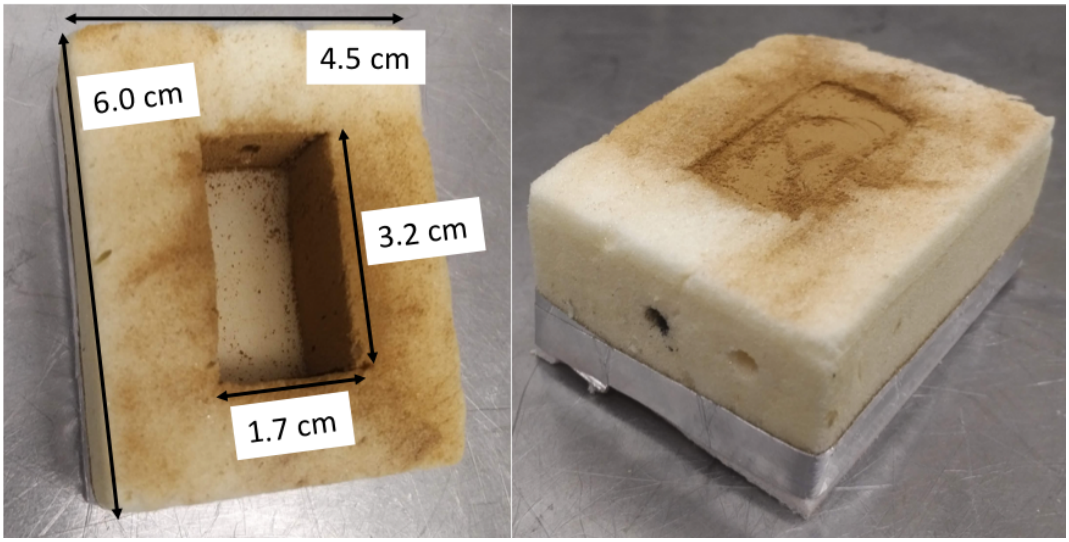

Figure 6.2: Interior of foam sample holder with (right) and without (left) JSC-RN sample. Dimensions of wall thickness and depth are 1.2 and 2.0 cm, respectively.

Output power at the exit aperture was measured with a power meter at ambient and cold conditions and was within 0.1 W for both conditions. A significant power drop was observed from the output of the amplifier to the waveguide aperture. This is a direct result of coupling losses attributed to connections and components (e.g., cables, SMA connections, isolator, etc.) and reduced the output power at the waveguide exit aperture to 1.2 and 1.3 W

at ambient and cold conditions, respectively. Aside from these losses, all power exiting the waveguide is assumed to be directed to the soil sample within the foam sample holder. Given similar power input conditions, observed differences in temperature between ambient and cold conditions are assumed to be a direct result of temperature-dependent energy coupling to the soil as a function of water content.

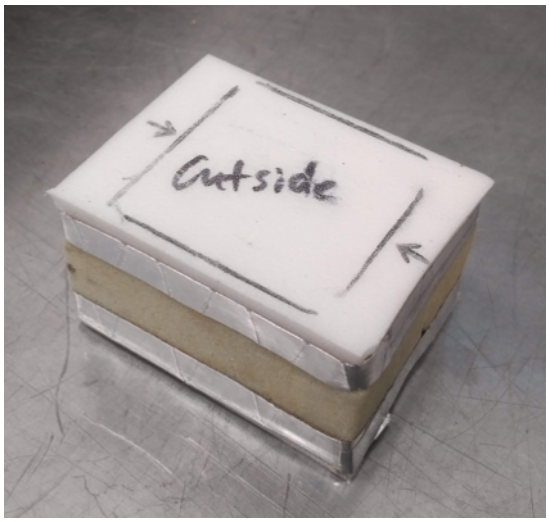

Figure 6.3: Assembled foam sample holder used for energy coupling experiments with simulant soils.

Soil mixtures were comprised of soil simulants, deionized water, and anhydrous sodium perchlorate ($NaClO_4$). In order to present a more realistic simulation of the subsurface of Mars, simulants were not sieved and thus contained a broader distribution of grain sizes than the soils analyzed in Chapter 5. Additionally, mixtures were prepared to match the permittivity mixtures described in Chapter 5 (i.e., 8.0 and 22.0 H_2O wt.%). Soils and deionized water were combined in the foam sample holder (Figure 6.2) by incrementally adding soil layered with pipetted water. The mixtures were prepared this way to distribute the water homogenously throughout the sample prior to freezing. Afterward, the sample holder was sealed with metallic tape (Figure 6.3) and positioned at the exit aperture of the waveguide. All mixtures analyzed are listed in Table 6.1.

Table 6.1: Soil mixtures for dielectric heating measurements

Simulant	Mass [g]	Volume, H_2O [μL]
MMS	24.8	2155
		6991
MMS•$NaClO_4$ (1.2 wt.%)	24.8	6991
	25.3	2200
JSC-RN	17.6	1530
	21	4451

6.2 Results and Discussion

Results from dielectrically heating Mars simulant soils (JSC-RN, MMS) are displayed in Table 6.2. Overall, most icy soils have similar heating rates, but JSC-RN at cold, dry conditions yielded noticeably lower results. This result at cold, dry conditions is unexpected considering JSC-RN is compositionally similar to both MMS and MMS·$NaClO_4$. It should be noted that the JSC-RN sample was significantly finer than the other simulants. Although derived from MMS sand (grain size: 3 μm to 2 mm), JSC-RN contained a smaller grain size distribution (3.0 – 600 μm). It is likely that the grain size distribution affected heating due to the thermal conductivity of coarser soils being roughly twice that of finer soils [84].

Measured dielectric losses, in general, do not directly correspond to dielectric heating of similar soil samples. Variations in temperature due to dielectric losses and energy transfer (or coupling) between microwave radiation and soil components are fundamentally different processes, albeit related. Furthermore, losses only characterize energy input to a system and do not provide any information regarding energy transformations or dissipations throughout the soil medium. Thermal properties of the soil (e.g., thermal conductivity and heat capacity) are independent of electrical properties, although they can be correlated. Moreover, if the irradiated sample is small (relative to the transmitting wavelength), compositionally uniform, well-insulated, the geometry of the transmission line and sample are well matched, and thermal properties are known, the resulting temperature rise should correlate to measured

Table 6.2: Heating rates of soil mixtures

Simulant	Heating Rate x10^{-3} [°C/s]
JSC-RN (AMBIENT)	3.54
JSC-RN (COLD-DRY)	1.51
JSC-RN (ICY-8 wt.%)	6.71
JSC-RN (ICY-22 wt.%)	6.01
MMS (AMBIENT)	4.46
MMS (COLD-DRY)	4.18
MMS (ICY-8 wt.%)	4.17
MMS (ICY-22 wt.%)	5.29
MMS-1.2 wt.% $NaClO_4$ (AMBIENT)	4.86
MMS-1.2 wt.% $NaClO_4$ (COLD-DRY)	3.07
MMS-1.2 wt.% $NaClO_4$ (ICY-8 wt.%)	4.33
MMS-1.2 wt.% $NaClO_4$ (ICY-22 wt.%)	7.14

losses. Thus, given these conditions, variations in dielectric losses within similar materials should correspond similarly in temperature. In other words, if dielectric losses are observed to increase in soils with higher water content, it would be expected that those soils would also generate a higher rise in temperature.

The latter point is furthered emphasized by comparing icy dielectric loss results (Fig. 5.11) and dielectric heating rates shown in Table 6.2 of icy MMS·$NaClO_4$. Dielectric loss measurements ascribe lower losses to the lower weight percent mixture (i.e., MMS·$NaClO_4$, 8.0 wt.%

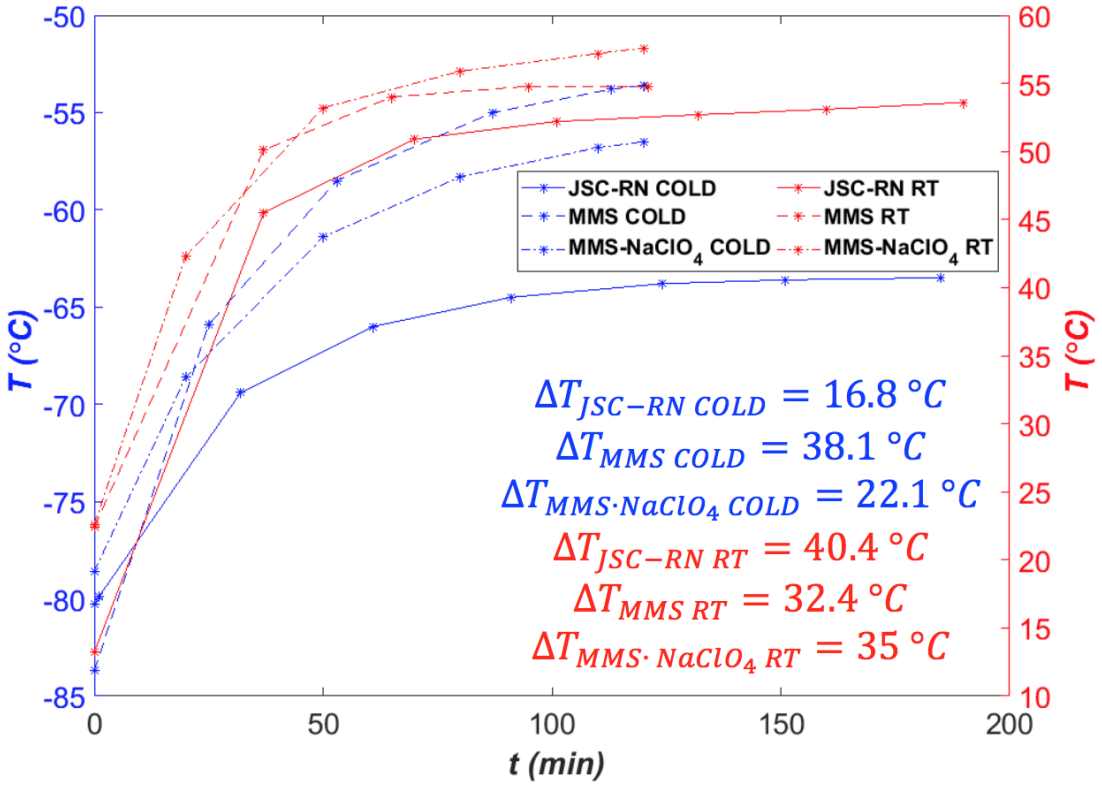

Figure 6.4: Thermal profiles of dry JSC-RN, MMS, and MMS·$NaClO_4$ samples at cold conditions (blue curves) and RT, i.e., ambient, conditions (red curves) when heated with 10 GHz microwave radiation at 1.2 and 1.3 W, respectively.

at 10.0 GHz), which is consistent with the lower heating rate when compared to the icier simulant (i.e., MMS·$NaClO_4$, 22.0 wt.%). Moreover, the dielectric heating rates of icy MMS simulants, which did not contain perchlorate, yield losses lower than the detectable limit of the PNA instrument, but appear to follow a similar heating trend. However, JSC-RN mixtures appear to have similar heating rates for both icy mixtures, although dielectric loss results ascribe higher losses to the icier mixture (i.e., JSC-RN, 22.0 wt.%).

Results demonstrate inhibited heating at cold conditions when compared with ambient for the same power setting at dry conditions for all simulants (Figure 6.4). The change in temperature, ΔT, is nearly 2.5 times greater at ambient conditions for all soils with the

exception of MMS. It should be noted that all samples achieved at least 65% of ΔT within the first 50 min of heating. Interestingly, significant heating was observed in MMS·$NaClO_4$ at cold conditions when compared with JSC-RN, although MMS is the base material for both simulants and despite the similar concentrations of sodium perchlorate.

Figure 6.5 displays results for icy soil mixtures. In general, icy samples yield higher changes in temperature during heating when compared to cold, dry soils. Moreover, of these, perchlorate mixtures at high water content (22.0 wt%) had the highest change in temperature overall.

Another interesting result that arose from these experiments involves the salt content in simulant soils and its impact on heating. It appears that perchlorate salts increased energy coupling when comparing icy MMS heating rates with icy JSC-RN and icy MMS·$NaClO_4$ because the perchlorate mixtures produced higher heating rates. The lower rate observed in JSC-RN soils is likely a result of lower thermal conductivity in finer graded soils [84]. However, enhanced heating effects in salty soils appears undermined in the absence of ice and can be seen when comparing cold, dry MMS with cold, dry MMS·$NaClO_4$ and JSC-RN. A potential explanation could be that this behavior is due to the adsorbed water layer structure within salty soils. Water adsorption to salt surfaces is similar to adsorption to silicate surfaces in that reversible physisorption (physical adsorption via hydrogen bonding) occurs at these surfaces [76]. Observations of water adsorption on NaCl at cryogenic temperatures (135 – 155 K) conclude that water molecules are more likely to adsorb uniformly to the salt surface (at low humidity) prior to adsorbing to other water molecules [76, 85]. Furthermore, adsorbed water layers at cryogenic temperatures are spectroscopically similar to ice [85], and most likely yield dielectric losses similar to those observed in ice. It is apparent that adsorbed layers of water in salty soils take a variety of forms at cold conditions. Thus, transitions in water adsorption in salty soils could potentially evolve with increasing water content in the manner described in Figure 6.6. At low humidity conditions, water adsorbs to the salt surface forming ice-like water layers uniformly along the salt surface. Adding water content would result in greater separation between the salt-soil interface as water molecules adsorb

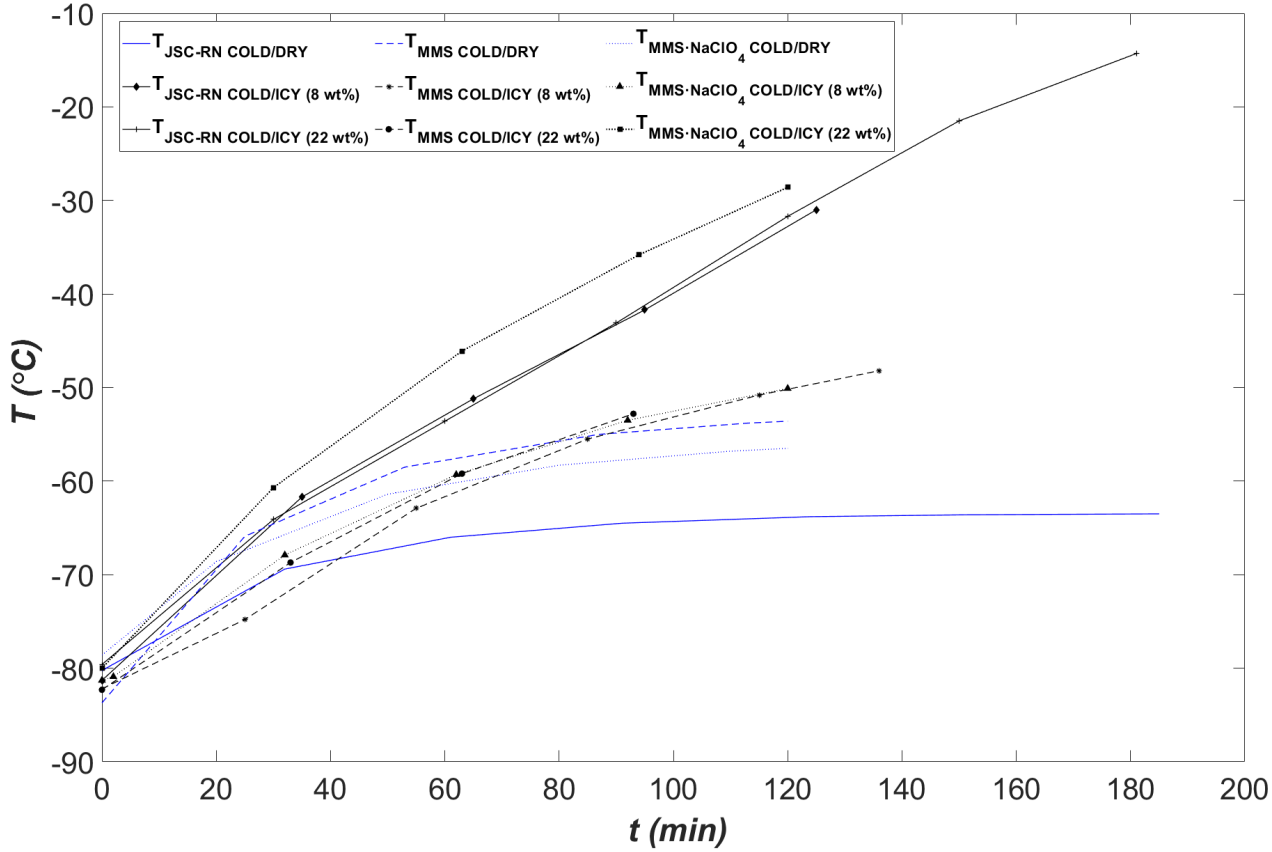

Figure 6.5: Thermal profiles of icy soil mixtures. Black curves represent icy mixtures of JSC-RN, MMS, and MMS·$NaClO_4$. Profiles at cold conditions (blue curves) from Figure 6.4 are reprinted for comparison.

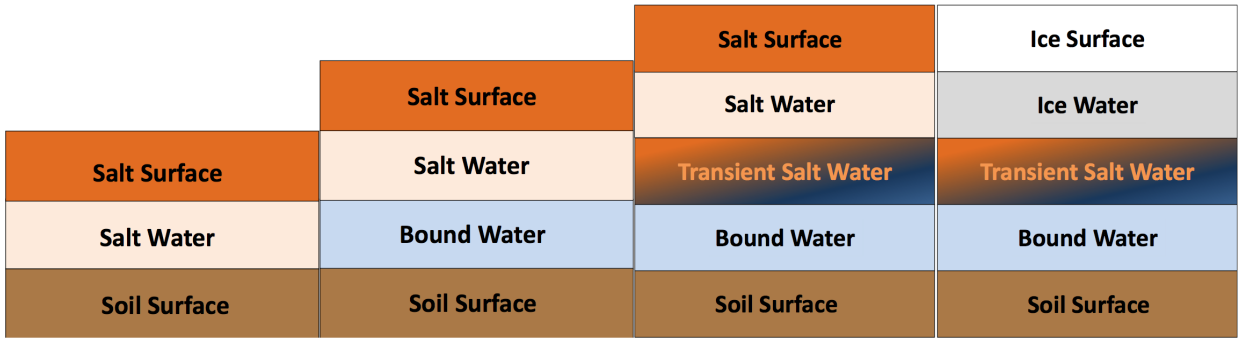

(A) (B) (C) (D)

Figure 6.6: Proposed transition of salt water interlayers within A) dry soils at low humidity (single layer adsorption), B - C) dry soils at increasing water content, and D) icy soils.

to each other creating a bound water layer. Further increasing water content would result in a mobile transient salt water layer forming in-between the salt water and bound water layers. Lastly, analogous to transient water layers in salt-free soils (Section 5.1), with the addition of ice, this salty, mobile layer would stabilize between the ice water layer and bound water layer. As discussed in Chapter 5, dielectric losses are higher in bound water layers than ice water layers. Salt water layers, resembling these ice water layers [85], are likely to also yield lower losses than bound water. Therefore, at cold conditions, bound water in salt-free, dry soils should produce higher losses than salty, dry soils, which is consistent with results in Table 6.2 and Figure 6.5. Similarly, salt solutions yield higher losses than pure water at frequencies within the microwave range [83]; thus, transient salt water layers are expected to be lossier than transient water layers within that frequency range. This effect can also be inferred from results displayed in Table 6.2. It should be noted that this proposed transient salt water theory assumes all salts dissolve in the transient water layer when ice is present and is empirically derived to reconcile observed dielectric heating effects of icy and dry soils at cold conditions. Furthermore, this theory is specifically for water adsorption within soil media and only considers water adsorption on soil mineral surfaces, salts, and ice.

It was observed that insulation of the foam soil sample has a crucial effect on the measured

temperature change. Given the low temperature of the freezer and the wall thickness of the foam sample holder, it was observed that further insulating the aft end of the sample holder with an additional piece of foam (∼3.0 cm thick and 15.0 cm in length) increased ΔT by ∼10°C in cold JSC-RN (Fig. 6.7). Moreover, the backing foam provided better contact between the forward end of the sample holder and the waveguide exit aperture. Prior to using the backing foam, small air gaps (Fig. 6.7) were present between the exit aperture and forward end of the sample holder, which could have diffused incident radiation. Figure 6.8 displays icy JSC-RN (22.0 wt%) with additional insulation plotted with icy JSC-RN results from Figure 6.5. These results demonstrate that increasing insulation can yield higher changes in temperature. More importantly, temperatures within the sample holder reached just below freezing (∼2°C) within 250 min of heating. Moreover, increasing the wall thickness of the sample holder combined with an insulating backing structure would likely increase the temperature above freezing within a similar time interval.

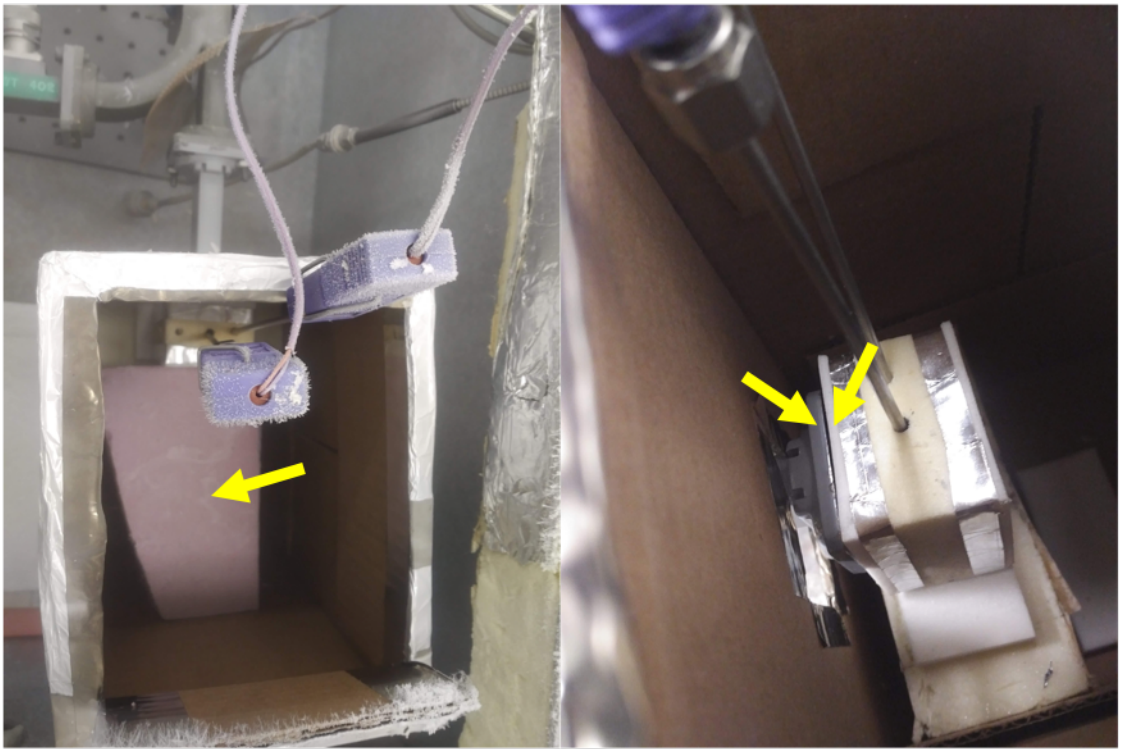

Figure 6.7: Left image: Top down view of foam sample holder showing the thermocouples within the sample (left) and sample holder wall (right). The yellow arrow points to foam bracing against the wall of the Faraday cage and aft end of sample holder. Right image: Yellow arrows point to air gap between waveguide and sample holder.

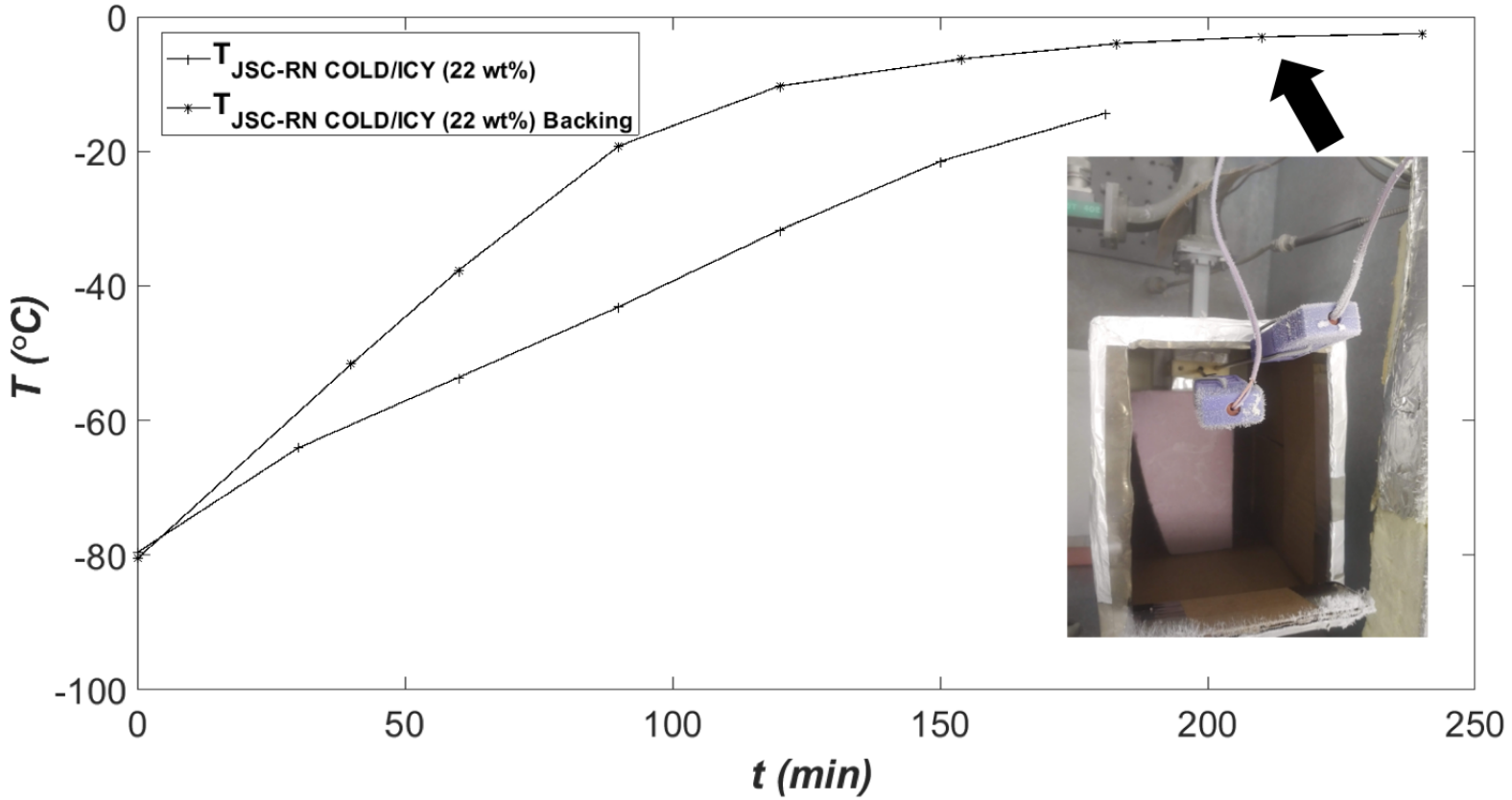

Figure 6.8: Thermal profiles of icy JSC-RN (22.0 wt%) with and without insulation backing.

6.3 Implications for Dielectric Heating on Mars

Transitioning the techniques of this heating experiment to simulate heat transfer effects expected at the near-surface of Mars while targeting heating rates from Section 6.2 would most likely require higher power input. Additionally, consideration should be given to the penetration depth, D_p, i.e., the distance to which the amplitude of the penetrating electric field falls to 1/e of its value at the surface, which is a function of the complex permittivity of soil components and the radiating frequency [21].

$$D_p = \frac{\lambda_0}{2\pi\sqrt{2\varepsilon'}\sqrt{\sqrt{1+\left(\frac{\varepsilon''}{\varepsilon'}\right)^2}-1}} \tag{6.2}$$

The penetration depth (Eq. 6.2) for non-magnetic media (i.e., $\mu = 1$) increases with increasing wavelength (decreasing frequency). At 10.0 GHz, with losses observed in salty, icy soils (Fig. 5.11), penetration would be limited to 2.0 – 8.0 cm (Table 6.3). However, penetration in lower loss soils can extend up to 10.0 m. Thus, although lossiness has heating benefits, increasing losses decreases penetration into the subsurface [21, 86]. However, temperature profiles in the subsurface would also be a function of the thermal properties of Mars soils, particularly the thermal conductivity. Results from the Phoenix Lander TECP (Thermal and Electrical Conductivity Probe) indicate that soils within 1.5 cm of the subsurface are thermally insulating, having an overall average thermal conductivity of 0.085 $\frac{\mathrm{W}}{\mathrm{mK}}$ [6]. Thermal conductivities in dry Mars simulants at cold conditions have been observed to be similar, yet increase by an order of magnitude with ice content [87]. The foam frame and end pieces have thermal conductivities of approximately 0.022 and 0.045 $\frac{\mathrm{W}}{\mathrm{mK}}$, respectively at ambient conditions. Although thermal conductivity can vary with temperature, if the thermal conductivity of the foam sample holder is considered invariant, then at cold conditions, the sample holder as actually more insulative than the soil sample, particularly for icy soils.

Measurements described in this chapter demonstrate the sensitivity of energy coupling to environmental conditions, specifically water and salt content at cold conditions. The advantage of performing energy coupling experiments with insulation provides an opportunity to

Table 6.3: Penetration depth of microwave radiation at 10.0 GHz

Simulant	Depth [m]
JSC-RN (COLD-DRY)	3.0
JSC-RN (ICY-8 wt.%)	0.07
JSC-RN (ICY-22 wt.%)	0.02
MMS (COLD-DRY)	4.8
MMS (ICY-8 wt.%)	9.7
MMS (ICY-22 wt.%)	5.3
MMS-1.2 wt.% $NaClO_4$ (COLD-DRY)	4.5
MMS-1.2 wt.% $NaClO_4$ (ICY-8 wt.%)	0.08
MMS-1.2 wt.% $NaClO_4$ (ICY-22 wt.%)	0.02

isolate energy coupling to soil components from heat transfer effects (i.e., thermal conduction) thereby identifying the heating potential as a function of inherent loss mechanisms and power input. Under these conditions, to wit: low-loss materials at low power, large temperature changes are not expected to occur within samples. Moreover, at these conditions, given long time intervals, temperatures above freezing could be achieved. However, this approach is not realistic for the near-surface of Mars and only represents an upper limit to achievable temperature increases in *in-situ* soils, particularly due to the lower thermal conductivity of the foam sample holder. It is important to also recognize that these conclusions are based on heating experiments of simulants that may not fully characterize the subsurface of Mars. Therefore, the penetration depth combined with thermal properties is a critical component of subsurface heating that would provide insight into the temperature distribution generated by dielectric losses.

Lastly, Allan et al., 2013 performed dielectric heating experiments with lunar simulants at ambient conditions in a 2.45 GHz heating chamber. These experiments applied 1.0 kW of power to 1.35-kg of simulant and resulted in a $\sim 1100°C$ temperature change over the course of 90 min. Although energy coupling at cold conditions may reduce this effect significantly, excessive heating of this degree caused melting and chemical alteration of the simulant [88]. There may be applications for melting of soil materials (e.g., extraction of water in hydrated minerals [89], processing building materials [90], etc.); but the extraction of subsurface ice and adsorbed water would not require soils to be heated to the extent discussed in Allan et al., 2013. Furthermore, temperatures just above freezing may be sufficient for water vapor extraction. However, optimization of extraction rates as a function of temperature need to be investigated. Furthermore, alteration of the soil material (due to excessive heating) could undermine water extraction efforts by introducing impurities to the extracted water vapor. Thus, consideration should be given to maintaining minimum power levels for longer time intervals to extract subsurface water.

Chapter 7

IMPLICATIONS FOR ASTROBIOLOGY

Irradiation of the soil subsurface with microwave radiation for water extraction on Mars could have an impact on microbial life. In general, soil bacteria display a range of tolerances when exposed to microwave radiation [91]. The use of microwave radiation at 2.45 GHz has been observed to selectively eliminate particular plant pathogens in soil samples, such as fungal microbes, while having a reduced influence on bacterial populations [92–94]. Soils heated to 60°C have been demonstrated to significantly or entirely reduce fungal colonies [92, 93]. Interestingly, short term (∼20 s) microwave radiation exposure of *Thiobacillus*, in organic and brown earth soils was observed to enhance bacterial populations [93]. Although it is unclear which species of *Thiobacillus* was used in Wainwright, 1980, thermophilic *Thiobacillus* species have been observed to sustain growth up to 52°C [95]. Although several of the aforementioned authors comment on microwave irradiation of soils containing microbes, there does not appear to be much documentation of microwave effects on thermophilic or psychrophilic (low-temperature resistant) microorganisms. As discussed in Chapter 5 and Chapter 6, enhanced thermal effects can result when irradiating icy soils, especially soils containing salts. This is particularly relevant for Mars where microbial life, if present, would most likely have adapted to the cold, dry conditions of the subsurface.

It should be noted that sterilization or microbicidal effects are not directly due to microwave radiation exposure. Rather, these effects are the direct result of elevated temperatures occurring due to energy coupling within the soil, which varies as a function of moisture content [96]. Indeed, thermal effects imposed by conventional heating methods yielded similar microbicidal results [97]. Moreover, sustained irradiation (approximately four minutes at 1.0 kW, 2.45 GHz) of commercially dried yeast (0.1% moisture content) outside of a soil

medium (i.e., direct irradiation of the yeast) demonstrated minimal microbicidal effects compared to a 25% survival rate of an identical sample suspended in distilled water after 20 s of microwave radiation exposure [96]. A similar experiment was conducted with a variety of bacteria and bacteriophages (viruses unique to bacteria and archaea), yielding similar results [96]. This highlights the low loss nature of microbial species containing low water content and further demonstrates that thermal effects enhanced by water content (whether internal or external to the microbial cell) is the primary consequence of microwave irradiation on microbial life. Thus, as discussed in Chapter 6, heating dry soils to extract adsorbed water may not be as detrimental if extant life can tolerate temperature environments just above freezing.

However, if microbial cells contain significant amounts of water, microbicidal effects of microwave radiation on microbial populations in soils are enhanced. In the case of high intercelluar water, dipolar dielectric loss mechanisms would dominate in the microwave region covered by this dissertation, particularly free water (Figure 2.1). Moreover, as demonstrated in Chapter 5, dielectric losses in icy soils are dominated by free water loss mechanisms, but overall heating would be a function of total water content, volume, and insulation effects. When irradiating soils with microbes, energy couples directly into the microbial cell and results in a rapid increase in temperature (50 – 90 °C). This temperature increase compromises cell membrane stability and leads to mechanical rupture of the cell [98]. However, in the absence of polar/ionic molecules, mechanisms contributing to dielectric losses are reduced by several orders of magnitude and lethal amounts of energy needed to destroy microbial cells may not be reached [96]. In general, soil type has minimal effects on dielectric heating due to the narrow range of specific heat capacities expected for mineral soils [92]. Moreover, mineral content was not observed to influence heating on the simulant soils analyzed in Chapter 6. Heating rates for all simulants were similar, although enhanced heating was observed in soils containing ice. However, if the soil matrix on Mars contains components that enhance losses (e.g., salts and ice), and irradiation is sustained, coupled energy can conduct into the microbial cell and still cause disruption of the cell membrane.

Lastly, Islam et al., 1998 reported that irradiation of soils with microwaves could also be used to measure biomass carbon when elevated soil temperatures rupture microbial cells and release intracellular compounds. Additionally, irradiation of soils at levels lower than 800 J/g have been reported to not breakdown non-biomass carbon nor drastically affect soil nutrients [92, 98, 99]). Therefore, irradiating soils with microwaves could be a useful tool for the detection of evidence to support past or present life.

Chapter 8

CONCLUSION

A major conclusion of the research in this dissertation has been recognizing the key to dielectric heating of cold soils is coupling microwave radiation to transient adsorbed water. Dielectric heating of icy soils is strongly dependent on this transient water layer. Thus, development and optimization of energy coupling to this unfrozen water would significantly benefit water extraction efforts with dielectric heating.

Although the feasibility study diagnosed the waveguide method as a preferred method for soil analysis over coaxial reflection techniques, the low loss nature of cold soils requires a measurement method that offers higher accuracy and precision. The waveguide method is certainly suitable for moderate to high loss materials, which was evident for higher loss soil samples (e.g., ambient/dry and icy soils) observed in Chapter 5. However, future work that seeks to investigate the contributions of adsorbed water at cold conditions will require a different method. Additionally, addressing losses attributed to grain size would also require a more precise measurement method. An alternative measurement technique that was not pursued during this research, but could be useful for low loss measurements, is the resonant cavity perturbation method (or simply 'resonant cavity method'). This method entails enclosing a small sample in a cavity structure (rectangular cavities are common and are structurally similar to rectangular waveguides) and determining the resonant frequency of the cavity with and without the sample. Unlike the waveguide method, temperature-dependent calibrations using calibration standards are not needed. Furthermore, iterative techniques are not required to determine the complex permittivity and can be directly calculated from the resonant frequencies, sample/cavity volume, and output power [100]. Future work with this method could investigate temperature-dependent loss mechanisms and ana-

lyze the impact of cold, vacuum conditions on adsorbed water layers. These investigations would better inform the nature of dielectric loss at the low pressure, cold conditions that are observed at the surface of Mars.

Complex permittivity and dielectric heating, albeit linked, are fundamentally different processes and should be analyzed with that understanding in mind. The former assesses electrical properties via interactions between an electric field and soil, while the latter assesses energy coupling via temperature variation and the thermal properties of soils. Another aspect to keep in mind with this line of research is that changes in temperature of soils heated by dielectric energy coupling is a product of the thermal properties of the soil and energy transfer mechanisms (e.g., conductive heat transfer). Although care was taken during heating experiments to minimize heat transfer effects, such that the resulting temperature change could be directly linked to dielectric losses in the soil, identification of the impact on temperature with increased losses is challenging. At times dielectric loss measurements appeared inconsistent with observed heating effects for low loss samples, which is likely indicative of the limitation of the waveguide method for measuring low loss materials.

Ultimately, this dissertation has observed the impact that transient adsorbed water has on dielectric heating. Microwave radiation from 2.6 – 18 GHz couples most efficiently with liquid water at ambient conditions ($\sim$20°C). Cold conditions greatly reduce dielectric losses due to temperature-dependent shifting of loss mechanisms and the absence of liquid water at cold conditions. Yet, energy coupling was enhanced at cold conditions in icy, salty soils due to transient liquid water layers. In fact, heating rates in icy, salty soils (22.0 wt.%) exceeded heating rates at ambient conditions across all soils analyzed. Interestingly, heating within cold, dry soils appeared inhibited by salts when compared to soils without salts. Therefore, dielectric heating of indigenous soils on Mars may not be impacted significantly by mineral composition; rather, heating effects would primarily be a function of ice and salt content.

The topic of subsurface water extraction via dielectric heating would benefit from an understanding of how power input and heating time can be optimized for *in-situ* heating of subsurface soils on Mars. Dielectric heating experiments performed in this dissertation

included moderate control over heat transfer effects. However, heat transfer to the soil subsurface introduces conduction effects that would significantly reduce the change in temperature observed in Chapter 6. Moreover, the thermal properties of simulants (and the indigenous soils of Mars) would most likely produce lower heating rates than those observed in Chapter 6 if dielectric heating were applied without insulation. Although soils on Mars have been observed to be have low thermal conductivity, the experimental components in Chapter 6 were more insulative. Moreover, heating experiments were performed on samples with spatial dimensions similar to the microwave radiation wavelengths. In other words, although the penetration depth for dielectric heating results was introduced in Chapter 6, its impact on dielectric heating was not addressed in this dissertation. Yet, on the surface of Mars, assessment of the depth of water resources and the spatial heating range are critical factors in determining effective heating strategies for subsurface water extraction. Future work should model thermal environmental effects combined with soil thermal properties to model the thermal evolution in soils irradiated with microwave radiation.

Direct applications for this research could include small-scale devices used to "farm" water from the subsurface of Mars with either a handheld or rover-deployed device. Microwave frequency transmission allows for smaller scale components (similar to the experimental setup in Chapter 6) that could be configured to operate remotely or *in-situ*. However, optimization of power requirements and extractions rates would need to be assessed. It should be noted that although this dissertation focused on dielectric heating in the microwave region, lower frequency regions (e.g., 1.0 – 10 kHz) could also be considered, particularly for large-scale applications (e.g., transmission from orbit). However, transmission at these frequencies would require very large antennas (on the order of kilometers) which may be impractical to implement.

Lastly, temperature control using microwave radiation would be the most critical parameter to assess the impact of microwave radiation on microbial life in the near-surface of planetary bodies. This dissertation documented the nature of dielectric loss in dry soils and the resulting thermal effects. Heating of salty, icy soils produced the highest thermal

response, thus water extraction efforts could have implications for microbial life in icy soils in the subsurface of Mars. However, dielectric heating of soils could also be a reliable method of preserving biomass for detection of past or present life.

REFERENCES

[1] Bell, J., *The Martian Surface: Composition, Mineralogy, and Physical Properties*, New York: Cambridge University Press, 2008.

[2] Orosei, R., Lauro, S. E., Pettinelli, E., Cicchetti, A., Coradini, M., Cosciotti, B., Di Paolo, F., Flamini, E., Mattei, E., Pajola, M., Soldovieri, F., Cartcci, M., Cassenti, F., Figeri, A., Giuppi, S., Martufi, R., Masdea, A., Mitri, G., Nenna, C., Noschese, R., Restano, M., and Seu, R., "Radar evidence of subglacial liquid water on Mars," *Science*, Vol. 361, No. 6401, 2018, pp. 490–493.

[3] Feldman, W. C., Prettyman, T. H., Maurice, S., Plaut, J. J., Bish, D. L., Vaniman, D. T., Mellon, M. T., Metzger, A. E., Squyres, S. W., Karunatillake, S., Boynton, W. V., Elphic, R. C., Funsten, H. O., Lawrence, D. J., and Tokar, R. L., "Global distribution of near-surface hydrogen on Mars," *Journal of Geophysical Research: Planets*, Vol. 109, 2004.

[4] Boynton, W. V., Feldman, W. C., Squyres, S. W., Prettyman, T. H., Brückner, J., Evans, L. G., Reedy, R. C., Starr, R., Arnold, J. R., Drake, D. M., Englert, P. A. J., Metzger, A. E., Mitrofanov, I., Trombka, J. I., d'Uston, C., Wänke, H., Gasnault, O., Hamara, D. K., Janes, D. M., Marcialis, R. L., Maurice, S., Mikheeva, I., Taylor, G. J., Tokar, R., and Shinohara, C., "Distribution of Hydrogen in the Near Surface of Mars: Evidence for Subsurface Ice Deposits," *Science*, Vol. 297, No. 5578, 2002, pp. 81–85.

[5] Wilson, J. T., Eke, V. R., Massey, R. J., Elphic, R. C., Feldman, W. C., Maurice, S., and Teodoro, L. F. A., "Equatorial locations of water on Mars: Improved resolution maps based on Mars Odyssey Neutron Spectrometer data," *Icarus*, Vol. 299, 2018, pp. 148–160.

[6] Zent, A. P., Hecht, M. H., Cobos, D. R., Wood, S. E., Hudson, T. L., Milkovich, S. M., DeFlores, L. P., and Mellon, M. T., "Initial results from the thermal and electrical conductivity probe (TECP) on Phoenix," *Journal of Geophysical Research: Planets*, Vol. 115, 2010.

[7] Schneider, M., *Experimental Investigation of Water Vapor Adsorption by Molecular Sieve Zeolite 3A under Simulated Martian Atmospheric Conditions*, Master's thesis, Department of Aeronautics and Astronautics, University of Washington, Seattle, WA, 2001.

[8] Ethridge, E. and Kaukler, W., "Extraction of Water from Polar Lunar Permafrost with Microwaves-Dielectric Property Measurements," *Proceedings of the 47th AIAA Aerospace Sciences Meeting*, AIAA, Orlando, FL, 2009.

[9] Ethridge, E. and Kaukler, W., "Microwave Processing of Planetary Surfaces for the Extraction of Volatiles," *Proceedings of the 49th AIAA Aerospace Sciences Meeting*, AIAA, Orlando, FL, 2011.

[10] Ethridge, E. and Kaukler, W., "Finite Element Analysis of Three Methods for Microwave Heating of Planetary Surfaces," *Proceedings of the 50th AIAA Aerospace Sciences Meeting*, AIAA, Nashville, TN, 2012.

[11] Sanders, G. B. and Mueller, R. P., "Mars Soil-Based Resource Processing and Planetary Protection," *Proceedings of the NASA Exploration Science Forum*, Solar System Exploration Research Institute, Moffet, CA, 2015, p. 1026.

[12] Voytek, M. A., "NASA Astrobiology Strategy 2015," *Astrobiology*, Vol. 16, No. 8, 2016, pp. 654–656.

[13] Des Marais, D. J., Nuth III, J. A., Allamandola, L. J., Boss, A. P., Farmer, J. D., Hoehler, T. M., Jakosky, B. M., Meadows, V. S., Pohorille, A., Runnegar, B., and

Spormann, A. M., "The NASA astrobiology roadmap," *Astrobiology*, Vol. 8, No. 4, 2008, pp. 715–730.

[14] Maurice, S., Feldman, W., Diez, B., Gasnault, O., Lawrence, D. J., Pathare, A., and Prettyman, T., "Mars Odyssey neutron data: 1. Data processing and models of water-equivalent-hydrogen distribution," *Journal of Geophysical Research: Planets*, Vol. 116, 2011.

[15] Milliken, R. E., Mustard, J. F., Poulet, F., Jouglet, D., Bibring, J.-P., Gondet, B., and Langevin, Y., "Hydration state of the Martian surface as seen by Mars Express OMEGA: 2. H_2O content of the surface," *Journal of Geophysical Research: Planets*, Vol. 112, 2007.

[16] Fialips, C. I., Carey, J. W., Vaniman, D. T., Bish, D. L., Feldman, W. C., and Mellon, M. T., "Hydration state of zeolites, clays, and hydrated salts under present-day martian surface conditions: Can hydrous minerals account for Mars Odyssey observations of near-equatorial water-equivalent hydrogen?" *Icarus*, Vol. 178, 2005, pp. 74–83.

[17] Meslin, P.-Y., Gasnault, O., Forni, O., Schröder, S., Cousin, A., Berger, G., Clegg, S. M., Lasue, J., Maurice, S., Sautter, V., Le Mouélic, S., Wiens, R. C., Fabre, C., Goetz, W., Bish, D., Mangold, N., Ehlmann, B., Lanza, N., Harri, A.-M., Anderson, R., Rampe, E., McConnochie, T. H., Pinet, P., Blaney, D., Léveillé, R., Archer, D., Barraclough, B., Bender, S., Blake, D., Blank, J. G., Bridges, N., Clark, B. C., DeFlores, L., Delapp, D., Dromart, G., Dyar, M. D., Fisk, M., Gondet, B., Grotzinger, J., Herkenhoff, K., Johnson, J., Lacour, J.-L., Langevin, Y., Leshin, L., Lewin, E., Madsen, M. B., Melikechi, N., Mezzacappa, A., Mischna, M. A., Moores, J. E., Newsom, H., Ollila, A., Perez, R., Renno, N., Sirven, J.-B., Tokar, R., de la Torre, M., d'Uston, L., Vaniman, D., Yingst, A., and MSL Science Team, "Soil Diversity and Hydration as Observed by ChemCam at Gale Crater, Mars," *Science*, Vol. 341, No. 6153, 2013.

[18] Smith, M. D., "The annual cycle of water vapor on Mars as observed by the Thermal Emission Spectrometer," *Journal of Geophysical Research: Planets*, Vol. 107, 2002.

[19] Pommerol, A., Schmitt, B., Beck, P., and Brissaud, O., "Water sorption on martian regolith analogs: Thermodynamics and near-infrared reflectance spectroscopy," *Icarus*, Vol. 204, 2009, pp. 114–136.

[20] Ray, P. S., "Broadband Complex Refractive Indices of Ice and Water," *Applied Optics*, Vol. 11, No. 8, 1972, pp. 1836–1844.

[21] Metaxas, A., , and Meredith, R. J., *Industrial Microwave Heating*, London: Peter Peregrinus Ltd., 1983.

[22] Stillman, D. E. and Olhoeft, G. R., "GPR and Magnetic Minerals at Mars Temperatures," *Proceedings of the Tenth International Conference on Ground Penetrating Radar*, IEEE, Delft, The Netherlands, 2004, pp. 735–738.

[23] Hasted, J. B., *Aqueous Dielectrics*, New York: John Wiley & Sons, Inc., 1973.

[24] Serdyuk, V. M., "Dielectric Study of Bound Water in Grain at Radio and Microwave Frequencies," *Progress In Electromagnetics Research*, Vol. 84, 2008, pp. 379–406.

[25] Scott, A. W., *Understanding Microwaves*, New York: John Wiley & Sons, 1993.

[26] Pozar, D. M., *Microwave Engineering*, Reading: Addison-Wesley, 1990.

[27] Ramo, S., Whinnery, J. R., and Van Duzer, T., *Fields and Waves in Communication Electronics*, New York: John Wiley & Sons, 2nd ed., 1984.

[28] Zhang, K. and Li, D., *Electromagnetic Theory for Microwaves and Optoelectronics*, Berlin: Springer, 2008.

[29] Blake, L. V., *Transmission lines and waveguides*, New York: John Wiley & Sons, 1969.

[30] Anritsu, "Understanding VNA Calibration," Part No 111410-00673A, 2012.

[31] Baker-Jarvis, J., Vanzura, E. J., and Kissick, W. A., "Improved Technique for Determining Complex Permittivity with the Transmission/Reflection Method," *IEEE Transactions on Microwave Theory and Techniques*, Vol. 38, No. 8, 1990, pp. 1096–1103.

[32] Nicolson, A. M. and Ross, G. F., "Measurement of the Intrinsic Properties of Materials by Time-Domain Techniques," *IEEE Transactions on Instrumentation and Measurement*, Vol. IM-19, No. 4, 1970, pp. 377–382.

[33] Weir, W. B., "Automatic Measurement of Complex Dielectric Constant and Permeability at Microwave Frequencies," *Proceedings of the IEEE*, Vol. 62, No. 1, 1974, pp. 33–36.

[34] Kent, S. and Günel, T., "Dielectric Permittivity Estimation of Cylindrical Objects Using Genetic Algorithm," *Journal of Microwave Power and Electromagnetic Energy*, Vol. 32, No. 2, 1997, pp. 109–113.

[35] Whitley, D., "A genetic algorithm tutorial," *Statistics and Computing*, Vol. 4, No. 2, 1994, pp. 65–85.

[36] Agilent, "Agilent: Understanding and Improving Network Analyzer Dynamic Range," Agilent Technologies, 5980-2778EN, 2000.

[37] Morris, R. V., Golden, D. C., Bell, J. F., Shelfer, T. D., Scheinost, A. C., Hinman, N. W., Furniss, G., Mertzman, S. A., Bishop, J. L., Ming, D. W., Allen, C. C., and Britt, D. T., "Mineralogy, composition, and alteration of Mars Pathfinder rocks and soils: Evidence from multispectral, elemental, and magnetic data on terrestrial analogue, SNC meteorite, and Pathfinder samples," *Journal of Geophysical Research: Planets*, Vol. 105, 2000, pp. 1757–1817.

[38] Peters, G. H., Abbey, W., Bearman, G. H., Mungas, G. S., Smith, J. A., Anderson, R. C., Douglas, S., and Beegle, L. W., "Mojave Mars simulant—Characterization of a new geologic Mars analog," *Icarus*, Vol. 197, 2008, pp. 470–479.

[39] Hogancamp, J. V. et al., "JSC-Rocknest: a Large-Scale Mojave Mars Simulant (MMS) Based Soil Simulant for In-Situ Resource Utilization Water-Extraction Studies," *In preparation for Icarus*.

[40] Sutter, B., McAdam, A. C., Mahaffy, P. R., Ming, D. W., Edgett, K. S., Rampe, E. B., Eigenbrode, J. L., Franz, H. B., Freissinet, C., Grotzinger, J. P., Steele, A., House, C. H., Archer, P. D., Malespin, C. A., Navarro-González, R., Stern, J. C., Bell, J. F., Calef, F. J., Gellert, R., Glavin, D. P., Thompson, L. M., and Yen, A. S., "Evolved gas analyses of sedimentary rocks and eolian sediment in Gale Crater, Mars: Results of the Curiosity rover's sample analysis at Mars instrument from Yellowknife Bay to the Namib Dune," *Journal of Geophysical Research: Planets*, Vol. 122, No. 12, 2017, pp. 2574–2609.

[41] Navarro-González, R., Vargas, E., de La Rosa, J., Raga, A. C., and McKay, C. P., "Reanalysis of the Viking results suggests perchlorate and organics at midlatitudes on Mars," *Journal of Geophysical Research: Planets*, Vol. 115, 2010.

[42] Hecht, M. H., Kounaves, S. P., Quinn, R. C., West, S. J., Young, S. M. M., Ming, D. W., Catling, D. C., Clark, B. C., Boynton, W. V., Hoffman, J., DeFlores, L. P., Gospodinova, J., Kapit, J., and Smith, P. H., "Detection of Perchlorate and the Soluble Chemistry of Martian Soil at the Phoenix Lander Site," *Science*, Vol. 325, 2009, pp. 64–67.

[43] Ojha, L., Wilhelm, M. B., Murchie, S. L., McEwen, A. S., Wray, J. J., Hanley, J., Massé, M., and Chojnacki, M., "Spectral evidence for hydrated salts in recurring slope lineae on Mars," *Nature Geoscience*, Vol. 8, No. 11, 2015, pp. 829–833.

[44] Kounaves, S. P., Chaniotakis, N. A., Chevrier, V. F., Carrier, B. L., Folds, K. E., Hansen, V. M., McElhoney, K. M., ONeil, G. D., and Weber, A. W., "Identification of the perchlorate parent salts at the Phoenix Mars landing site and possible implications," *Icarus*, Vol. 232, 2014, pp. 226–231.

[45] Leshin, L. A., Mahaffy, P. R., Webster, C. R., Cabane, M., Coll, P., Conrad, P. G., Archer, P. D., Atreya, S. K., Brunner, A. E., Buch, A., Eigenbrode, J. L., Flesch, G. J., Franz, H. B., Freissient, C., Glavin, D. P., McAdam, A. C., Miller, K. E., Ming, D. W., Morris, R. V., Navarro-González, R., Niles, P. B., Owen, T., Pepin, R. O., Squyres, S., Steele, A., Stern, J. C., Summons, R. E., Sumner, D. Y., Sutter, B., Szopa, C., Teinturier, S., Trainer, M. G., Wray, J. J., Grotzinger, J. P., and MSL Science Team, "Volatile, Isotope, and Organic Analysis of Martian Fines with the Mars Curiosity Rover," *Science*, Vol. 341, No. 6153, 2013.

[46] Hogancamp, J. V., Archer, P. D., Gruener, J., Ming, D. W., and Tu, V., "JSC-Rocknest: a Large-Scale Mojave Mars Simulant (MMS) Based Soil Simulant for In-Situ Resource Utilization Water-Extraction Studies," *Proceedings of the 50th Lunar and Planetary Science Conference*, Lunar and Planetary Institute, The Woodlands, TX, 2019.

[47] Loewer, M., Igel, J., and Wagner, N., "Spectral Decomposition of Soil Electrical and Dielectric Losses and Prediction of *In Situ* GPR Performance," *IEEE Journal of Selected Topics in Applied Earth Observations and Remote Sensing*, Vol. 9, No. 1, 2016, pp. 212–220.

[48] Boivin, A. L., Hickson, D., Tsai, C., Cunje, A., Ghent, R. R., and Daly, M. G., "Broadband Measurements of the Complex Permittivity of Carbonaceous Asteroid Regolith Analog Materials," *Journal of Geophysical Research: Planets*, Vol. 123, No. 12, 2018, pp. 3088–3104.

[49] Stillman, D. and Olhoeft, G., "Frequency and temperature dependence in electromagnetic properties of Martian analog minerals," *Journal of Geophysical Research: Planets*, Vol. 113, 2008.

[50] Keysight, "Keysight 85070E: Dielectric Probe Kit 200 MHz to 50 GHz," Keysight Technologies, 5989-0222EN, August 2014.

[51] Keysight, "Keysight 85071E: Materials Measurement Software," Keysight Technologies, 5988-9472EN, August 2014.

[52] Zent, A. P., Hecht, M. H., Cobos, D. R., Campbell, G. S., Campbell, C. S., Cardell, G., Foote, M. C., Wood, S. E., and Mehta, M., "Thermal and Electrical Conductivity Probe (TECP) for Phoenix," *Journal of Geophysical Research: Planets*, Vol. 114, 2009.

[53] Leuschen, C., "Analysis of the Complex Permittivity and Permeability of a Martian Soil Simulant from 10 MHz to 1 GHz," *Proceedings of the International Geoscience and Remote Sensing Symposium*, IEEE, Hamburg, Germany, 1999, pp. 2264–2266.

[54] Deshpande, M. D., Reddy, C. J., Tiemsin, P. I., and Cravey, R., "A New Approach to Estimate Complex Permittivity of Dielectric Materials at Microwave Frequencies using Waveguide Measurements," *IEEE Transactions on Microwave Theory and Techniques*, Vol. 45, No. 3, 1997, pp. 359–366.

[55] Ghodgaonkar, D., Varadan, V., and Varadan, V., "Free-Space Measurement of Complex Permittivity and Complex Permeability of Magnetic Materials at Microwave Frequencies," *IEEE Transactions on Instrumentation and Measurement*, Vol. 39, No. 2, 1990, pp. 387–394.

[56] ASTM, "Standard Test Method for Measuring Relative Complex Permittivity and Relative Magnetic Permeability of Solid Materials at Microwave Frequencies Using Waveguide," American Society for Testing and Materials, Document D5568-14, West Conshohocken, PA, November 2014.

[57] Jacob, M. V., Mazierska, J., Leong, K., and Krupka, J., "Microwave Properties of Low-Loss Polymers at Cryogenic Temperatures," *IEEE Transactions on Microwave Theory and Techniques*, Vol. 50, No. 2, 2002, pp. 474–480.

[58] Geyer, R. G. and Krupka, J., "Microwave Dielectric Properties of Anisotropic Mate-

rials at Cryogenic Temperatures," *IEEE Transactions on Instrumentation and Measurement*, Vol. 44, No. 2, 1995, pp. 329–331.

[59] Keysight, "Keysight PNA Series Network Analyzers," Keysight Technologies, E8364-90031, December 2014.

[60] Curtis, J. O., "Microwave Dielectric Behavior of Soils. Report 1. Summary of Related Research and Applications," Waterways Experiment Station, Technical Report EL-93-25, Vicksburg, MS, December 1993.

[61] Debye, P. J. W., *Polar Molecules*, New York: Chemical Catalog Company, Inc., 1929.

[62] Matsuoka, T., Fujita, S., and Mae, S., "Dielectric Properties of Ice Containing Ionic Impurities at Microwave Frequencies," *Journal of Physical Chemistry B*, Vol. 101, No. 32, 1997, pp. 6219–6222.

[63] Ulaby, F. T., Moore, R. K., and Fung, A. K., *Microwave Remote Sensing: Active and Passive. Volume III-From Theory to Applications*, Reading: Addison-Wesley, Inc., 1986.

[64] Grimm, R. E., Stillman, D. E., Dec, S. F., and Bullock, M. A., "Low-Frequency Electrical Properties of Polycrystalline Saline Ice and Salt Hydrates," *The Journal of Physical Chemistry B*, Vol. 112, No. 48, 2008, pp. 15382–15390.

[65] Campbell, J. E., "Dielectric Properties and Influence of Conductivity in Soils at One to Fifty megahertz," *Soil Science Society of America*, Vol. 54, No. 2, 1990, pp. 332–341.

[66] Komarov, S. A., Mironov, V. L., and Romanov, A. N., "The Effect of Salinity on the Permittivity of Moist Soils in the Microwave Band," *Journal of Communications Technology and Electronics*, Vol. 47, No. 6, 2002, pp. 626–631.

[67] Abdelmoneim, H. M., "Dielectric and AC Conductivity of Potassium Perchlorate, $KClO_4$," *Acta Physica Polonica A.*, Vol. 117, No. 6, 2010.

[68] Chevrier, V. F., Hanley, J., and Altheide, T. S., "Stability of perchlorate hydrates and their liquid solutions at the Phoenix landing site, Mars," *Geophysical Research Letters*, Vol. 36, 2009.

[69] Nelson, S. O., Lindroth, D. P., and Blake, R. L., "Dielectric properties of selected minerals at 1 to 22 GHz," *Geophysics*, Vol. 54, No. 10, 1989, pp. 1344–1349.

[70] Fletcher, N., "The Surface of Ice," *Physics and Chemistry of Ice*, Royal Society of Canada Ottawa, Aug. 1973, pp. 132–136.

[71] Hobbs, P. V., *Ice Physics*, Glasgow: Oxford University Press, 1974.

[72] Hoekstra, P. and Doyle, W. T., "Dielectric Relaxation of Surface Adsorbed Water," *Journal of Colloid and Interface Science*, Vol. 36, No. 4, 1971, pp. 513–521.

[73] Slater, B. and Michaelides, A., "Surface premelting of water ice," *Nature Reviews Chemistry*, Vol. 3, No. 3, 2019, pp. 172–188.

[74] Yeşilbaş, M. and Boily, J.-F., "Particle Size Controls on Water Adsorption and Condensation Regimes at Mineral Surfaces," *Scientific Reports*, Vol. 6, 2016.

[75] Mironov, V. L., De Roo, R. D., and Savin, I. V., "Temperature-Dependable Microwave Dielectric Model for an Arctic Soil," *IEEE Transactions on Geoscience and Remote Sensing*, Vol. 48, No. 6, 2010, pp. 2544–2556.

[76] Peters, S. J. and Ewing, G. E., "Water on Salt: An Infrared Study of Adsorbed H_2O on NaCl(100) under Ambient Conditions," *Journal of Physical Chemistry B*, Vol. 101, No. 50, 1997, pp. 10880–10886.

[77] Van Vleck, J. H., "The Absorption of Microwaves by Oxygen," *Physical Review*, Vol. 71, No. 7, 1947, pp. 413–424.

[78] Asay, D. B. and Kim, S. H., "Evolution of the Adsorbed Water Layer Structure on Silicon Oxide at Room Temperature," *Journal of Physical Chemistry B*, Vol. 109, No. 35, 2005, pp. 16760–16763.

[79] Bhatt, B. I., *Design Data Book: Properties of Steam, Selected Refrigerants, n-Hexane and Brines*, New Delhi: CBS Publishers & Distributors, 2008.

[80] Hibbitts, C. A., Grieves, G. A., Poston, M. J., Dyar, M. D., Alexandrov, A. B., Johnson, M. A., and Orlando, T. M., "Thermal stability of water and hydroxyl on the surface of the Moon from temperature-programmed desorption measurements of lunar analog materials," *Icarus*, Vol. 213, No. 1, 2011, pp. 64–72.

[81] Mitchell, J. K. and Soga, K., *Fundamentals of Soil Behavior*, Vol. 3, Hoboken: John Wiley & Sons, Inc., 2005.

[82] Allen, C. C., Morris, R. V., Jager, K. M., Golden, D., Lindstrom, D. J., Lindstrom, M. M., and Lockwood, J. P., "JSC Mars-1: Martian Regolith Simulant," *Lunar and Planetary Science Conference*, Lunar and Planetary Institute, Houston, TX, 1997.

[83] Lasne, Y., Paillou, P., Freeman, A., Farr, T., McDonald, K. C., Ruffie, G., Maleziéux, J.-M., Chapman, B., and Demontoux, F., "Effect of Salinity on the Dielectric Properties of Geological Materials: Implication for Soil Moisture Detection by Means of Radar Remote Sensing," *IEEE Transactions on Geoscience and Remote Sensing*, Vol. 46, No. 6, 2008, pp. 1674–1688.

[84] Farouki, O. T., "Thermal properties of soils," Cold Regions Research and Engineering Lab, Monograph 81-1, Hanover, NH, December 1981.

[85] Fölsch, S., Stock, A., and Henzler, M., "Two-dimensional water condensation on the NaCl(100) surface," *Surface Science*, Vol. 264, 1992, pp. 65–72.

[86] Ulaby, F. T., Moore, R. K., and Fung, A. K., *Microwave Remote Sensing: Active and Passive. Volume II-Radar Remote Sensing and Surface Scattering and Emission Theory*, Reading: Addison-Wesley, Inc., 1982.

[87] Siegler, M., Aharonson, O., Carey, E., Choukroun, M., Hudson, T., Schorghofer, N., and Xu, S., "Measurements of thermal properties of icy Mars regolith analogs," *Journal of Geophysical Research: Planets*, Vol. 117, 2012.

[88] Allan, S., Braunstein, J., Baranova, I., Vandervoort, N., Fall, M., and Shulman, H., "Computational modeling and experimental microwave processing of JSC-1A lunar simulant," *Journal of Aerospace Engineering*, Vol. 26, No. 1, 2013, pp. 143–151.

[89] Lewis, J. S., Matthews, M. S., and Guerrieri, M. L., *Resources of Near-Earth Space*, Tucson: University of Arizona Press, 1993.

[90] Howe, A. S. and Sherwood, B., *Out of This World: The New Field of Space Architecture*, Reston: American Institute of Aeronautics and Astronautics, Inc., 2009.

[91] Nunes, I., Jurburg, S., Jacquiod, S., Brejnrod, A., Salles, J. F., Priemé, A., and Sørensen, S. J., "Soil bacteria show different tolerance ranges to an unprecedented disturbance," *Biology and Fertility of Soils*, Vol. 54, No. 2, 2018, pp. 189–202.

[92] Ferriss, R. S., "Effects of Microwave Oven Treatment on Microorganisms in Soil." *Phytopathology*, Vol. 74, No. 1, 1984, pp. 121–126.

[93] Wainwright, M., Killham, K., and Diprose, M. F., "Effects of 2450 MHz Microwave Radiation on Nitrification, Respiration and S-oxidation in Soil," *Soil Biology and Biochemistry*, Vol. 12, No. 5, 1980, pp. 489–493.

[94] Speir, T. W., Cowling, J. C., Sparling, G. P., West, A. W., and Corderoy, D. M., "Effects of Microwave Radiation on the Microbial Biomass, Phosphatase Activity and Levels of Extractable N and P in a Low Fertility Soil Under Pasture," *Soil Biology and Biochemistry*, Vol. 18, No. 4, 1986, pp. 377–382.

[95] Hallberg, K. B. and Lindström, E. B., "Characterization of *Thiobacillus caldus* sp. nov., a moderately thermophilic acidophile," *Microbiology*, Vol. 140, 1994, pp. 3451–3456.

[96] Vela, G. R. and Wu, J. F., "Mechanism of Lethal Action of 2,450-MHz Radiation on Microorganisms." *Applied and Environmental Microbiology*, Vol. 37, No. 3, 1979, pp. 550–553.

[97] Dunn, P. H., Barro, S. C., and Poth, M., "Soil Moisture Affects Survival of Microorganisms in Heated Chaparral Soil," *Soil Biology and Biochemistry*, Vol. 17, No. 2, 1985, pp. 143–148.

[98] Islam, K. R. and Weil, R. R., "Microwave irradiation of soil for routine measurement of microbial biomass carbon," *Biology and Fertility of Soils*, Vol. 27, No. 4, 1998, pp. 408–416.

[99] de Araujo, A. S. F., "Is the microwave irradiation a suitable method for measuring soil microbial biomass?" *Reviews in Environmental Science and Bio-Technology*, Vol. 9, No. 4, 2010, pp. 317–321.

[100] ASTM, "Standard Test Methods for Complex Permittivity (Dielctric Constant) of Solid Electrical Insulting Materials at Microwave Frequencies and Temperatures to 1650°C," American Society for Testing and Materials, Document D2520-13, West Conshohocken, PA, August 2013.

[101] Hewlett-Packard, "Measuring Dielectric Constant with the HP 8510 Network Analyzer," Hewlett-Packard, Product Note No. 8510-3.

APPENDIX

Sample cells used for dielectric loss measurements are described in Section 3.3.2. The cross-sectional dimensions of the sample cell aperture were determined by the frequency range (Table 2.2). However, the thickness of the sample cell is determined by λ_g (i.e., the wavelength in the sample material) which is a function of the relative permittivity, ε_r, relative permeability, μ_r, cutoff wavelength, λ_c, and free space wavelength, λ_0 (Eq. A.1). The optimum thickness is equivalent to $\frac{\lambda_g}{4}$ (where λ_g decreases with increasing ε_r) and ensures that uncertainties in ε_r and μ_r are minimized [101].

$$\lambda_g = Re\left(\frac{1}{\sqrt{\frac{\varepsilon_r \mu_r}{\lambda_0^2} - \frac{1}{\lambda_c^2}}}\right) \tag{A.1}$$

During sample cell design, it was not expected that high ice content would contribute significantly to an increase in the dielectric constant at the frequency range analyzed in this dissertation (i.e., 2.6 – 18 GHz), therefore $\varepsilon_r = \varepsilon_{rmax} \approx 3$. It should be noted that the effect of high loss components on ε_r was unknown during sample cell construction. Additionally, the metallic content of soil simulants (primarily Fe_2O_3) is very low, thus samples were considered to be non-metallic ($\mu_r \approx 1$). These values were also used to calculate the maximum sample thickness, which is limited to $\frac{\lambda_g}{2}$ due to instabilities inherent to the iterative processing methods (Section 2.4). The value of λ_g decreases with increasing frequency; therefore, optimum and maximum sample cell thickness values for each microwave band were calculated at center-band frequencies (Table A.1). Sample cell thickness values in Table A.1 reflect the total thickness of the soil sample and foam windows (used for containment with dry soils). Thus, soil sample thickness deviated from optimum by up to 45 – 48 % (S and G-bands) and 5 – 15 % (C, H, X, and P-bands) at center-band frequencies. Although variations from optimum are higher for the lower frequency bands, the increase in uncertainty

Table A.1: Sample cell optimum thickness

	Thickness in mm			
EIA	$\frac{\lambda_g}{4}$	Sample cell thickness	Soil sample thickness	$\frac{\lambda_g}{2}$
S	14.2	10.94	7.36	28.39
G	9.52	7.3	5.14	19.04
C	6.59	8.0	6.20	13.17
H	5.45	7.59	4.59	10.9
X	4.52	5.72	3.85	9.04
P	3.05	4.77	3.27	6.11

is not significant. Large uncertainties arise when samples approach the $\frac{\lambda_g}{2}$ (i.e., maximum thickness) limit [Hewlett-Packard]. However, it is unclear how uncertainty is affected by small deviations from optimum.

A major conclusion of the research contained in this dissertation was the observation of enhanced dielectric losses in salty, icy soils. Higher loss soil samples had correspondingly higher dielectric constant (ε') values. Therefore, within X-band, values of ε' were higher than anticipated, ranging from 2 – 12; however, in ∼60% of samples measured, ε' only varied from 2 – 4. For high loss samples ($\varepsilon' \approx 12$), soil sample thickness deviated from optimum by over 50% at 10.3 GHz (center-band frequency of X-band) but remained below the maximum thickness limit. However, higher frequencies within X-band (11.4 GHz and above) approached and exceeded the maximum thickness limit (Fig. A.1). For future studies of soils with high loss components, consideration should be given to constructing thinner sample cells or using thicker containment windows.

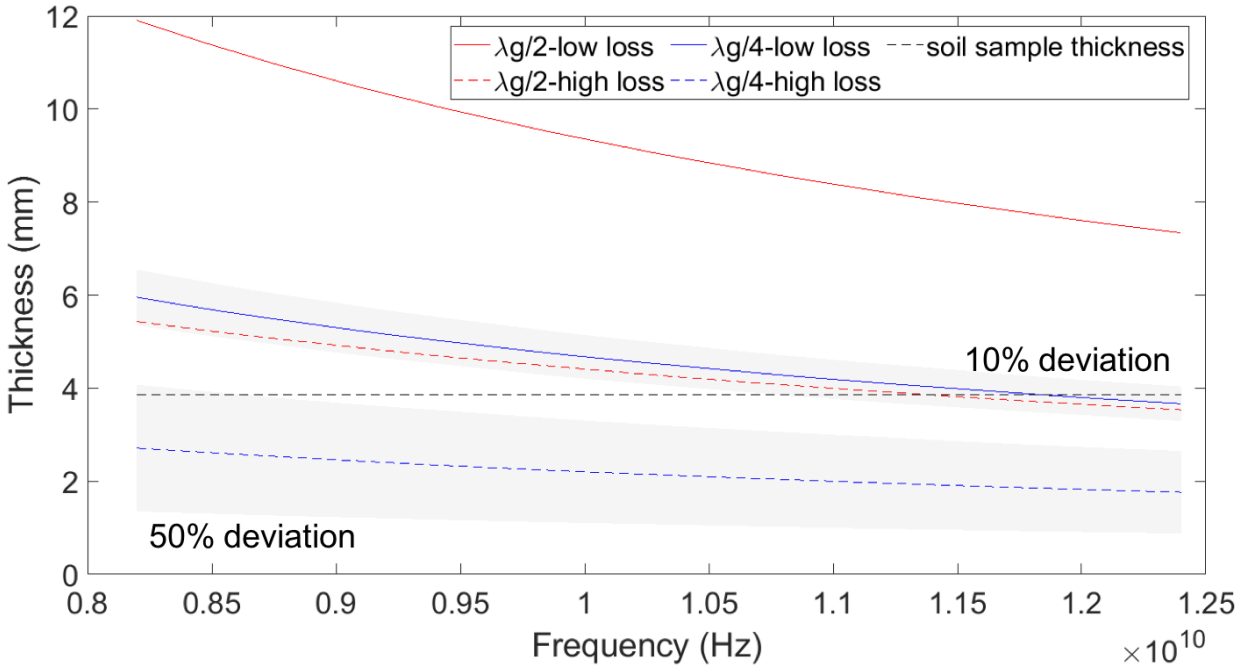

Figure A.1: Optimum thickness curves (blue) and maximum thickness curves (red) for low and high loss soil samples. Shaded regions indicate 10% and 50% deviation bands from optimum thickness at low and high loss, respectively.